PASSIVE FLOW CONTROL METHOD FOR MITIGATION OF UNSTEADY LOAD EXCURSIONS ON A WIND TURBINE BLADE

A Thesis

by

JAMIE MARIE WEBER

Submitted to the Office of Graduate Studies of
Texas A&M University
in partial fulfillment of the requirements for the degree of

MASTER OF SCIENCE

Approved by:

Chair of Committee,	Othon K. Rediniotis
Committee Members,	Edward B. White
	Mark T. Holtzapple
Head of Department,	Rodney Bowersox

December 2012

Major Subject: Aerospace Engineering

ABSTRACT

Stochastic flow conditions, such as large unsteady wind gusts and coherent structures in turbulent winds, cause detrimental blade loadings to horizontal axis wind turbines (HAWT). Such loadings lead to large blade root bending moments, increased blade fatigue damage, and inconsistent rotor torque and thrust. In the present work, robust, fast-response passive flow control (PFC) methods for mitigating adverse effects from unsteady aerodynamic loadings on a HAWT blade due were developed. The PFC methods examined were that of a leading-edge slot and a novel combination of two passive flow control devices, namely a leading-edge slot and a passively oscillating surface located at the slot exit (slot-flap). Wind tunnel tests were conducted at a Reynolds number of 0.3×10^6 and unsteady flow conditions were produced by an upstream disturbance generator. The disturbance generator utilized shed vortices from a rapidly deflecting upstream airfoil to simulate high-frequency, impulse-like load excursions on the main airfoil, representative of large wind gusts and coherent structures in turbulent winds.

Results from the test series demonstrated reduced maximum load excursions of 7 to 9% using the PFC methods as compared to clean airfoil tests. Effectiveness of the PFC methods decreased for loading with multiple vortex interactions. To further examine the influence of the slot-flap oscillations, two additional slot-flap configurations were examined: (1) increased rigidity and thickness and (2) reduced length. Both variations indicated a further reduction of transient load excursions from 8 to 12% as compared to a

clean airfoil. Coefficient of momentum (c_μ) was calculated for each slot-flap configuration, which was on the order of 1% and varied with angle of attack. The reduced excitation frequency (F^+) ranged from 0.96 to 1.23 based upon the slot-flap configuration. The three slot-flap variations showed comparable c_μ and F^+ average values and were within the uncertainty limits, indicating that the improved mitigation from the slot-flap variations is not attributed to c_μ and F^+ contributions. Based upon this study, the location and oscillation amplitude of the slot-flap configurations are significant parameters in the resulting mitigation effects.

DEDICATION

To my parents Susan and Paul Weber and my sister Jennifer

ACKNOWLEDGEMENTS

During my graduate studies I have had the opportunity to work and learn from several individuals. I wish to express my sincerest gratitude to my advisor Dr. Othon Rediniotis, who has provided continuous support and guidance throughout this project. I am greatly appreciative to have had the opportunity to contribute to this research. I would like to thank Dr. Ed White for providing valuable feedback and for being an additional source of experimental knowledge. I wish to also thank Dr. Mark Holtzapple for his time serving on my advisory committee. I will always be grateful to my undergraduate advisor Dr. Evan Lemley for his encouragement to pursue this path.

I would like to thank Vestas Technology R&D Americas, Inc. for providing financial support and an industry perspective to this project. Additionally, I wish to recognize Abigail Arrington of Vestas and her outreach and mentorship through Women of Wind Energy.

I am immensely appreciative and thankful of the assistance, friendship, and encouragement of my labmates and peers. Thank you to Shalom Johnson, Jason Schmucker, and Yogesh Babbar for their experimental expertise and insight. Thanks also are extended to Ben Recla and Luke Richards for helping construct many elements of my experimental setup. Special thanks are given to Robert Ehrmann who has provided equal parts knowledge and friendship.

Thank you to my friends Matt, Herlinda, and Brian for your continual optimism and encouragement. Additionally, I am greatly thankful for the love and support of my

family, who taught me from a very young age that anything is obtainable with hard work, dedication, and perseverance. Finally, much gratitude is expressed to the Department of Aerospace Engineering for providing me the opportunity to extend my education.

NOMENCLATURE

a	Speed of sound	[m/s]
A	Pitch rate of upstream disturbance	[–]
AFC	Active Flow Control	
ATEG	Adaptive Trailing Edge Geometry	
α	Angle of attack	[degrees]
α_D	Rate of change of angle of attack of the deployment	[rad]
α_D	Maximum deflection angle of upstream disturbance	[degrees]
c	Chord length	[m]
CCW	Circulation Controlled Wing	
C_L	Coefficient of Lift	[–]
$C_{L,max}$	Maximum static C_L	[–]
C_M	Moment Coefficient	[–]
C_μ	Coefficient of Momentum	[–]
c_μ	Periodic excitation Coefficient of Momentum	[–]
C_p	Coefficient of Pressure	[–]
CTKE	Coherent Turbulent Kinetic Energy	
ΔC_L	Change in C_L from load the excursion	[–]
DSV	Dynamic Stall Vortex	
f	Flow frequency	[Hz]
F^+	Reduced excitation frequency	[–]

FFT	Fast Fourier Transform	
γ	Ratio of specific heat	[–]
Γ	Propagation constant	[m^{-1}]
h	Slot width	[m]
HAWT	Horizontal Axis Wind Turbines	
ID	Tubing inner diameter	[m]
J_n	Bessel function of the first kind of order n	[–]
K	Polytrophic factor	[–]
k	Reduced frequency $\omega/2U_{ref}$	[–]
L	Tubing length	[m]
λ	$128\mu LV / (\pi \, ID^4 P_{atm})$	[s]
ω	Oscillation frequency $2\pi f$	[Hz]
μ	Dynamic viscosity	[Pa·s]
pc	Volume polytrophic constant	[–]
PFC	Passive Flow Control	
φ	Phase angle	[rad]
PIV	Particle Image Velocimetry	
Pr	Prandlt number	[–]
P_s	Surface static pressure	[Pa]
P_t	Transducer pressure	[Pa]
r	Amplitude ratio (gain)	[–]
Re	Reynolds number	[–]

RP	Rapid Prototyping	
ρ	Density	[kg/m^3]
σ	Transducer diaphragm deflection	[–]
s	Shear wave number	[–]
SJA	Synthetic Jet Actuator	
TF	Transfer Function	
U_{jet}	Slot/Jet velocity	[m/s]
U_{ref}	Reference velocity	[m/s]
VG	Vortex Generator	
V_v	Internal transducer volume	[mL]
V_T	Tubing internal volume	[mm^3]
x_{te}	Distance from trailing edge to actuation point	[m]
ZNMF	Zero Net-Mass Flux	

TABLE OF CONTENTS

LIST OF FIGURES

LIST OF TABLES

CHAPTER I

INTRODUCTION

The Importance of Aerodynamic Wind Energy Research

As indicated in the 2007 Department of Energy (DOE) *20% Wind Energy by 2030* report [1], wind energy research is required to create a highly efficient and reliable energy system capable of meeting the nation's growing energy demands. Furthermore the U.S. Energy Information Administration (EIA) stated in its 2011 Annual Energy Outlook [2] that American energy consumption is projected to increase 0.7% per year from 2009 to 2035, totaling approximately 114.2 quadrillion Btu in 2035. The significant growth in energy consumption requires an increase in US energy production from all energy sectors. With respect to wind energy, this requires advancements in the areas of transmission, economics, and manufacturing, specifically in the area of enhanced fluid-blade aerodynamics.

Power produced by horizontal axis wind turbines (HAWT) is a function of wind velocity and rotor size. To increase the electrical energy generated, current trends in manufacturing involve developing longer blades to increase rotor capture area and constructing taller structures to access the greater wind velocities seen at higher altitudes. Furthermore, manufacturing costs scale with the total weight, so that lighter blade structures are favored; however, this is not a linear design problem. As turbine structures grow larger and lighter, fatigue damage and tip deflection become critical matters. Innovative control technologies are necessary for these large aerodynamic

structures to withstand the fatigue loading cycles and tip deflections that occur during extreme atmospheric inflow conditions.

In open air fields, wind turbines are under the influence of an unsteady flow environment during the majority of operational time [3–5]. Stochastic flow conditions, such as large unsteady wind gusts and large coherent structures in turbulent winds, cause detrimental blade loadings [6–8]. These undesirable loads lead to structural fatigue as well as potentially causing mechanical damage of the rotor, which may significantly affect operation and mechanical life of the system elements. In addition, time-varying forces contribute to power fluctuations, which adversely impact the overall power quality and limit performance [9, 10]. The reduction of undesirable loading caused by unsteady aerodynamics will reduce power fluctuations as well as reducing structural fatigue of the rotor.

Wind Turbine Unsteady Aerodynamics Literature Review

Wind turbine blades are designed with a life expectancy of 20 years [1]. In parallel to this, the influence of inflow turbulence on the structural response of a wind turbine blade is an area of high interest in the wind energy industry, because unsteady aerodynamic loadings may precipitate premature fatigue and structural damage. The brief literature review that follows examines the relationship between inflow conditions and fatigue damage. Mouzakis, Moradakis, and Dellaportas [11] performed an analytic study using multivariable regression to identify independent parameters that describe deterministic and stochastic properties of the incoming flow. The study results indicated that inflow

turbulence is a main contributor to fatigue in all wind turbine components. Fragoulis [12] identified similar observations from a study relating to the effects of complex terrain on turbulence, and concluded that increased turbulence propagates increased fatigue. Conversely, Nelson, Manuel, Sutherland, and Veers [13] reported mixed results relating primary and secondary inflow parameters (such as mean wind speed and wind shear, respectively) to fatigue and extreme loads. However, utilizing a reduced dataset that included only 10-minute periods with a mean wind speed above the rated wind speed (13 m/s), results showed an improved correlation of the primary inflow parameters to fatigue damage.

To examine fatigue damage propagated by short-lived, high-frequency inflow loadings, Kelley, Osgood, Bialasiewicz, and Jakubowski [14] performed wavelet analyses on transient HAWT blade load excursions. By studying field test data of an upwind, three-bladed Micon 65/13 turbine, their studies showed that the presence of coherent turbulent structures significantly contributed to large load excursions, resulting in fatigue damage. Additionally, the wavelet analysis validated that wind gusts may contain complex turbulence structures, which subsequently provide a broad range of frequency excitation to the turbine rotor as the air passes through it.

In a supplemental paper, Kelley, Jonkman, Scott, Bialasiewicz, and Redmond [6] further illustrate the potential detrimental effects of coherent turbulence on energy production. Based upon their spectral analysis of coherent turbulent kinetic energy (CTKE), the authors state that it is unlikely for the entirety of the CTKE that interacts with the rotor blades to be converted into electrical power. This was particularly noted

for higher frequencies of the spectrum (0.1 – 10 Hz) of parasitic energy, which does not contribute to energy production and must be dissipated by the structure and components. The authors' further state that for the greater operational time spent in the parasitic region there is a greater need to incorporate and account for high frequency coherent turbulence and corresponding loadings in the turbine design.

Numerical studies that describe the aeroelastic response propagated by inflow conditions have also been conducted. Wind shear and turbulence effects were examined by Eggers, Digumarthi, and Chaney [15] using a von Karman spectrum, which is common in stochastic wind simulations. In these studies, wind shear was shown to substantially increase blade spanwise fatigue damage and identified turbulence as a significant contributor of inconsistent rotor torque and thrust. Assuming the presence of vortices under certain atmospheric conditions and modeling these coherent structures using an idealized Rankine vortex, Hand, Robinson, and Balas [16] studied and identified the vortex characteristics that contribute to high-amplitude cyclic blade loads. Their results showed that such vortex interactions lead to large blade root bending moment amplitudes that contributed to high damage rates.

Unsteady inflow conditions are exceptionally complicated because they are a product of periodic and aperiodic sources [3–5]. Periodic flow conditions are induced by blade rotational effects, including such environmental contributors such as tower shadow, yaw misalignment, atmospheric boundary layers, and various other inflow conditions relating to rotational effects. The periodic contributors are directly related to the rotational frequency of a wind turbine blade. The frequencies of these effects are on the order of

1–*P* to *n*–*P* where *P* is the rotational frequency of a single blade rotation and *n* is the number of blades. Conversely, aperiodic unsteady flow is of a smaller time scale and is a product of atmospheric turbulence, blade wake interactions, and wake conditions. Wavelet analysis indicates that the resulting loads of this high frequency unsteadiness are applied more as an impulse than cyclic load variations, which occur over one blade revolution (1–*P*) [14]. The aperiodic flow conditions significantly contribute to stochastic blade loadings; however they are hard to predict, making it difficult to model and design for appropriately [3, 4, 14].

Research Objectives and Approach

The primary objective for this research was to develop a robust, fast-response flow control method for mitigating of adverse effects of unsteady aerodynamic loadings on a HAWT blade resulting from aperiodic inflow conditions. To meet this objective, unsteady flow conditions were created which allowed for accurate modeling and experimental testing. Static tests with attempts to correct for unsteady conditions under-predict blade loadings and do not correctly describe the complex nature of unsteady flow [3, 17]. For a representative modeling technique, repeatable, unsteady conditions must be incorporated in wind tunnel tests. For this research, the unsteady flow condition was produced by an upstream disturbance generator, which utilized vortices shed from a rapidly deflecting upstream airfoil to represent high-frequency, impulse-like load excursions on the main airfoil. After establishing that the unsteady flow field is representative of HAWT inflow conditions, the research focused on mitigating the

adverse aerodynamic effects. The mitigation approach involved a passive flow control design that utilized periodic excitation to reduce unsteady loading. Fundamental elements of this flow control design are described in detail in the following chapter.

CHAPTER II

INTRODUCTION TO FLOW CONTROL

Flow Control Overview

Historically, flow control techniques have been incorporated into a variety of airfoil structures to enhance aerodynamic performance. The implementation of flow control methods has allowed for a variety of aerodynamic improvements based upon the following optimization objectives: (1) transition, separation and circulation control, (2) drag and noise reduction, and (3) mixing enhancement. One such method is active flow control (AFC), which is defined as mechanisms that actively control local air surrounding a surface. The principle of AFC is highly investigated for aerospace applications, because many experimental applications have been shown to produce favorable results for a large spectrum of flow conditions. AFC is often implemented to improve or manipulate aerodynamic properties of a lifting surface by utilizing either the addition of stored high-momentum air, the removal of low-momentum fluid, or by other actuated geometric modifications. AFC devices may be further classified by predetermined or interactive methods. Predetermined AFC mechanisms may be steady or unsteady flow manipulations, but the control is open-loop so that the amount of energy input does not change based upon the flow conditions. Conversely, interactive methods include sensing units to allow for the augmentation of the amount of flow control based on incoming flow conditions. Interactive methods may be closed- or open-loop depending if the mechanism includes an output monitoring method, which

establishes if the desired response was achieved. Finally, typical AFC devices include a gamut of mechanisms, ranging from the fairly simple, reduced designs, such as blowing [18], steady suction [19], trailing-edge flaps or ailerons [20], to more complicated structural and fluidic actuation, including zero-mass flux blowing [21, 22], oscillatory blowing [23], piezoelectric actuators [24], synthetic jet actuators [25–28], Gurney flaps [29] and many more.

Previous research at Texas A&M University has shown that active control methods, specifically implementing leading-edge synthetic jet actuators (SJA), significantly impact stall effects and aerodynamic loadings [25–27]. Because of the noteworthy influence on flow manipulation, this thesis research initially considered active flow control as an optional method to reduce the effects of adverse, unsteady aerodynamic loads; however, there is a tradeoff in the application of AFC. Typical active flow control mechanisms require an external or auxiliary power supply, so the corresponding increase in performance requires an increase in the complexity of the fluidic actuation design. Simple, robust, light-weight blade structures are favored in wind industry. Considering this and the nature of application, the following research chose to focus on passive flow control (PFC) methods as a mitigation technique. Unlike AFC, passive methods do not require an auxiliary energy supply to enhance aerodynamic properties. This approach comparatively limits manufacturing cost and reduces overall lifetime maintenance while eliminating extra weight caused by the addition of AFC actuation mechanisms [33]. As the predecessors of many active flow control devices, classic examples of passive flow control elements similarly include a spectrum of designs involving geometric or fluidic

manipulation, such as vortex generators [22]; trip-strips, surface roughness, or spoilers [31]; leading-edge slot or slats [32]; variable leading-edge geometries [33]; acoustic cavities [34], etc.

Flow control is a highly multivariable design problem, with dozens of papers published annually with respect to new applications and control methods. Although the following is not an exhaustive review on methods and applications of flow control, select literature is presented relating to the research presented in this thesis and provides a background for the current work. Before examining current implementations, a brief history of flow control is presented. A more detailed view of the historical development of flow control is delineated in Gal-de-Hak [35] and Wygnanski [36].

Select Flow Control Literature Review

The origins of the science of flow control are attributed to Prandlt [36] (1904) and his work with boundary layer theory and control. Using a cylinder in a free stream, Prandlt demonstrated increased lift by using suction to manipulate the boundary layer on one side. Suction was not readily implemented until the early 1940's, when many researchers began to demonstrate the use of suction for delaying transition and maintaining laminar flow, thus reducing the transition-associated drag penalty [35]. As trends in wing design began moving to thinner airfoil profiles, flow control methods moved away from suction techniques, which at the time required large internal ducting systems. Suction was then replaced by constant blowing systems which, unlike its predecessor, utilized smaller internal ducting and typically readily available compressed

air to delay flow separation. The coefficient of momentum C_μ, introduced by Ph. Poisson Quinton [36] became the widely accepted parameter describing the relative strength of blowing ($C_\mu > 0$) and suction ($C_\mu < 0$) and is defined as

$$C_\mu = \frac{m'_{jet} U_{jet}}{\frac{1}{2}\rho_{ref} {U_{ref}}^2 A_{ref}} \tag{2.1}$$

which uses incompressible, isentropic flow properties to relate slot momentum to free-stream momentum by means of the mass flow rate through the slot $m'_{jet} = \rho_{jet} U_{jet} A_{jet}$, the reference free stream velocity and density U_{ref} and ρ_{ref} and the planform area A_{ref}.

As technology advanced, ejectors and innovative jet devices allowed for the combination of suction and blowing and the development of pulsing streams of high momentum air, known as periodic excitation. As compared to constant blowing, periodic excitation reduced the necessary jet momentum by an order of magnitude to achieve the same performance objective [36, 39]. The improved aerodynamic response is believed to be the product of added vorticity generated by the periodicity of the injected momentum. The additional vorticity enhances mixing of the free-stream momentum into the boundary layer, resulting in less momentum required to attain the same enhancement [40]. The coefficient of momentum for periodic excitation, c_μ, is thus typically redefined as

$$c_\mu = \frac{h}{c} \frac{U_{Jmax}^2}{U_{ref}^2} \tag{2.2}$$

which relates the slot width h and maximum slot velocity U_{Jmax}, to the chord length c and reference velocity U_{ref}.

A second non-dimensional variable is used to describe the excitation frequency, known as the reduced excitation frequency F^+. This flow control parameter is optimum at an approximate value of unity [41, 42] and is the ratio of the pulsing frequency f and the distance from the slot to trailing edge x_{te} to the free stream velocity U_∞ defined as:

$$F^+ = \frac{f x_{te}}{U_\infty} \tag{2.3}$$

Seifert, Daraby, Nishri, and Wygnanski [38] illustrated the effectiveness of pulsed blowing by comparing the method to steady blowing flow control. Experiments were conducted at test Reynolds numbers between 0.15×10^6 and 0.75×10^6. The model used was a NACA 0015 airfoil, from which controlled air was directed through a leading edge slot. Pulsed blowing at a low momentum coefficient ($c_\mu = 0.008$) and at a reduced forcing frequency ($F^+ = 0.8$) showed 30% increase in the lift coefficient as compared to a clean airfoil. For the same momentum coefficient, steady blowing showed no change.

An example of load control using periodic excitation with active flow control was performed by Weaver, McAlister, and Tso [41], who examined the effects of pulsed and steady blowing to control dynamic stall. Dynamic stall is an unsteady, complex aerodynamic phenomenon that may result from unsteady inflow conditions and is common to many rotor applications [43]. It is attributed to the dynamic increase of the local angle of attack of an airfoil beyond static stall limitations, producing maximum values of lift, drag and moment coefficients exceeding that of static conditions [7, 14]. For their research, Weaver, et al. achieved dynamic stall effects by sinusoidally pitching a Boeing-Vertol VR-7 airfoil, a typical helicopter rotor profile. Tests involved flow visualization to determine aerodynamic forces and moments for tests conducted at a

Reynolds number of 0.1×10^6. Blowing was achieved utilizing a slot located along the upper surface of the model with a reduced frequency F^+ from 0 to 3 and the momentum coefficient, $C\mu$, from 0.03 to 0.66. Results showed that under certain conditions both blowing methods were able to maintain the dynamic stall separation bubble at the airfoil leading edge, thus considerably enhancing lift. It was demonstrated that pulsed blowing increased lift by 20% as compared to the reference clean airfoil, whereas under the same test conditions, steady blowing only increased lift by 12%. Additionally, the largest lift enhancement was observed for a reduced excitation frequency of $F^+ = 0.9$, corresponding to the principle that an approximate value of unity produces the most favorable aerodynamic response.

Similarly, Greenblatt [21] used experimental flow control methods to trap the dynamic stall separation bubble upstream using zero net-mass flux blowing (ZNMF), and thus delayed load excursion from dynamic vortex shedding. Two airfoils were studied: NACA 0012 and NACA 0015. Each airfoil was incorporated with a leading-edge jet, which controlled blowing along the upper surface; however, the locations and angles of the jets varied: the 0012 at 5% chord length at an angle of 45º, and the 0015 at approximately the tip of the leading edge with a 90º angle. Their results indicated that relatively low reduced excitation frequencies ($F^+ < 1$) and moderate momentum coefficients ($0.1\% \leq c_\mu \leq 0.5\%$) were effective of imposing control on the 0015. For the 0012 airfoil at the same forcing frequency, significantly larger momentum coefficients were required and moment stall was not completely eliminated. Because the jet angle and location varied with respect to airfoil geometry, it is difficult to make

strong correlations between geometry effects, such as leading edge curvature and percent thickness to AFC parameters. However, this provides an example of the multivariable nature of flow control.

Many researchers have attempted to incorporate flow control methods in wind turbine blade designs to reduce loadings that lead to fatigue damage. The use of trailing-edge microtabs and microflaps has been examined by van Dam et al. [29, 44, 45] and have been shown to reduce the lift excursions and therefore transient loads on the blade relating to fatigue. Extensive research has been performed by Risoe National Laboratory on Adaptive Trailing Edge Geometry (ATEG) by Anderson et al. [46], Bak et al. [47], and Fuglsang et al. [48, 49]. Typical ATEG utilizes trailing-edge flap geometries that have no visible joints or hinges, but is actuated by piezoelectric actuators, which allows for rapid and independent deflection along the span of the blade. Lewis, Potts, and Arain [50] used leading-edge active stall strips to manipulate stalling characteristics on a wind turbine airfoil.

One augmentation to classic blowing and suction control examined for potential wind turbine applications is the development of the circulation control wing (CCW). Using trailing edge, high-momentum jets directed tangentially over a rounded trailing edge airfoil, circulation controlled wings increase the lift on an airfoil by increasing circulation. This design utilizes the Coanda effect to delay boundary layer separation and manipulate the location of the trailing-edge stagnation point. Tongchitpakdee, Benjanirat, and Sankar [51] studied this design with respect to wind turbine applications. Computational studies were performed using a NREL Phase VI rotor with a S809 airfoil

at wind speeds of 7 and 15 m/s and jet momentum coefficients ranging from 0 to 0.10. For the lower speed of 7 m/s, results showed attached jet flow along the curved trailing edge as well as shifted stagnation points, indicating improved suction and corresponding lift. However at 15 m/s, a typical rated wind speed of a 2-MW HAWT, the flow separates at a location forward of the trailing-edge jet. Liu [52] expanded on the CCW design by adding a leading edge jet to account for these separation effects. His results from a computational study demonstrated the combination was highly effective because the leading edge blowing prevented separation and achieved lift at high angles of attack while the trailing-edge blowing allowed for an overall increase in lift.

An analysis by Stalnov, Kribus, and Seirfet [22] studied AFC using zero net-mass flux (ZNMF) piezofluidic actuators applied to a wind turbine airfoil. The premise of their research involved demonstrating that ZNMF actuation performed better than the commonly applied vortex generators. Stalnov et al. concluded that for the target Reynolds number for which the vortex generators were designed ($Re = 0.6\times10^6$), the VGs had the design advantage over the two methods. However, at higher Reynolds numbers, the VGs were not effective on the flow (because of separation) or produced additional drag penalty. Additionally, at lower Reynolds numbers ($Re = 0.3\times10^6$) the zero-mass flux actuators proved superior, nearly doubling the lift increment of that produced by the VGs. This observation is highly applicable to wind turbines, which encompass a range of airflow velocities and rotor speeds. The results indicate that a variable flow control system is needed for a robust system that can manage unsteady conditions at start-up velocities as well as nominal operation speeds.

Maldonad, Boucher, Ostman, and Amitay [53] investigated active vibration control using piezoelectric synthetic jet actuators for wind turbine blade applications. Experimental wind tunnel tests were conducted at Reynolds numbers between 7.1×10^4 and 2.38×10^5, and flow and vibrational effects were quantified using Particle Image Velocimetry (PIV) and surface mounted strain gages. The synthetic jets were located along just past quarter chord ($0.318c$) of a S809 airfoil for which the momentum coefficient for the SJAs ranged from 0.00134 to 0.00597. Results showed a reduction of vibration by a factor of ~6.5 when the synthetic jets were activated in the outboard region of the blade.

While each method examined exhibited a potential advancement in HAWT blade technology, comparisons between the various approaches are difficult to conclude as each flow control method is at a different level of research and development and seek to optimize different areas. Currently, the main issue relating to implementing flow control technology in wind turbine structures is the lack of field test data on large-scale wind turbines. However, at this time full-scaled field tests are many years away and more exploratory research is required [40].

Passive Flow Control Approach

Considering the nature of the specific application, a novel passive flow control apparatus was proposed and developed. The flow control mechanism presented combines of two passive flow control devices, namely a leading-edge slot and a

passively oscillating surface located at the slot exit (Figures 2.1 and 2.2). A description of the mechanics of this design follows:

1. Air is ingested at the leading-edge stagnation point.
2. Air is driven through the internal path by a naturally occurring pressure gradient based on the pressure differential from the airfoil pressure and suction sides.
3. The air is accelerated, acting as a jet, and is tangentially blown along the upper surface.
4. An oscillating surface is added at the slot exit. The oscillation of the surface is the result of resonance as the surface interacts with the jet. It is designed to oscillate at the optimum flow frequency by structural bending as well as "opening" and "closing" at the slot exit.
5. The oscillations enhance fluidic mixing of high-momentum flow which, prevents separation.

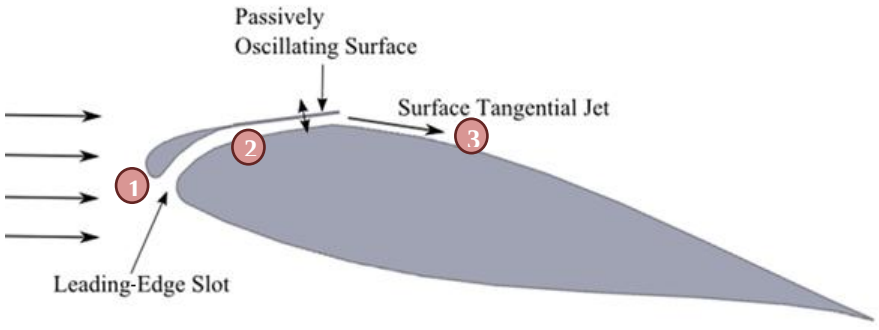

Figure 2.1 Diagram of passive flow control elements of a leading-edge slot and an oscillating slot-flap

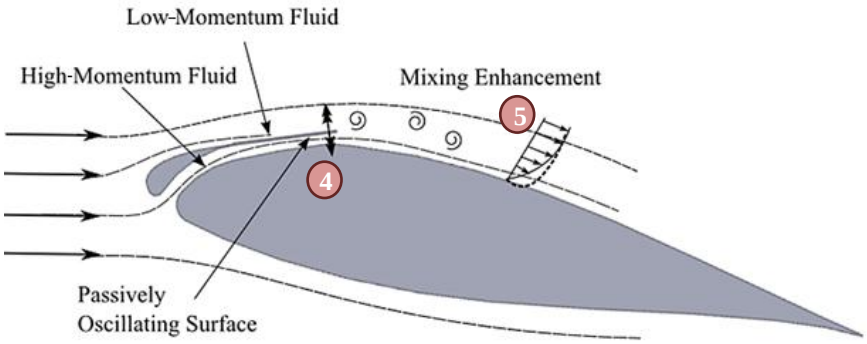

Figure 2.2 Illustration of fluidic mixing from passive flow control elements of a leading-edge slot and an oscillating slot-flap

As shown with active flow control methods, oscillating jet motion allows for delay of separation by introducing unsteady flow conditions, which enhance mixing of high- and low-momentum flows. Shear layers parallel to the airfoil surface are generally responsive to disturbances. When the oscillating jet motion is optimized and a characteristic frequency is obtained, the fluid shear layers begin to resonate, causing the formation of coherent structures in the form of discrete vortices. The vortices convect downstream, mixing and adding energy to the boundary layer.

The proposed passive flow control method maintains this oscillatory nature by adding an oscillating structure mounted at the slot exit. The oscillating structure is cantilevered at the leading edge corner of the slot and is designed so that the differences in pressure produce resonance flapping in the first bending mode of the structure. For low angles of attack, the composite structure is in the "closed" position. The structure produces minimal fluctuation disturbances in this position and reduces the coefficient of

momentum, which in turn reduces the mass flux produced by the slot. When the airfoil is at high angles of incidence, the composite structure is in the "open" position. In this position, the slot produces higher momentum and mass flux while the cantilevered structure oscillates at higher structural bending modes through resonance.

Two parameters are used to optimize the design: (1) the coefficient of momentum (c_μ) which is related to the jet generated by the leading edge slot, and (2) the reduced excitation frequency (F^+) which is related to the oscillating surface. Although this design is primarily governed by two fundamental flow control parameters, it quickly becomes a large, multivariable problem when considering the number of design combinations possible. For example, the addition of an oscillating structure not only requires quantifying the frequency of the oscillations, but also the effects of physical and geometrical properties such as location, length, oscillation amplitude, and material strength must be considered.

CHAPTER III

WIND TUNNEL MODEL

Airfoil Characteristics

A NACA 63_3-418 airfoil was selected as the test model for the current research. This is a common, non-proprietary airfoil used for wind turbine blade testing, which represents an airfoil geometry similar to an outbound turbine blade profile. The airfoil has a large percent thickness and camber and is used in wind turbine application because of its 'gentle stall' characteristics at high angles of attack. The test model has a 9-inch (23-cm) chord and an 18-inch (46-cm) span, and spanned the width of the tunnel. The airfoil (Figures 3.1 through 3.3) was designed in SolidWorks based upon contour coordinates provided by University of Illinois at Urbana-Champaign (UIUC) Applied Aerodynamics airfoil database [54]. The entire model (main airfoil and leading-edge slot) was manufactured in four pieces via rapid prototyping and sealed together with an epoxy-resin based adhesive. The airfoil was internally supported by two steel rectangular beams at 0.22*c* and 0.44*c* for the full span length.

Pressure taps of Tygon tubing with an inner diameter of 0.034 ±0.004 inch (0.86 ± 0.10 mm) were embedded in the airfoil, flush to the surface. The pressure taps were horizontally staggered along the span of the blade to prevent interference of surface-boundary layer fluid interactions. The airfoil contained 31 taps with greater distribution density and smaller spacing intervals near the leading edge, as is standard practice, with 22 on the suction surface and 9 on the pressure surface. The exact locations of the

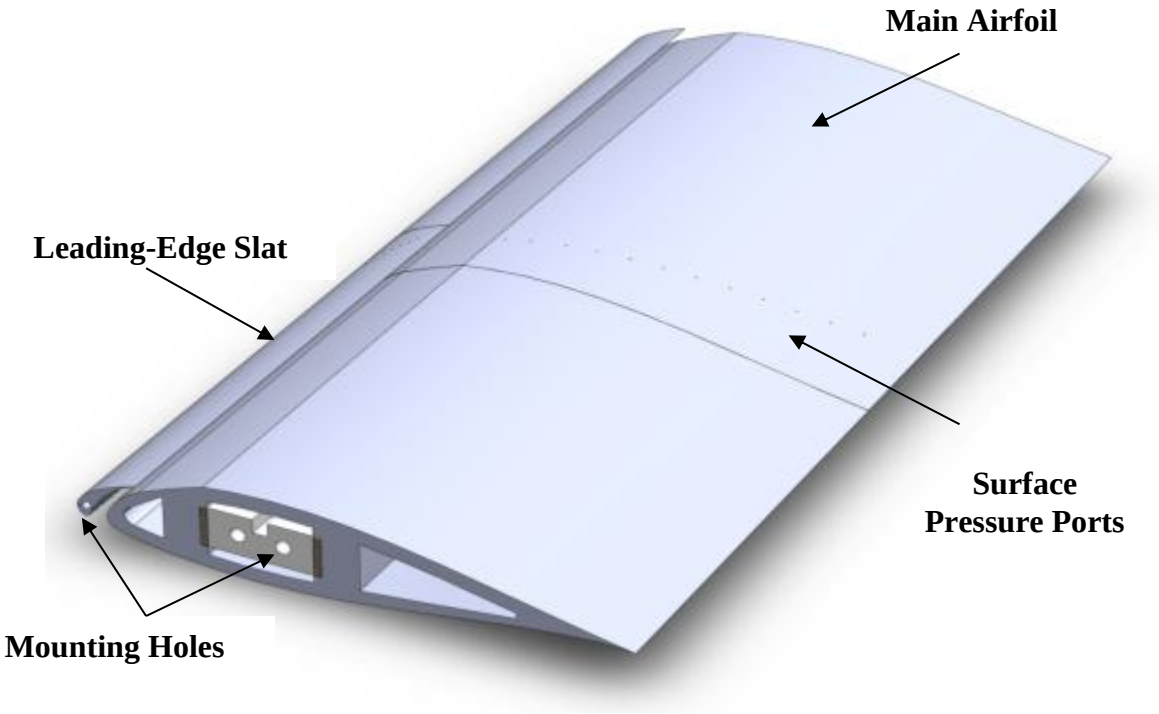

Figure 3.1. SolidWorks model of RP main airfoil and leading-edge slat

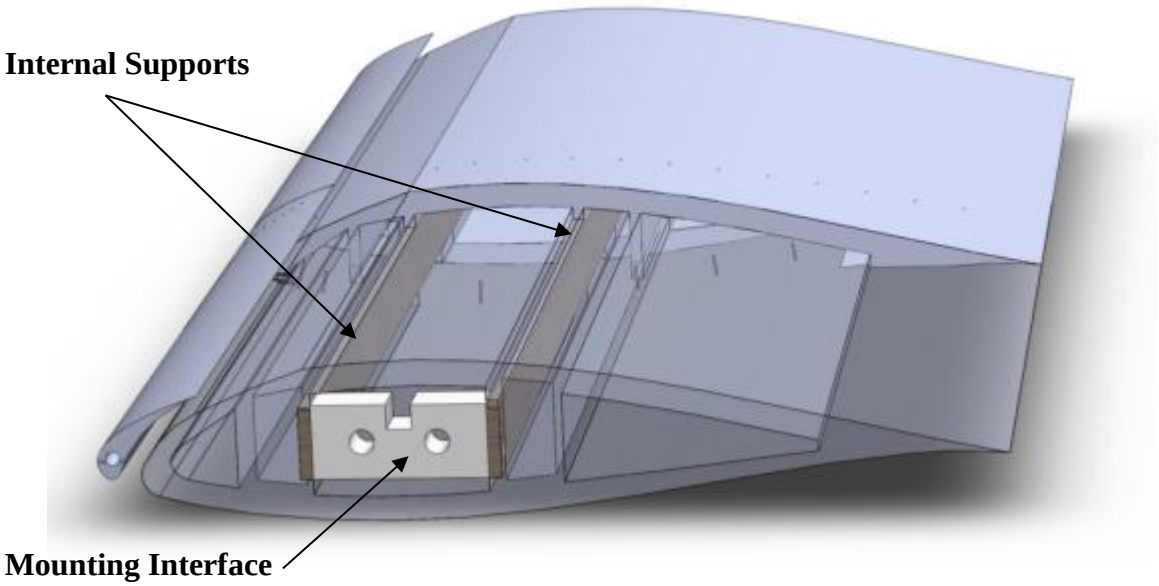

Figure 3.2. SolidWorks model showing the internal structure of the airfoil

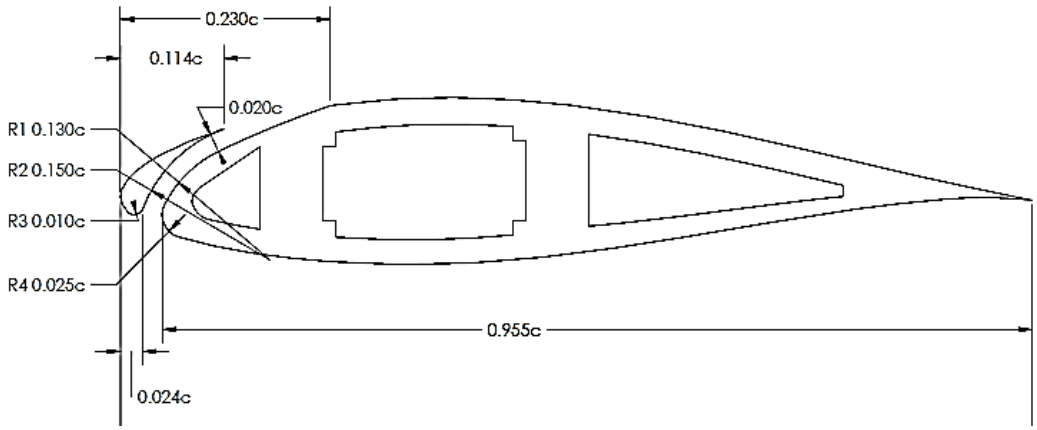

Figure 3.3. SolidWorks dimensional specifications of the slot location, width, and curvature

Table 3.1. Chord-wise pressure port locations

Upper Surface

Port	1	2	3	4	5	6	7	8	9	10	11	12	13	14	15	16
x/c	0	0.005	0.01	0.02	0.03	0.04	0.05	0.06	0.07	0.08	0.23	0.25	0.3	0.36	0.48	0.54
y/c	0.013	0.018	0.025	0.035	0.041	0.049	0.052	0.057	0.062	0.065	0.104	0.104	0.109	0.111	0.104	0.096

Upper Surface							Lower Surface								
Port	17	18	19	20	21	22	Port	23	24	25	26	27	28	29	30	31
x/c	0.6	0.66	0.72	0.78	0.84	0.86	*x/c*	0.8	0.7	0.6	0.5	0.4	0.3	0.2	0.07	0.005
y/c	0.087	0.075	0.061	0.048	0.034	0.030	*y/c*	-0.011	-0.026	-0.043	-0.057	-0.067	-0.069	-0.064	-0.042	-0.001

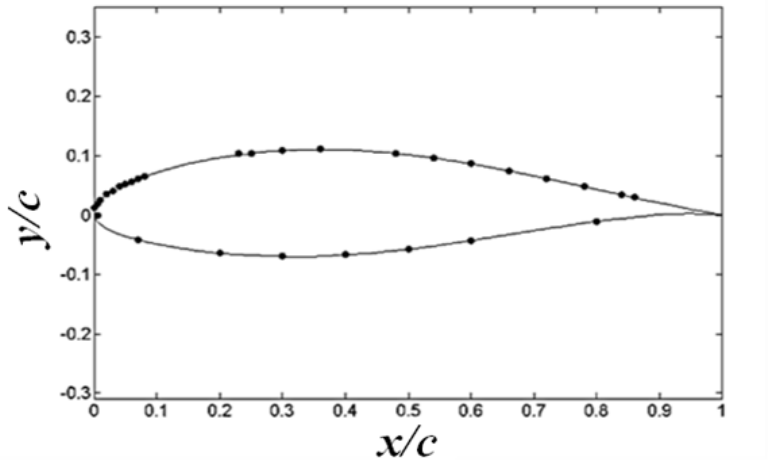

Figure 3.4. Chord-wise pressure port locations

pressure taps are shown in Figure 3.4. Tygon tubing of length 18.00 ± 0.06 inches (45.7 ± 0.2 cm) and an inner diameter of 0.034 ± 0.004 inch (0.86 ± 0.10 mm) connected the pressure ports to externally mounted ±25-mbar differential pressure sensors manufactured by Honeywell. Instantaneous pressure measurements were acquired and recorded at each port at a sampling rate of 1 kHz. Employing trapezoidal discrete integration of the coefficient of pressures as measured by the surface ports, instantaneous aerodynamic forces and moments were calculated.

The airfoil spanned the test section width and was mounted directly to the wall of the test section. This setup is favored because it eliminates three-dimensional tip leakage effects. The model was fixed in the test section by bolting the airfoil mounting end pieces to 10-inch Plexiglas circular cutouts from the test section walls. Pressure from external clamps secured the cutouts in place, allowing for easy change in angle of attack while preventing test section leakage. The pitch angle of the model was set by rotating the endplates for a range of angle of attack from –9˚ to 24˚.

During the airfoil manufacturing process, a small linear indention was incorporated to the airfoil profile, indicating the chord line. From this reference line, the zero angle of attack was determined by aligning the chord line with the floor of the test section. Additionally, the airfoil angle of attack was measured using a digital inclinometer along the chord reference line. The digital inclinometer had a precision of 0.1˚ and was externally mounted on the test section. Finally, the angle of incidence was verified by validating the zero lift angle of attack from the coefficient of lift curve for static conditions of a clean airfoil.

Passive Flow Control Design

This research involved studying the unsteady aerodynamic effects of two passive flow control design: (1) a leading-edge slot and (2) a novel arrangement of passive flow control elements involving a leading-edge slot and an oscillating structure (slot-flap) located at the airfoil upper surface at the slot exit. The leading edge slot used in both passive flow control designs was designed with the following specifications. The width of the leading-edge slot is 2% of the main airfoil chord length (0.02*c*) whereas the leading-edge slat chord length was 11.5% (0.115*c*). The slat was fabricated using rapid prototyping (RP) material and internally reinforced with a steel, cylindrical all-thread rod of 0.125-inch (3.2-mm) diameter. The internal rod was used to position and mount the leading-edge slat to the test section, and was fixed in place by externally bolting the rod to the circular cutouts.

The slot properties were selected so that the ingestion location on the pressure side of the airfoil was near the leading-edge stagnation point for high angles of attack (greater than 12˚). The curvature of the slot was designed to have a radius 1.5% of the chord length. The internal curvature and slot exit along the upper surface were manufactured so that the jet produced by the slot was tangentially blown along the upper surface, but after the pressure suction peak. Figure 3.3 is the SolidWorks drawing of the leading-edge slot and corresponding slat dimensions and Figure 3.5 shows the complete RP model and slot configuration.

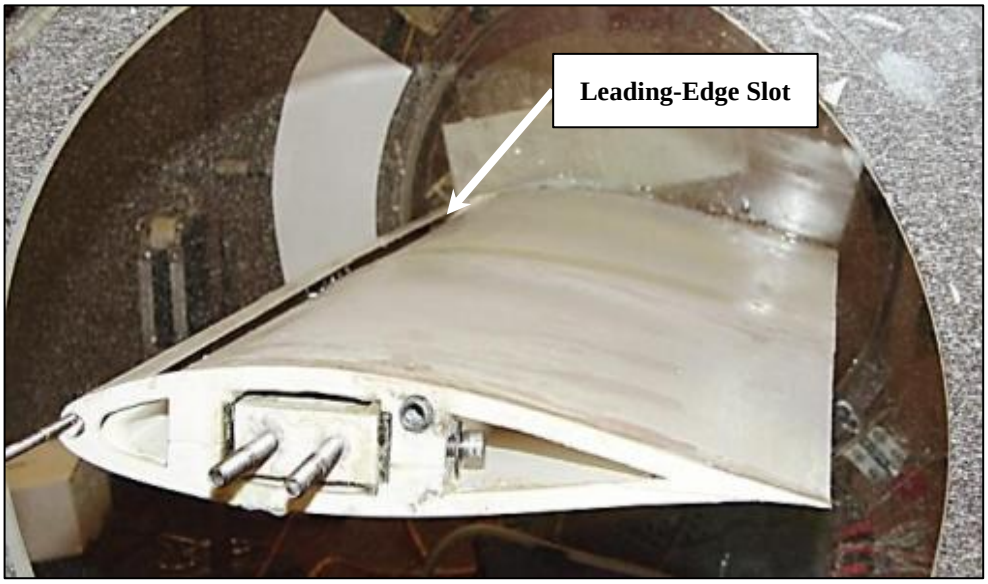

Figure 3.5. Photo of the NACA 63_3-418 airfoil indicating leading-edge slot location

The second passive flow control design combined the leading-edge slot, described previously, but with the addition of an oscillating structure at the slot exit. A design challenge of incorporating the oscillating structure involves optimizing of physical and geometrical parameters (e.g., length, rigidity and thickness) so that vibrational resonance occurs at a reduced excitation frequency (F^+) of approximately unity. The first series of tests were conceptual, intended to validate that the structure would oscillate in an unsteady flow field and that the stochastic loads would reduce. However, the attachment method and thickness of the flapping surface produced a premature transition. Design development was improved for both construction and mounting techniques and resulted in a more favorable aerodynamic response.

Figure 3.6. Photo of the NACA 63_3-418 airfoil indicating slot-flap location

The "baseline" slot-flap configuration, shown in Figure 3.6, was a fiberglass composite with a two-ply fiberglass layup and an epoxy-resin sealant resulting in 0.012 ± 0.001 inch (0.31 ± 0.03 mm) total thickness. The slot-flap was trimmed to a width of 1.55 ± 0.05 inch (3.9 ± 0.1 cm) and a length equal to the span of the airfoil. The composite was vacuum sealed to a flat surface to eliminate excess span wise non-uniformities. The slot-flap was adhered to the surface of the leading edge slot from 0.06c to 0.08c. The excess length extended freely over the upper surface slot distance. After comparing the leading edge slot to the base-line slot-flap configuration, two additional comparative analysis tests were performed: the first analysis compared variations in materials while the second compared variations in length.

In order to reduce separation encountered by sudden variations in geometry, the oscillating slot-flap was constructed of thin, but structurally robust materials. For an

assessment of the influence of material properties such as thickness and rigidity, two slot-flaps of equal length were compared: (1) baseline fiberglass composite and (2) Mylar plastic. An off-the-shelf Mylar sheet was purchased with a thickness of in 0.035 ± 0.001 inch (0.89 ± 0.03 mm). In addition to having a greater thickness as compared to the fiberglass slot-flap, the Mylar is qualitatively less flexible; however, exact material rigidity was not quantified. For the first comparative analysis, the Mylar sheet was trimmed to the same length as the baseline slot-flap, and adhered to the same location on the leading-edge slat.

For an assessment of the influence of slot-flap length, two slot-flaps of fiberglass composite and of equal thickness were compared: (1) baseline of length 1.55 ± 0.05 inch and (2) equal composite thickness, but of length 0.75 ± 0.05 inch. All physical aspects of the 0.75-inch slot-flap are equivalent to the baseline configuration. Results from these assessments are presented in Chapter 6.

CHAPTER IV

EXPERIMENTAL TEST FACILITIES AND METHODS

Wind Tunnel Parameters

The following experiments were performed in a low-speed wind tunnel located in H.R. Bright Building at Texas A&M University. The wind tunnel is an open-loop configuration with an inlet contraction ratio of 25:1. A series of screen meshing were added at the contraction inlet at 1.5-inch intervals. The layers of screens help to streamline the flow entering the test section by breaking down large-scaled flow non-uniformities. The wind tunnel is equipped with a Plexiglas test section with a length of 50 inches (127 cm) with an 18-inch (46-cm) by 18-inch (46-cm) cross section. The test section flow speed was maintained at 20 m/s for the testing process, corresponding to a chord Reynolds number of 3.0×10^5 for the model used. Turbulence intensity measurements were acquired with a hotwire anemometry system and were found to be less than 0.5% for this tunnel at a velocity of 20 m/s.

To correct for flow constraints generated by the presence of the test section walls, boundary corrections were applied to the resulting lift, drag, and pitching moment as well as the free-stream conditions and angle of attack. A brief description of the application of boundary corrections follows: As flow encounters an object in a wind tunnel test section, streamlines are constrained by the presence of the physical boundary. This aerodynamic response agrees with basic principles of conservation of momentum and conservation of mass. Streamline constrictions act as a Venturi nozzle, increasing

the flow velocity over the airfoil, providing corresponding alterations in surface static pressure, lift, drag, and pitching moment. For an enclosed test section, the lift increases and the drag decreases, additionally resulting in variations in geometrical and effective angles of attack. Empirical relations have been developed that correct for these increases and represent the aerodynamic response of the airfoil profile in true free-stream conditions. These relations, including that of solid blockage and streamline curvature, were applied to the experimentally attained measurements and follow the approach detailed in Barlow [56].

Instrumentation

Twelve Honeywell TruStability silicon pressure transducers were used to measure the model surface pressure and the free-stream conditions. The manufacturers state that these transducers have an amplified analog output with a resolution of 0.03% of the full scale (FS) value (1.5 Pa) and an accuracy of 0.25% FS (12.5 Pa) with a total error bar uncertainty of 2% FS (50 Pa). The internal volume was measured as 85 ± 5 mm^3 and the manufacturer stated frequency response was 1 kHz (1 ms response time). Each transducer was individually linearly calibrated using a compressed air flow controlled calibration system, from which a five-point calibration curve was established relating pressure to voltage. For the transducer calibration procedure, pressures were validated against a 590 Barocel pressure transducer with a range of ±100 Torr and an accuracy of 0.15 Torr (20 Pa).

Free-stream test conditions were measured by an upstream pitot-static tube. The pitot tube was positioned in the wind tunnel at the inlet of the test section, but upstream of the disturbance generator. Tubing from the static and total pressure leads from the pitot tube were connected to a Honeywell differential pressure sensor, from which the dynamic free-stream pressure was obtained.

The unsteady test conditions required coherent measurements of the 31 surface pressures and the corresponding free-stream dynamic pressure; however, only 12 pressure transducers were utilized for measurement acquisition. This approach required pressures to be subsequently measured in three intervals for each angle of attack increment. Additionally, the transducers were tared to zero-pressure before each interval measurement series. To temporally align the unsteady datasets, the measurements were phase referenced. An unsteady impulse was generated by applying a voltage step function to the linear solenoid, which in turn actuated the upstream disturbance airfoil. This applied voltage was monitored and used as a starting reference point for phase synchronization. To reduce random uncertainties, the phase-referenced pressures were averaged over nine test samples. Unsteady pressure measurements are further addressed in Chapter 5.

An NI LabView program was developed that helped time and sequence data acquisition using an NI-DAQ 6211 data acquisition board. The NI-DAQ has a maximum analog sampling rate of 250 kHz with 16 analog port inputs and 2 analog outputs. Voltage from the 12 differential pressure transducers was sampled at a rate of 1 kHz for a total duration of 3 s. Sampling was initiated 0.5 s before the upstream

disturbance was applied and continued sampling 2.5 s after the disturbance was applied. Finally, to allow for the system and flow to return to steady state, a 2-s wait period was added before sequential tests were performed. An individual data file was written for each angle of attack at each sensor rotation interval and actuation duration period. An analog impulse was sent from an analog output port to the solenoid to actuate the upstream disturbance. This actuation voltage was also monitored and recorded.

Hot-wire anemometry was used to quantify the coefficient of momentum and to characterize the transient load excursion generated by the upstream disturbance. The anemometer was a TSI IFA 300 constant-temperature anemometer and the hot-wire probe was a TSI 1201. The hot wire was positioned directly behind the slot and angled perpendicular to the curvature of the airfoil because the jet was directed tangentially to the surface. To avoid wall interactions, the probe was positioned 6 in from the wind tunnel wall in the span-wise direction. Hot-wire voltages were sampled at a rate of 1 kHz by the NI DAQ board and were synchronized with surface pressure measurement acquisition. The hot wire probe was calibrated before each test series using King's Law, which relates voltage to velocity as

$$U^{0.45} = AE^2 + B \tag{4.1}$$

where U is the velocity component parallel to the free stream, E is the hot wire voltage, and A and B are constant coefficients established from calibration.

Upstream Disturbance Generator

Wind turbine blades undergo unsteady aerodynamic loadings from to both periodic and aperiodic sources [4]. This research focuses on aperiodic contributors (typically large, unsteady wind gusts), which required the development of an experimental modeling technique that represents these conditions. Examination of environmental free-stream flow conditions shows that incoming winds have differing speeds, various angles of attack, and add circulation because of vortices in the free stream. Considering the stochastic nature of wind gusts, an upstream disturbance generator was chosen to model the unsteady environment.

A variety of wakes and vortex shedding patterns may be formed by oscillating an airfoil in a free stream [55]. However, it was not an objective of this research to fully describe the highly complex vortex-blade interactions or to study all the formations possible, but to provide a comparable representation of the coherent structures exhibited in turbulent winds that interact with wind turbine blades. This section validates these objectives of the upstream disturbance and verifies that the disturbance generated is comparable to observed vortex/blade interactions and is experimentally repeatable.

Figure 4.1 shows a diagram of the upstream disturbance apparatus. The upstream disturbance airfoil is a NACA 0012 airfoil with a 6-in (15-cm) chord. The airfoil has a polystyrene foam core with a fiberglass layup. A 0.5-in aluminum rod serves as a support and rotation axis around the quarter chord. The rod is attached to the foam using epoxy-resin, which transfers the motion from the linear actuator to the airfoil. The disturbance apparatus was located two chord-lengths (18 in) upstream from the main

airfoil and set at a zero angle of attack in the un-actuated position. Additionally, the disturbance airfoil was vertically offset of a distance of half the main airfoil chord length (4.5 in).

A linear actuator was used to deflect the disturbance airfoil through the desired range of motion. When actuated, the upstream disturbance deflects from the nominal position at zero degrees to a positive angle of attack and then returns to the nominal position, resulting in an impulse-pitching motion. The actuator is a high-force, open-box frame, push-style linear actuator capable of generating 21 lb_f when actuated. A spring was attached to the actuator to provide a controlled resistance to the motion and return the airfoil to its nominal position at zero degrees angle of attack. The motion of the linear actuator is transferred to the airfoil through a control arm and pitch-control horn. The actuator system is connected to a 0.5-in (13-mm) rod that runs through the quarter chord

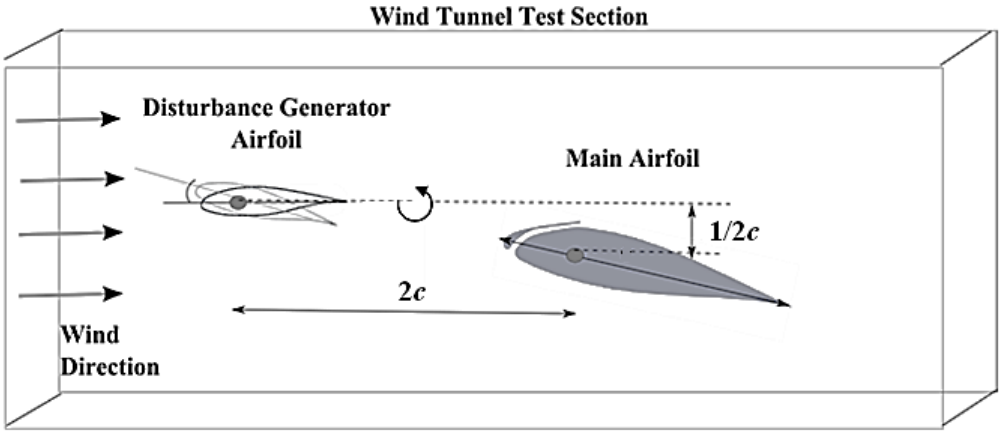

Figure 4.1. Illustration of unsteady disturbance generator

location of the upstream disturbance airfoil. A fly-wheel was mounted externally on the upstream airfoil quarter-chord support rod to add inertia and allow for greater control of the actuation deployment speed. Figures 4.2–4.5 show the test section configuration and the linear actuator apparatus.

Load Excursion Characterization

Characterization of the unsteady load excursion from the upstream disturbance is required before mitigation methods could be established. It was not an objective of this research to fully describe the highly complex vortex-blade interactions or to describe the various formations possible because this is an extensive area of research and is beyond the scope of the present work. Alternatively, the function of incorporating the upstream disturbance was to represent the coherent structures observed in turbulent winds and wind gusts that interact with a wind turbine blade. Namely, the objective of the upstream disturbance generator is to produce a repeatable, unsteady load excursion representative of wind gusts and other environmental contributors.

The transient loads produced by the upstream disturbance generator are influenced by the pitch rate (A) of the upstream airfoil and is characterized as $A = \alpha_D c_D / U_\infty$ where α_D is the rate of change of angle of attack of the deployment c_D is the chord of the upstream disturbance airfoil, and U_∞ is the free-stream velocity. Three variations in deployment

Figure 4.2. Photo of wind tunnel test section and contraction inlet

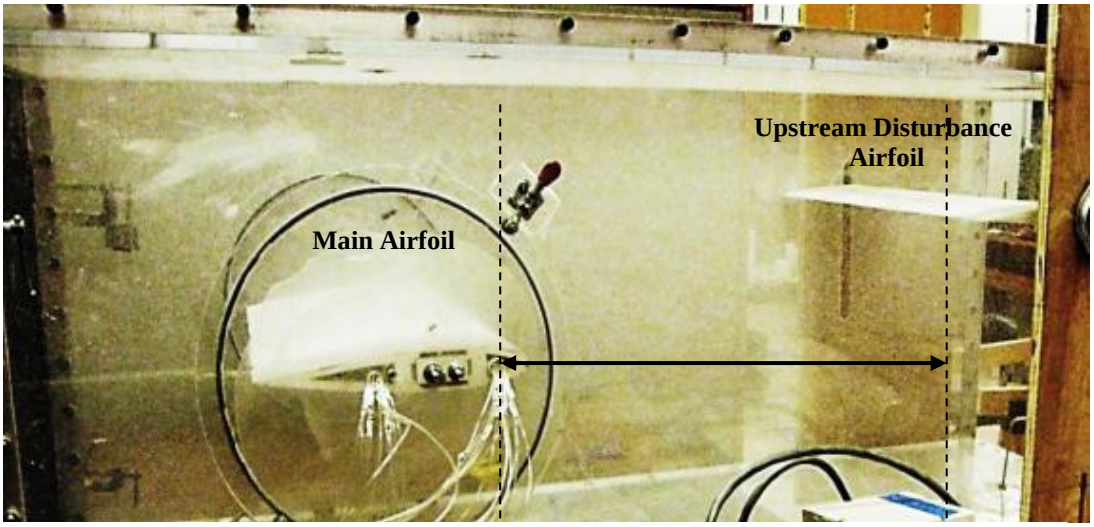

Figure 4.3. Photo of wind tunnel test section showing main airfoil and upstream disturbance airfoil

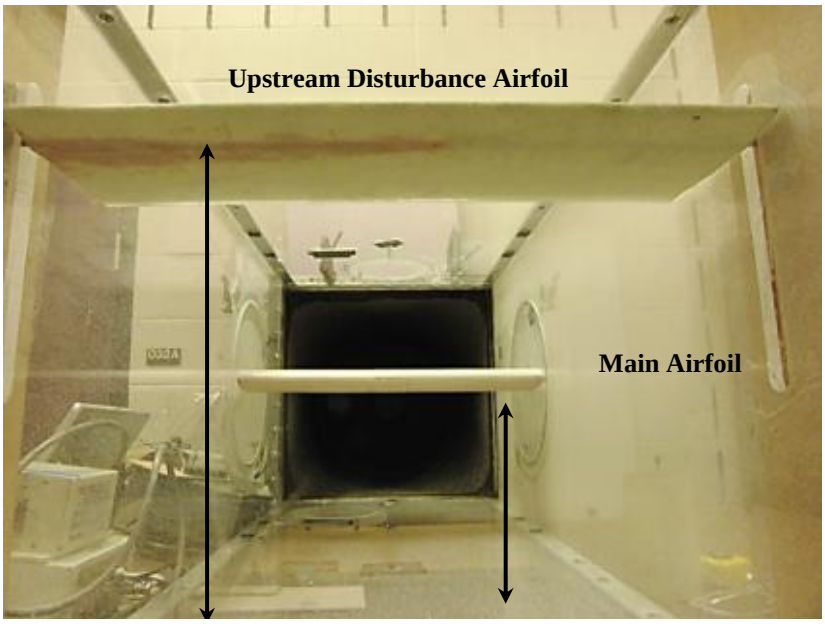

Figure 4.4. Photo of interior of the test section highlighting the vertical placement of the upstream disturbance airfoil and main airfoil

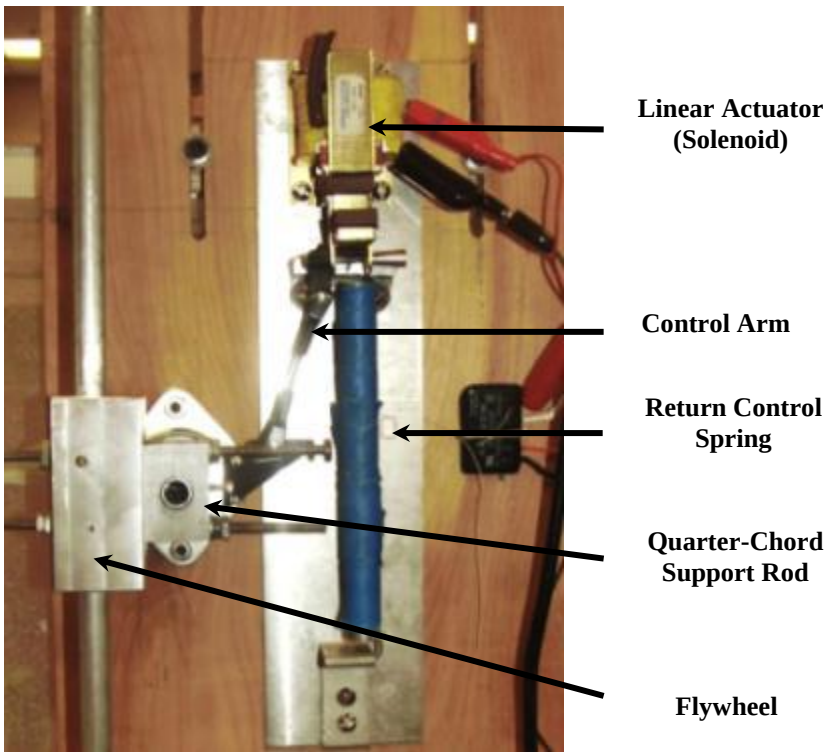

Figure 4.5. Photo of linear actuator apparatus used to deflect the upstream disturbance airfoil

were examined of maximum deflection angles (α_D) of 3˚, 15˚, and 25˚ with an angular velocity of 4.2, 3.7, and 4.9 rad/s corresponding to non-dimensional reduced angular deflection frequencies of 0.032, 0.028, and 0.037, respectively. A high-speed digital camera set to 420 frames per second (fps) and image processing software were used to determine the angular velocity of the deflection. To quantify the signature of the upstream disturbance, velocity measurements were acquired using hot-wire anemometry. For these measurements, the main airfoil was removed from the test section and the hot-wire probe was aligned perpendicular to the flow and positioned approximately at the quarter-chord location of the main airfoil when mounted. Figure 4.6 shows the phase averaged unsteady response over 100 deflection periods as measured by the hot-wire probe versus reduced time, $\tau = U_\infty t/c$. From the hot-wire data, the transient load gain was quantified as the percent change between the maximum and minimum (x_M) load excursion as compared to the mean value ($\overline{x}$) defined as

$$\% \text{ Change} = \frac{x_M - \overline{x}}{\overline{x}} \times 100 \tag{4.2}$$

Table 4.1 delineates maximum and minimum velocity excursions. As the maximum deflection angle of the upstream disturbance increases, the percent change with respect to the mean free-stream velocity increases, so that the pitch rate of $A = 0.037$ with a deflection angle of $\alpha_D = 25^\circ$ generated the largest percent change in velocity and $A = 0.032$ with a deflection angle of $\alpha_D = 3^\circ$ generated the smallest.

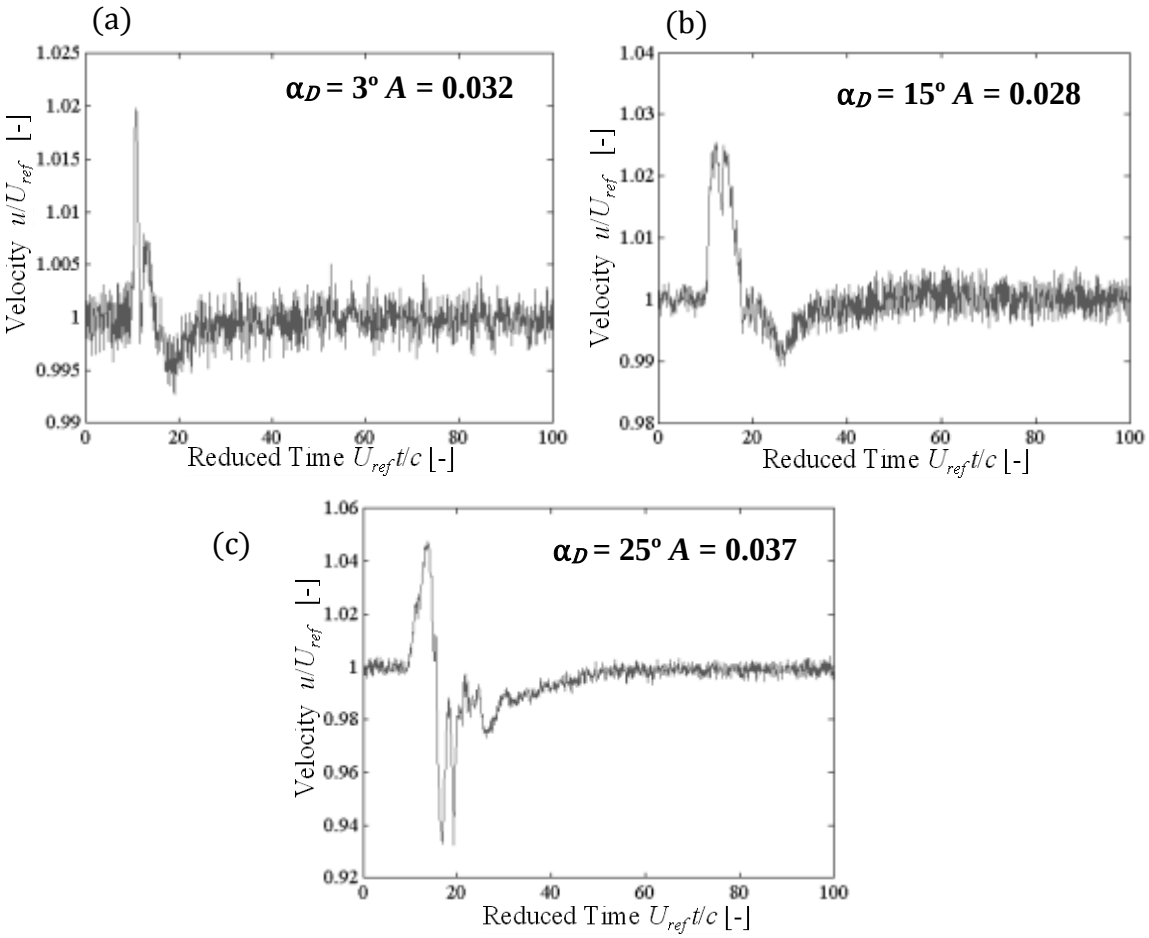

Figure 4.6 Hot-wire measurements of velocity vs. reduced time of the transient load excursions for and upstream deflection of α_D = (a) 3˚, (b) 15˚, and (c) 25˚

Table 4.1. Summary of upstream disturbance generator controls and the resulting percent change as compared to the free-stream conditions

Pitch Rate [-] $A = \alpha\, c_{DG}/U_\infty$	**Max Angle of Deflection**	**Max $\Delta u/U$ % Change**	**Min $\Delta u/U$ % Change**
0.032	3˚	2.1%	0.6%
0.028	15˚	2.5%	1.0%
0.037	25˚	4.8%	6.6%

Figure 4.7 shows the effects of the load excursions on lift and moment coefficients are examined and the time histories. Observing the transient time history of lift at a fixed maximum lift angle of attack of 11˚ for A = 0.032 and α_D = 3º, three significant deviations from the steady value are realized: (1) a large increase in lift, (2) followed by a sharp decline, (3) succeeded by a second smaller increase in lift. Assuming a negative vortex of counterclockwise circulation is shed from the disturbance generator, the vortex initially impacts the leading edge of the airfoil contributing to added circulation effects that positively increases lift. This response is attributed to an increase in effective angle of attack, which becomes greater as the distance between the vortex and the main airfoil decreases. After reaching a maximum, there is a dramatic decrease in lift as the vortex passes over the leading edge. Finally, the vortex passes the upper surface trailing edge and moves into the wake, generating a second increase in lift that decreases as the vortex propagates downstream.

For A = 0.028 and α_D= 15º, similar temporal lift deviations are observed as compared to steady-state values. However, the maximum and minimum deflections for this test case as compared to A = 0.032 and α_D= 3º are larger in magnitude. The impulse actuation of A = 0.037 and deflection α_D = 25º exhibited a differing trend. Reviewing the time history of this test case shows three increases in lift and two declines, with the dominant deflection peak occurring on the second deviation region. This result indicates multiple shed vortices during the actuation period.

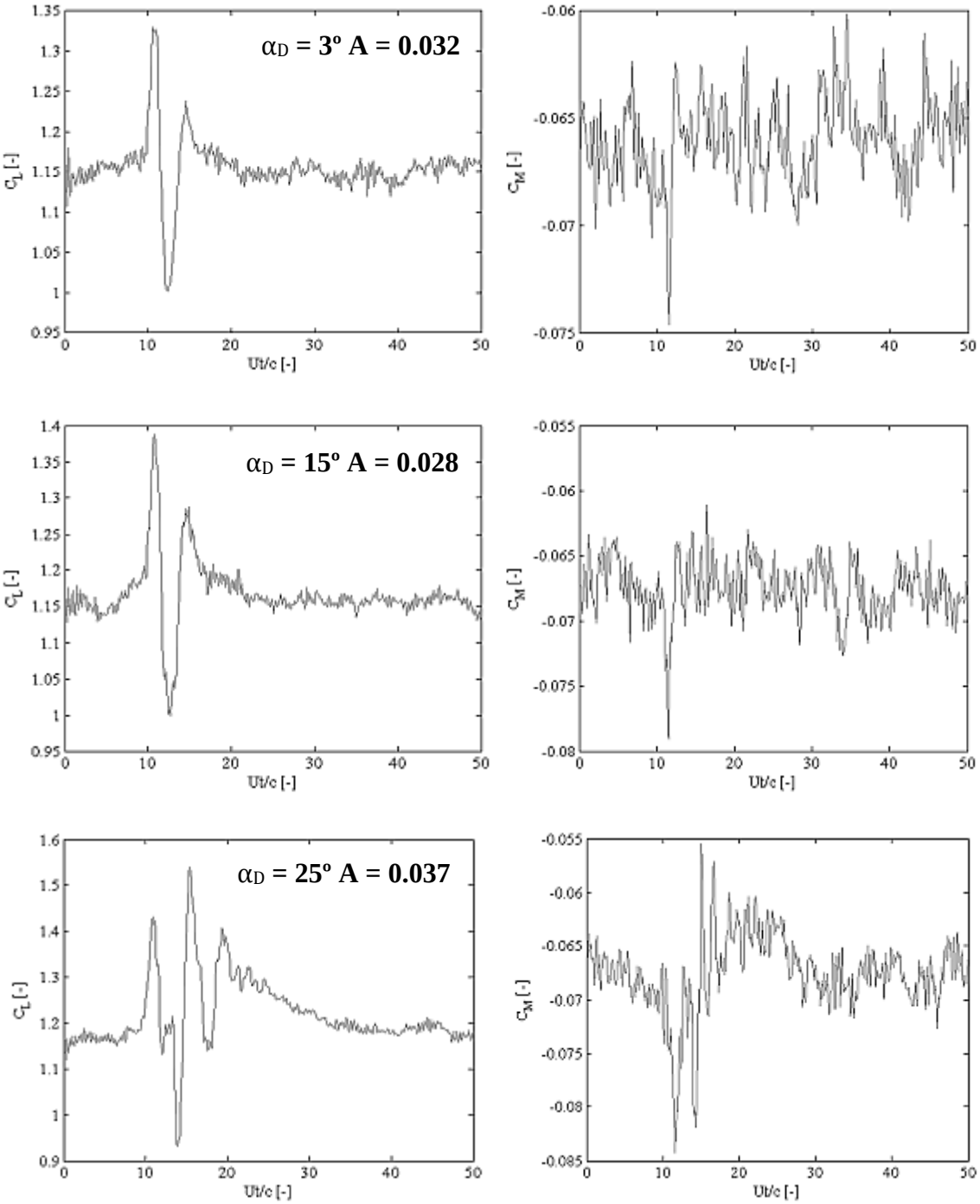

Figure 4.7(a-f). NACA 63_3-418 clean airfoil C_L (left) and C_M (right) unsteady time history at $\alpha = 11°$ for various pitch rates.

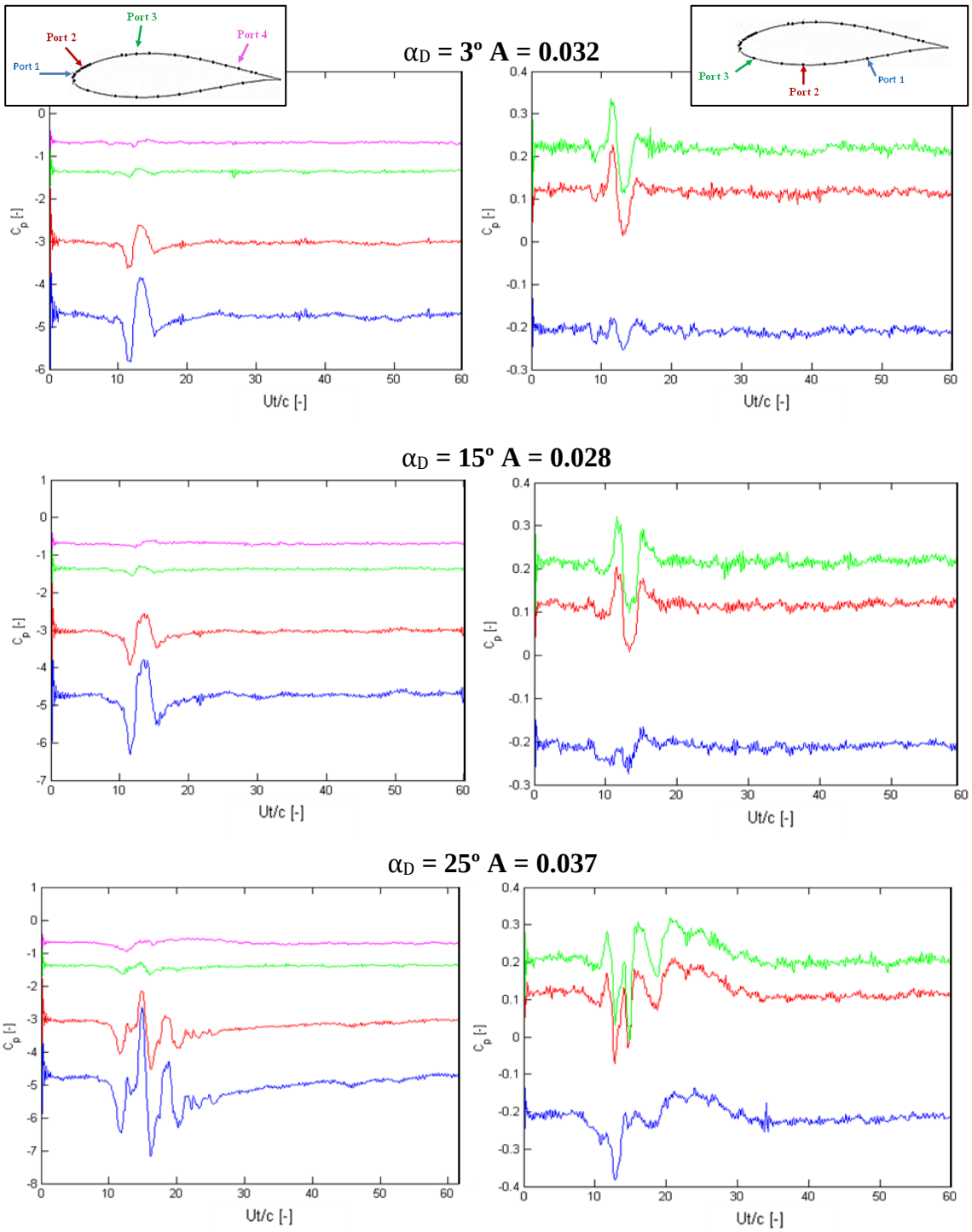

Figure 4.8(a-f). C_p unsteady time history for the suction surface (left) and pressure surface (right) of a NACA 63_3-418 clean airfoil at $\alpha = 11^\circ$ for various pitch rates.

The coefficients of lift and moment are discrete integrations of the surface pressures, and thus only provide a general depiction of the load excursions. The vortex interaction generated by the oscillating upstream disturbance airfoil is more specifically visualized by examining changes in the surface pressure distribution on the main airfoil. Figure 4.8 shows the C_P measurements versus reduced time for Ports 2, 6, 13 and 20 along the suction surface and Ports 25, 28 and 30 along the pressure surface at the maximum lift angle attack of 11º. Plotting the time history of the all of the surface pressures in a single plot would be unreadable, thus seven ports were selected that represent the pressure excursions for the respective chordwise location. Similar trends are viewed in the pressure time history as compared to the transient lift response. The vortex-body response shows an increase, followed by a decrease and a subsequent increase in suction on the upper surface. The reverse response is observed on the lower surface with an initial increase in pressure, followed by a decrease and a second smaller increase in C_p.

The reduced frequency, k, can be used to describe the unsteadiness of the incoming flow conditions as seen by the main airfoil, and is defined as $k = f\pi c/(2U_\infty)$ where f is the frequency of the disturbance and c is the main airfoil chord length. To extract dominant frequency information of the transient load response, a Fast Fourier Transform (FFT) was applied to surface pressure measurements. For all three reduced angular deflection frequencies, the dominant frequency resulting from the load excursion was 20 Hz. Appropriately, a FFT of C_L time history also resulted in 20 Hz for all three cases. As a result, the corresponding reduced frequencies for the three variations were 0.72. As

stated in the literature review, unsteadiness generated by rotational effects are on the order of 1-P to n-P where P is the rotational frequency of a single blade rotation and n is the number of blades. For a commercial HAWT, this frequency range corresponds to a reduced frequency range of 0.05 to 0.5 [4, 37] with variations depending on outboard, mid, or inboard chord lengths. However, aperiodic unsteady flow conditions, such as that of large wind gusts, are of a smaller time scales and higher frequency ranges. While the reduced frequency of the experimental setup is greater than that associated with rotational effects of a commercial HAWT, the frequency range and impulse-like loading is comparable to aperiodic atmospheric and inflow conditions as those seen on a horizontal axis wind turbine blade.

Reduced Excitation Frequency Algorithm

The slot-flap configurations were designed such that the structures oscillate under the influence of the surrounding fluid flow. As such, a non-invasive measurement technique was required to quantify the oscillation frequency. A high speed digital camera set to a frame rate of 1000 fps was used to visually capture this frequency. The video was imported to Matlab and processed using the following algorithm.

Figure 4.9 is a flow chart showing the steps of this scheme. The principle of the image processing investigates time history of individual pixels. When the slot-flap is in frame, the pixel turns “on” and as the slot-flap moves out of frame the pixel turns “off”. This approach is a binary method and is dependent on the image intensity threshold. For a more analog representation, the norm of the pixel’s true color vector [R, B, G] is

calculated for each frame. This process is the first stage in the algorithm. For the second stage the power spectral density of the pixel time history is analyzed using the pwelch function from the Matlab Signal Processing Toolbox. This function uses Welch's method to divide the time history into eight overlapping segments, each with 50% overlap, from which periodograms are computed and averaged. The function also incorporates a Hamming window of the same length as the segments. The third stage involves utilizing a peak finding program, which extracted the three most dominant frequencies. The process was repeated for eight 512 time series over a 2 second time period for each pixel from the selected image window of 14 x 6 pixels. The results of this survey are presented in a histogram and are addressed in Chapter 6.

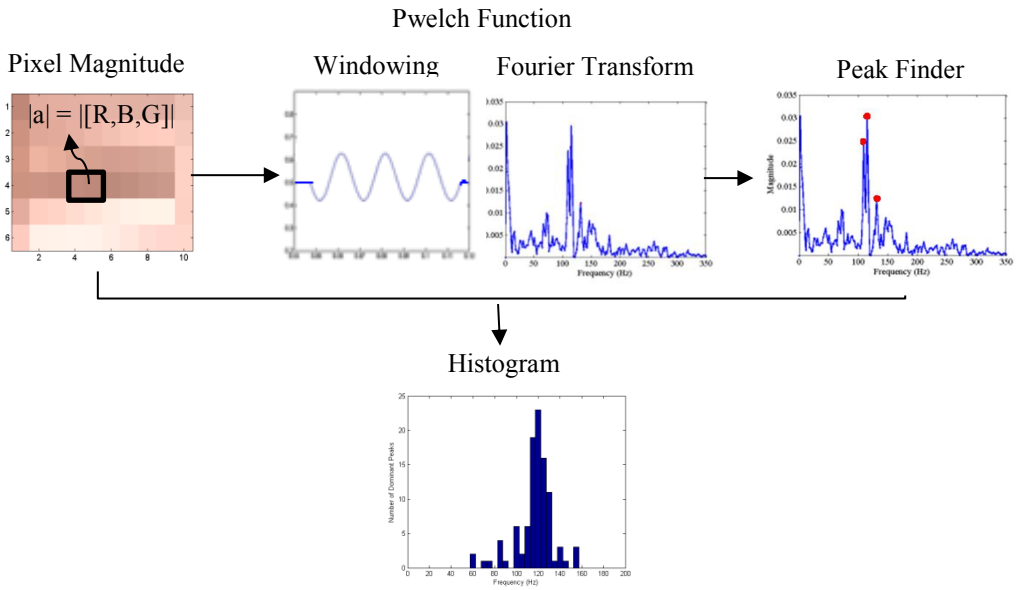

Figure 4.9. Reduced excitation frequency algorithm flow chart

CHAPTER V

UNSTEADY AERODYNAMIC TESTING

Unsteady Pressure Measurements

Steady pressure measurements are common in wind tunnel experimentation, utilizing surface pressure integration to determine aerodynamic properties of lift, drag, and pitching moments. This experimental measurement technique involves employing tubing systems that connect surface pressure ports to pressure transducers. Figure 5.1 shows an example of the schematic of a basic system showing a pressure transducer connected to a tubing system of inner diameter ID and length L.

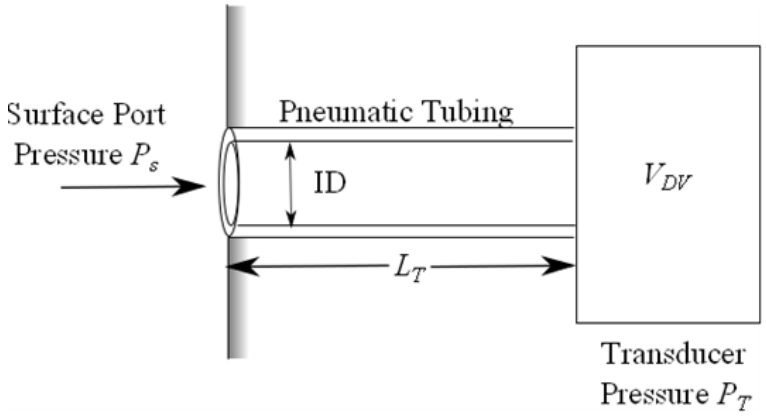

Figure 5.1. Schematic of a basic pressure tubing system

For steady flow conditions, the pressure as measured by the transducer P_T is equal in magnitude to the true surface pressure P_s. However, in an unsteady flow field, inertial effects from the fluid-tubing interactions distort the amplitude and phase of the unsteady pressure wave. The pressure measured by the transducer no longer represents the local

surface pressure. This error propagates through the data analysis, leading to incorrect representation of force and moments on the airfoil.

Ideally, fast-response, surface-mounted pressure transducers would be employed to make unsteady measurements. These sensors, such as those manufactured by Kulite or Endevco, have minimal measurement errors from surface mounting, and additionally have a negligible internal transducer volume, which provides a high frequency response. However, these are fragile, easily damaged, and prohibitively expensive. An alternative approach is to implement a conventional pressure system (Figure 5.1) and then apply a correction, typically by developing a system transfer function. For the results presented in this thesis, a bench-top acoustic procedure was used to determine an experimental transfer function of the tubing system. This was compared to an analytic pneumatic tubing model for validation purposes. Finally, to reconstruct the actual surface pressures, a spectral decomposition algorithm incorporating the experimentally derived transfer function was applied to all transducer-measured values.

Pneumatic Tubing Transfer Function

The transfer function for the pneumatic system was experimentally determined using an acoustic bench-top experiment. The basic experimental procedure involved comparing a known, oscillating pressure of a specified frequency to the pressure as measured by the pneumatic tubing system. Both pressures were then converted the frequency domain. The transfer function for the specified oscillation frequency ω was

the ratio of the transducer measured pressure $P_T(\omega)$ to the actual pressure $P_S(\omega)$ in the frequency domain, expressed in Equation 5.1.

$$TF = \frac{P_T(\omega)}{P_S(\omega)} \tag{5.1}$$

The process was repeated at 5-Hz increments for a range of 5–260 Hz. The result was a discretized transfer function as a function of frequency. As a method of validation, the resulting function was then compared to the widely acknowledged and accepted Tijdeman and Bergh analytic pneumatic tubing transfer function.

Tijdeman and Bergh [58] derived an experimental model for determining a pneumatic tubing transfer function based on simplified fundamental flow equations (i.e., Navier-Stokes, continuity and conservation equations). This analytic relation is reduced from the governing equations based upon assumptions relating to small sinusoidal disturbances, circular tubes with internal radii much less than the tubing length, and laminar flow throughout the system. For multiple tubes with differing inner diameters and several connecting volumes, the non-linear, infinite-order frequency response model may be used to account for pressure attenuation in a tubing system. For the experimental system described in Chapter 3, only a single tubing system was used for which the numerical relation reduces to

$$TF = [\cosh\ \Gamma\, L\ + \frac{Vv}{V_T}\ \ \sigma + \frac{1}{pc}\ \ k\, \Gamma\, L \sinh(\Gamma\, L)]^{-1} \tag{5.2}$$

where V_v is the internal "dead-volume" within the transducer, V_T is the tubing internal volume, σ a dimensionless increase in the transducer volume due to diaphragm

deflection, *pc* is the polytrophic constant for the volumes, and Γ is the propagation constant defined as

$$\Gamma = \frac{\omega}{a}\ \frac{\gamma}{k}\frac{J_o\ \ i^{\frac{3}{2}}s}{J_2\ \ i^{\frac{3}{2}}s}^{1/2} \tag{5.3}$$

for which a is the mean velocity of sound, J_n is the Bessel function of the first kind of order *n*, γ is the ratio of specific heats and *K* is the polytrophic factor defined as

$$K = \ 1 + \frac{\gamma - 1}{\gamma}\frac{J_2\ \ i^{\frac{3}{2}}s\sqrt{Pr}}{J_0\ \ i^{\frac{3}{2}}s\sqrt{Pr}}^{-1} \tag{5.4}$$

and *s* is the shear wave number

$$s = \frac{\mathrm{ID}}{2}\frac{\overline{\omega\rho}}{\mu} \tag{5.5}$$

Bench-Top Tubing Experiments

To determine the pneumatic tubing transfer function, the transducer-measured pressure must be compared against a known, unsteady pressure measurement. A bench-top experiment was conducted to develop a transfer function that relates the actual unsteady, surface pressure to the transducer-measured pressure (Figure 5.2). The calibration method generates a repeatable, fluctuating pressure at the inlet of the tubing system. A loudspeaker is used as the driving element, and creates pressure oscillations from acoustic waves with controlled amplitude and wavelength. This method of experimentally determining the transfer function accounts for the unknowns of the

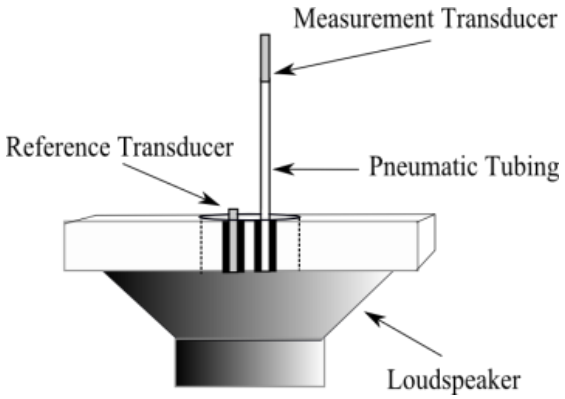

Figure 5.2. Diagram of a bench-top acoustic experiment to establish the pneumatic tubing transfer function

tubing system including the effects of tubing length and internal dead-volume within the transducer.

The speaker used was a 10-in Pioneer subwoofer with a rated frequency response between 20 and 280 Hz. A flat plate was mounted to the surface and created a sealed cavity without leakage. Two holes were drilled into the plate of diameters 1.70 ± 0.03 mm (0.067 ± 0.001 in) and 2.46 ± 0.03 mm (0.097 ± 0.001 in), and are separated by a distance of 5.84 ± 0.03 mm (0.230 ± 0.001 in). Both holes are approximately equidistance from the direct center. A Model 8507C-2 Endevco pressure transducer of outer diameter 2.34 ± 0.03 mm (0.092 ± 0.001 in) was mounted and sealed in the first pressure opening. The Endevco has a range of ±2 psi and a total uncertainty relating to non-linearity, hysteresis, and non-repeatability of 0.79% full scale (110 Pa) as determined by the manufacturer. This sensor was selected because it is a fast-response, surface-mounted transducer. The manufacturer-stated internal volume of this transducer is 5.0×10^{-5} in^3 (0.0008 mL), which is considered negligible. In addition, the transducer

is flush mounted, so that the pressures measured do not require a transfer function and represent the actual pressure applied to the inlet of the tubing system.

The tubing system is mounted to the second opening to compare to the actual pressure as measured by the Endevco transducer. The tubing used was Scanivalve Tygon tubing of outer diameter of 1.68 ± 0.10 mm (0.066 ± 0.004 in) and an internal diameter of 0.86 ± 0.10 mm (0.034 ± 0.004 in). To validate the transfer function, various tubing lengths were used. The four tubing lengths used were 15.2 ± 0.2 cm, 30.5 ± 0.2 cm, 45.7 ± 0.2 cm, and 61.0 ± 0.2 cm (6, 12, 18 and 24 in respectively).

Unsteady pressures along the surface of the airfoil were taken using 12 Honeywell TruStability low-pressure, differential transducers. Each of the 12 transducers used in the experiment has its own transfer function relating to the internal dead-volume. However, it would be impractical to derive the transfer function for each transducer. Instead, data were collected for four transducers using four different tubing lengths and 52 different oscillation frequencies. Tests were conducted for applied oscillation frequencies from 5 to 260 Hz at 5-Hz increments. An NI Labview program was written that outputs a sinusoidal signal at the desired frequency using a laptop sound card. An auxiliary connection was used to transfer the sine wave to the voltage input of the speaker amplifier. The result of this signal transfer was a low frequency sound as produced by the speaker.

The two transducers were sampled simultaneously by a National Instruments 6211 Data Acquisition Board at a rate of 4 kHz for a duration of 2 s. Additionally, a basic low-pass filter was applied to the data series to eliminate high-frequency noise.

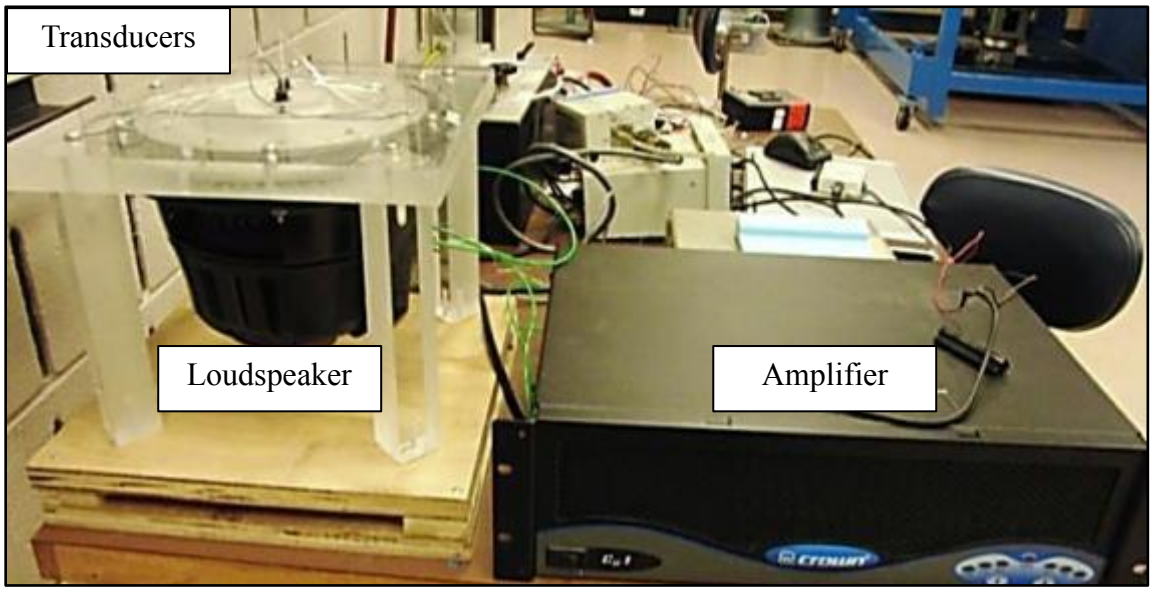

Figure 5.3. Bench-top acoustic calibration experiment to establish the pneumatic tubing transfer function

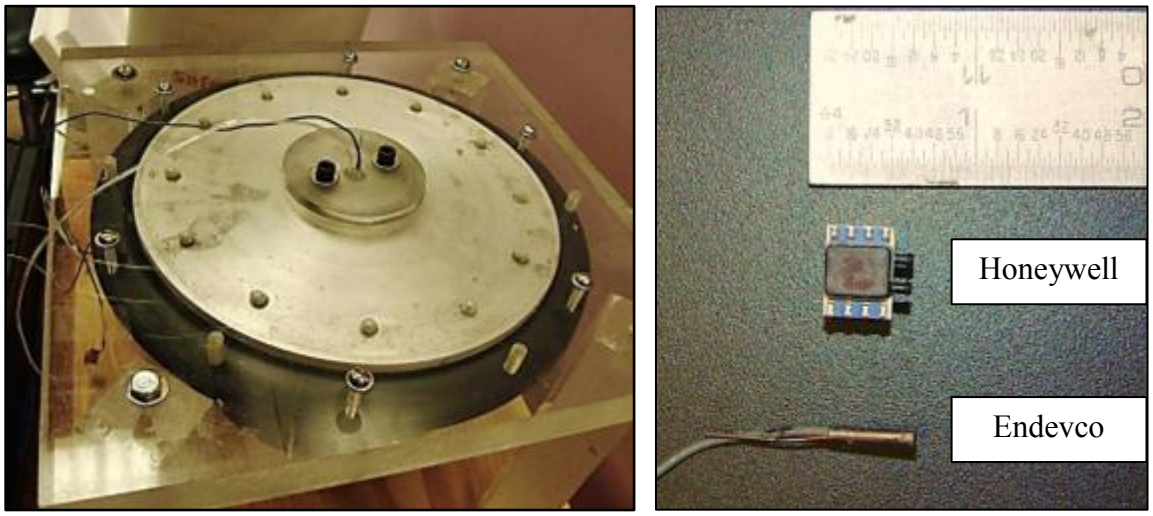

Figure 5.4. *(right)* Picture of the transducer and pneumatic tubing connection. *(left)* Picture of the measurement transducer (Honeywell TruStability) and the reference transducer (Endevco 8507C-2)

The reference and measured pressures were then converted to the frequency domain by taking a FFT of each series and the relation of the transfer function for each oscillation frequency was found by utilizing Equation 5.1.

Transfer Function Comparison

The experimental transfer function outlined in the previous section was compared to the analytic Tijdeman and Berg function. The Tijdeman and Berg relation is parameterized by the tubing diameter, length, and internal volume. The transducer internal volume was found by filling the internal cavities of a Honeywell sensor with water using a graduated pipet and then measuring the volume of the fluid. The internal volume was measured as 85 ± 5 mm^3. Tubing diameter and length are known values; however, the analytic transfer function is highly sensitive to variations in these parameters. Uncertainties in the internal diameter lead to significant shifts in the transfer function. Sensitivity with respect to the measured uncertainty in length was of a lower magnitude, and hence was excluded as a parameter for optimizating of the analytic function.

Figures 5.5–5.8 show the magnitude and Figures 5.9–5.12 show the phase of the comparative analysis of the experimental and analytic transfer functions in the complex frequency domain. The Tijdeman and Berg transfer function was optimized with respect to the inner tubing diameter for the 18 inch tubing length, which was chosen because the reference length as it was the length of the tubing embedded in the airfoil model. The best-fit line resulted from an inner diameter of 0.030 in, which was within the

uncertainty of the manufacturer-stated tubing inner diameter. Tijdeman and Berg also noted similar trends, stating that the analytic function best fit with experimental results when using an effective radius of 2–5% smaller than the mean tubing radius. To examine the effects from sensitivity in diameter, maximum and minimum diameters were analyzed and plotted in the corresponding figures. The maximum and minimum diameters were the effective radius of 0.030 in plus the manufacturer-stated uncertainty of ±0.004 in.

Collectively, the plots indicate that the experimental transfer function agrees well the analytic function. Experimental values in Figures 5.5–5.12 are within the uncertainty bounds of the analytic function for frequencies less than approximately 200 Hz. Additionally, the experimental data points from the four transducers do not significantly deviate from one another, indicating that it is valid to assume negligible deviations in manufacturing between transducers. Small variations in transducer responses also indicate that the established experimental transfer function is valid for all 12 transducers used in the experimental testing phase.

Basic trends are comparable between the experimental and analytic transfer functions. However, the responses from the experimental tests exactly represent the pneumatic system response, where as the analytic function is an approximate fit of the data. Because of this, the experimental transfer function was used for the pressure reconstruction algorithm. To generate a continuous function, the four datasets were averaged and extrapolated around local values of the frequency intervals. A detailed description of the reconstruction algorithm is outlined in the following section.

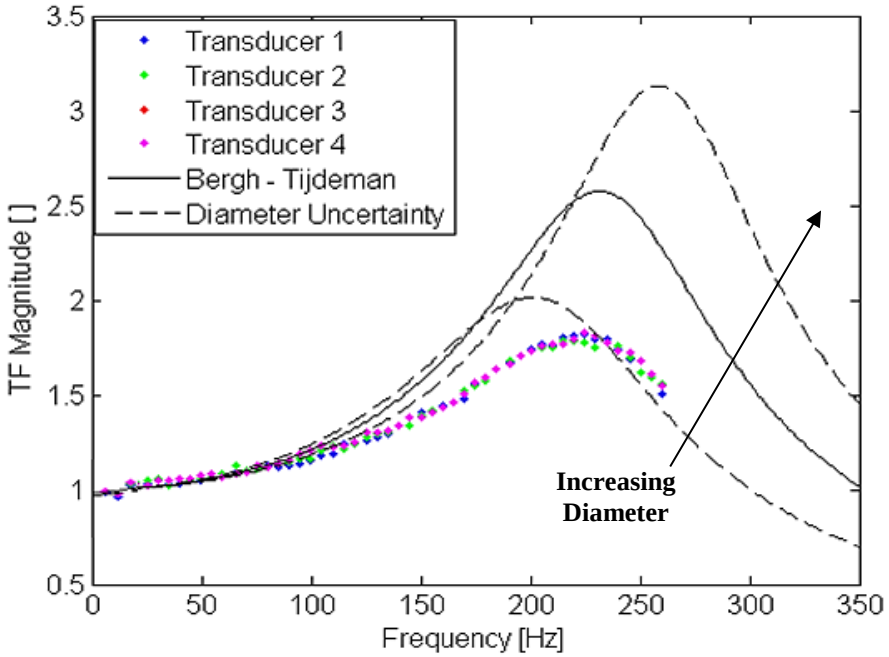

Figure 5.5. Magnitude of pneumatic tubing transfer function for a tubing length of 6 in

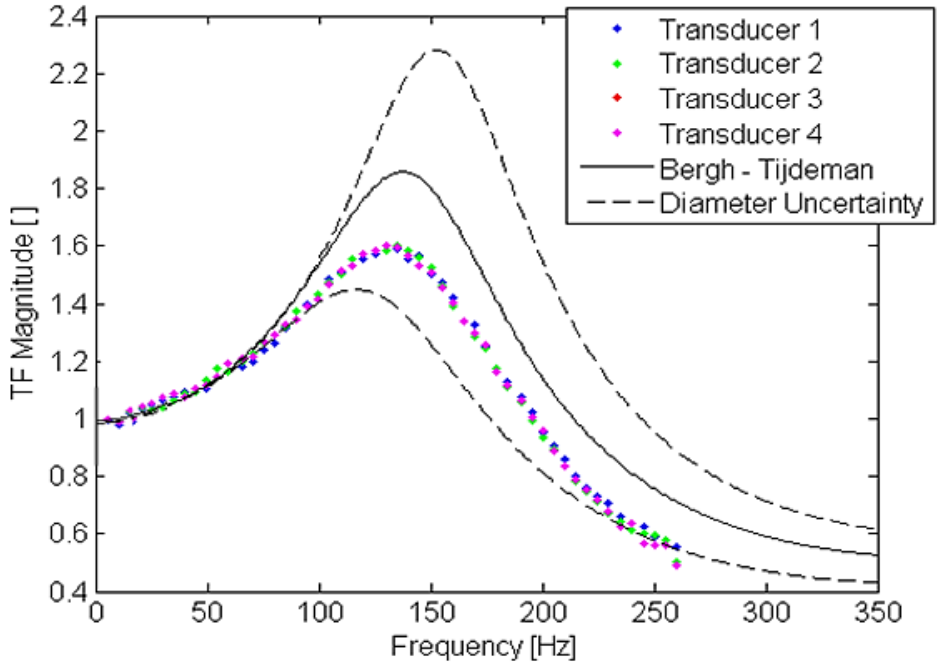

Figure 5.6. Magnitude of pneumatic tubing transfer function for a tubing length of 12 in

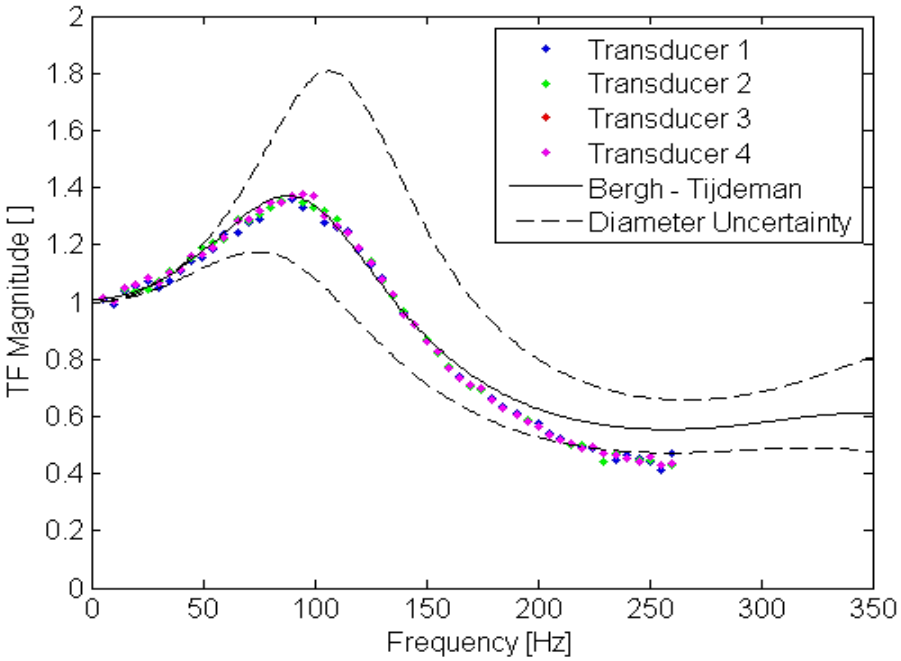

Figure 5.7. Magnitude of pneumatic tubing transfer function for a tubing length of 18 in

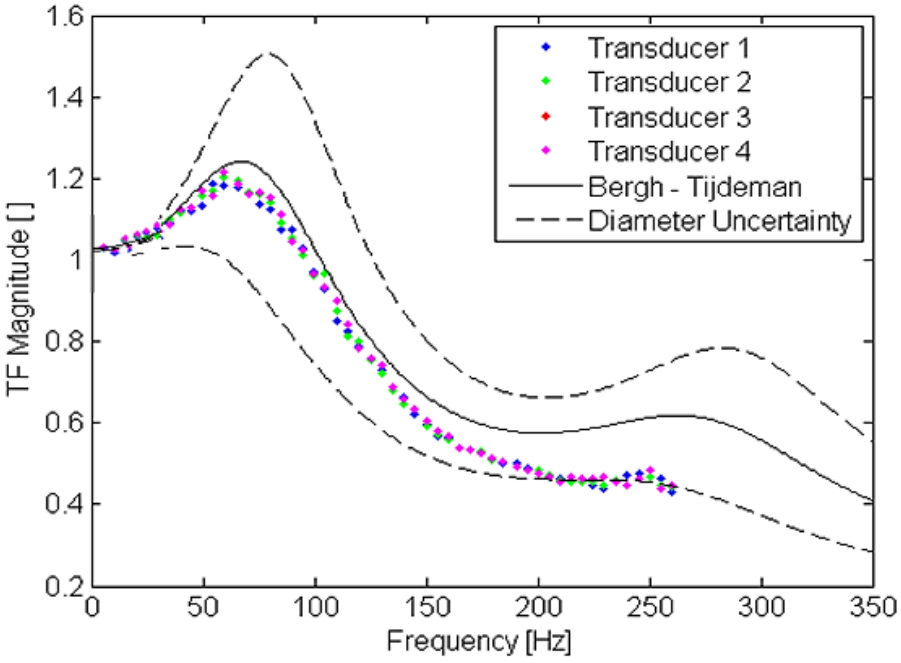

Figure 5.8. Magnitude of pneumatic tubing transfer function for a tubing length of 24 in

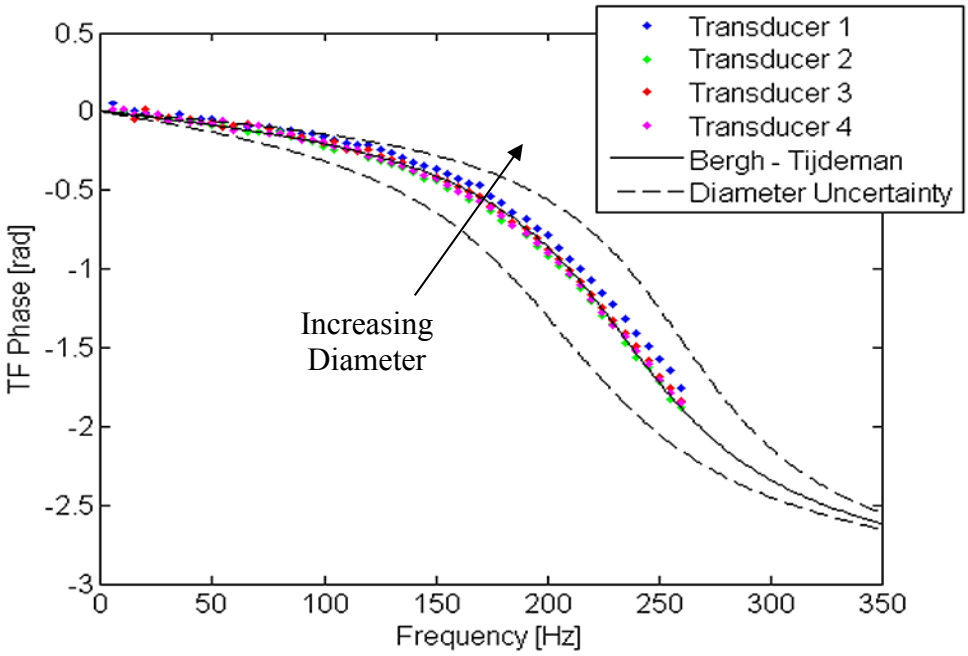

Figure 5.9. Phase of pneumatic tubing transfer function for a tubing length of 6 in

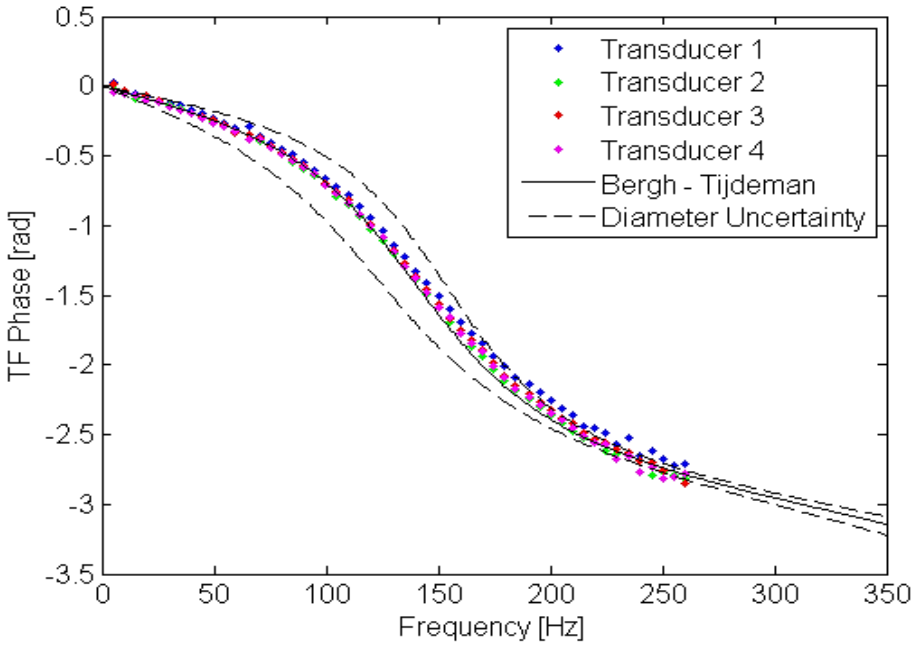

Figure 5.10. Phase of pneumatic tubing transfer function for a tubing length of 12 in

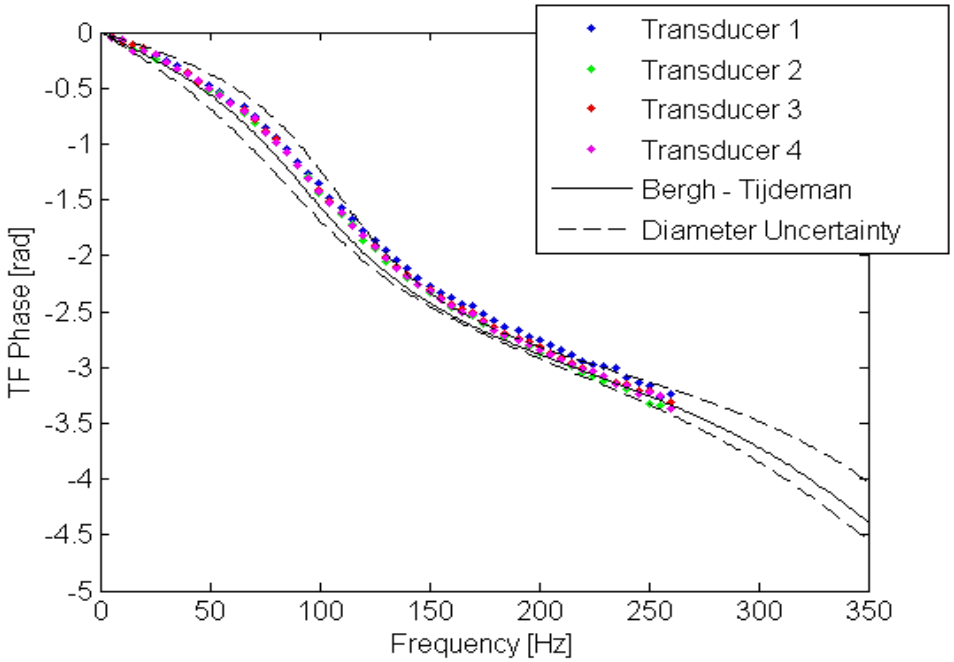

Figure 5.11. Phase of pneumatic tubing transfer function for a tubing length of 18 in

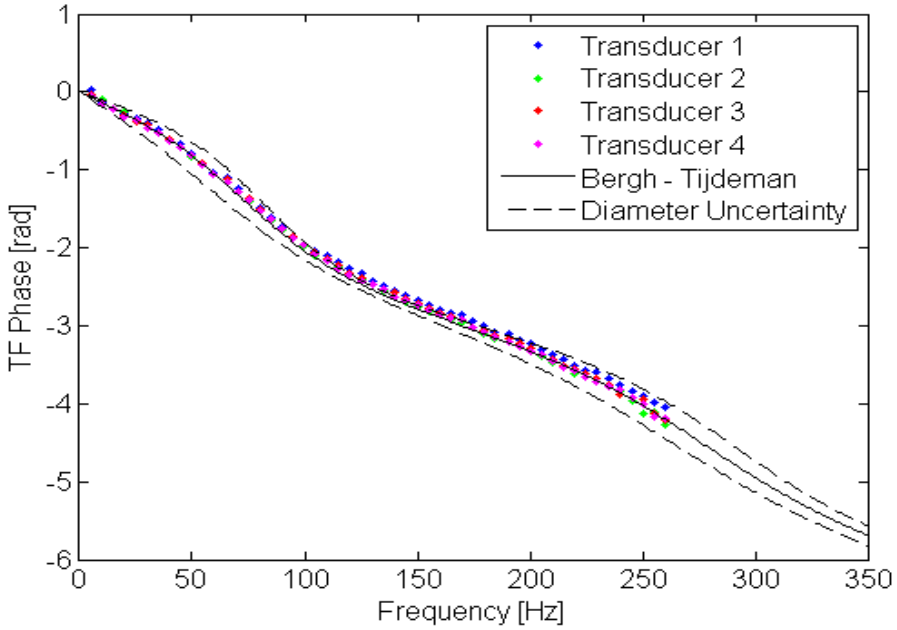

Figure 5.12. Phase of pneumatic tubing transfer function for a tubing length of 24 in

Reconstruction Algorithm

A compensation algorithm was used to convert the transducer-measured pressure to the actual surface pressure. Figure 5.13 is a flow chart showing the steps of this spectral deconvolution scheme. The first stage involves a windowing function. To convert the signal from time to frequency domain, a Fast Fourier Transform (FFT) was used. An inherent property of a FFT is that the transform assumes that the signal is periodic within the sampling series. A basic windowing function is applied for a more accurate transformation of signals that are not perfectly periodic. Additionally, windowing forces zero values at the start and end of the sample series, reducing spectral leakage and creating quasi-periodic trends in an aperiodic signal.

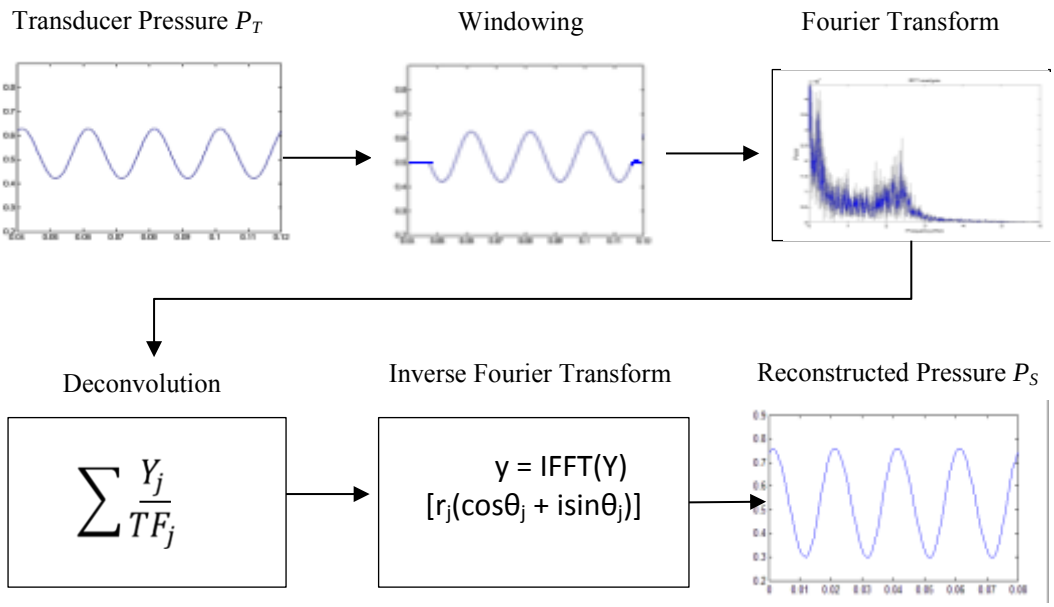

Figure 5.13. Pressure reconstruction algorithm flow chart

In the frequency domain, a deconvolution method was applied. Deconvolution involved dividing the pressure signal by the experimental transfer function described in the previous section. For the fifth stage, the inverse FFT is applied, resulting in the reconstructed pressure applied at the airfoil surface. The amplitude ratio is given as the modulus of the FFT of the signal divided by the magnitude of the transfer function (TF), given by

$$r\ f\ = \frac{|\mathrm{FFT}\ f\ |}{|\mathrm{TF}\ f\ |} \tag{5.5}$$

Similarly, the phase angle relation is the difference between the argument of the FFT and the TF

$$\theta\ f\ = \arg\ \frac{\mathrm{FFT}\ f}{\mathrm{TF}\ f}\ = \arg\ \mathrm{FFT}\ f\ - \varphi(f) \tag{5.6}$$

where φ is the phase angle from the experimental transfer function. Finally, the corrected pressure wave is expressed in complex form as:

$$z\ f\ = r\ f\ [\cos\theta\ f\ + i\sin\theta\ f\ ] \tag{5.7}$$

By taking the inverse of Equation 5.7, the signal is then reconstructed and corrected to represent the actual pressure wave, shown as the last stage in Figure 5.2.

Reconstruction Results

Before applying the reconstruction algorithm to the surface pressures of the airfoil, pressure reconstruction results were validated by utilizing the results from the bench-top experiment. Figure 5.14 shows the reconstructed pressures (red) from the bench-top oscillating pressure tests as compared to the transducer measured pressure (green) and

the Endevco reference pressure (blue) for sine wave oscillation frequencies of 10, 90, 170, and 250 Hz. The length and diameter are maintained at constant values for this comparison of 18 in and 0.034 in, respectively.

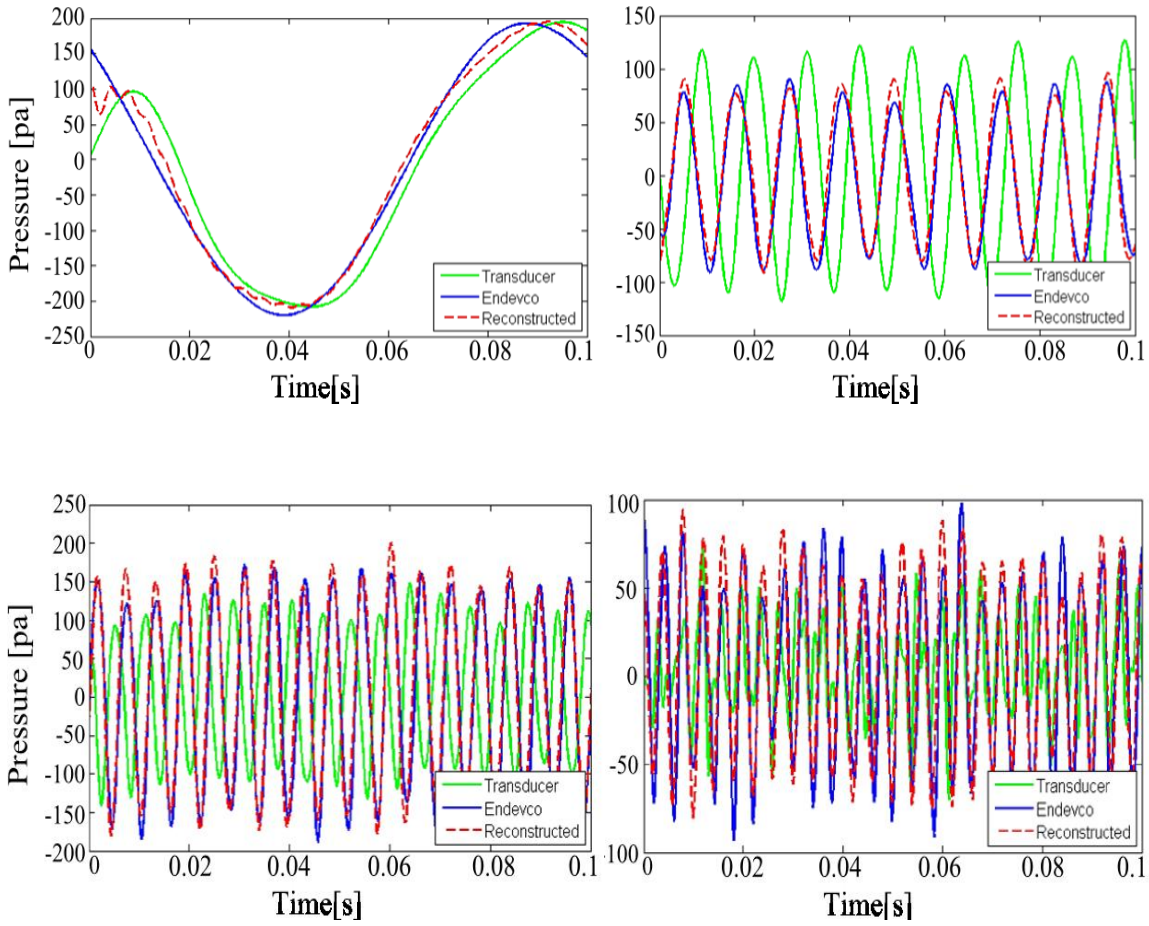

Figure 5.14. Pressure reconstruction of 10-, 90-, 170-, and 250-Hz signals

For the majority of midrange oscillation frequencies (shown 90 and 170 Hz), the phase of the signals were accurately corrected. The gains of the midrange values were correctly reconstructed for the majority of the signal; however slight over and under

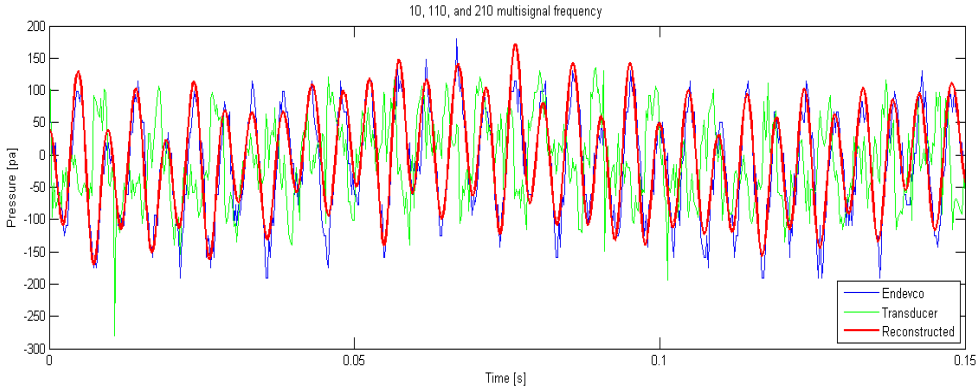

Figure 5.15. Pressure reconstruction of a multi-frequency signal of 10, 110 and 210 Hz using experimentally derived transfer function

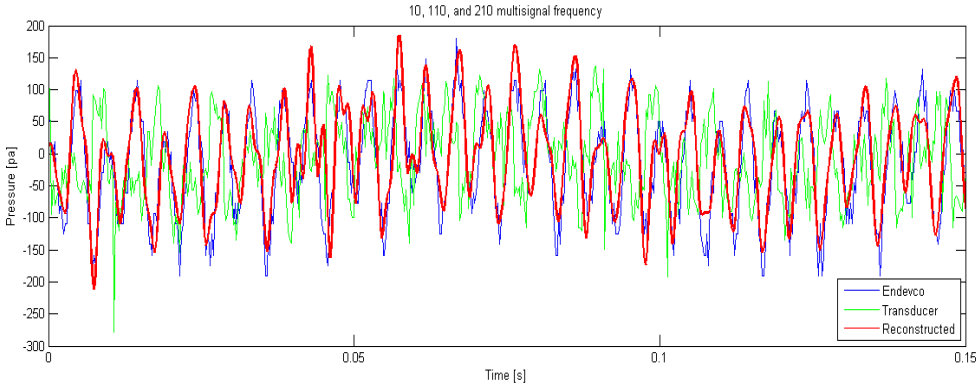

Figure 5.16. Pressure reconstruction of a multi-frequency signal of 10, 110 and 210 Hz using Tijdeman and Bergh transfer function

predictions exist in these figures. These minor inconsistencies are attributed to filtering effects with respect to energy from high-frequency noise in the various transducer measurements. For the low range oscillation frequencies (shown 10 Hz), the first few time intervals of the reconstructed signal are comparably poor. For applications of

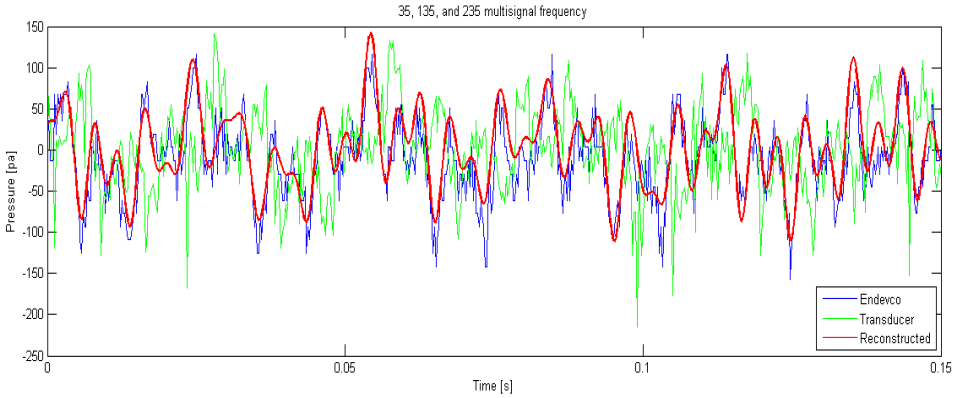

Figure 5.17. Pressure reconstruction of a multi-frequency signal of 35, 135 and 235 Hz using experimentally derived transfer function

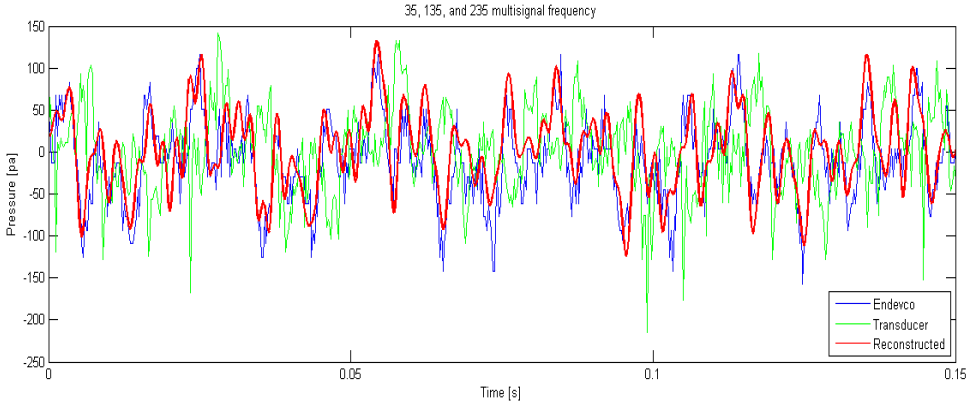

Figure 5.18. Pressure reconstruction of a multi-frequency signal of 35, 135 and 235 Hz using Tijdeman and Bergh transfer function

periodic signals, this response can be amended by either disregarding the first and last reconstruction periods or by increasing the sampling period to include more oscillations and thus increasing the dominance of the low-frequency sine wave.

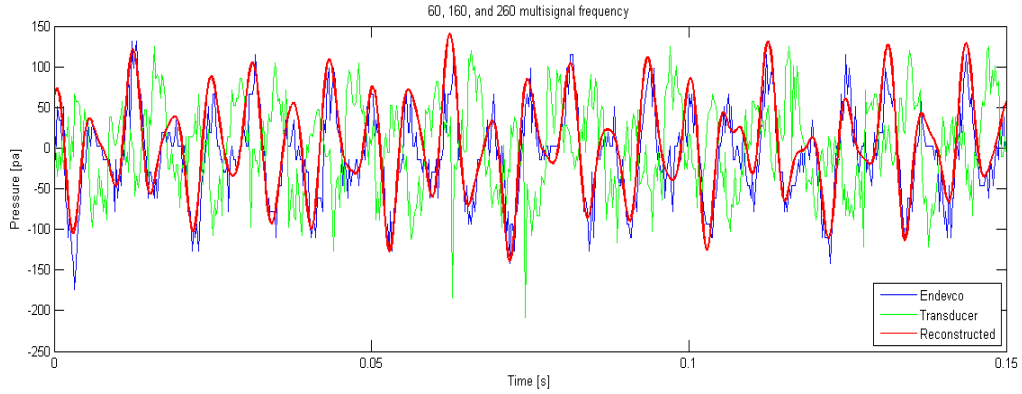

Figure 5.19. Pressure reconstruction of a multi-frequency signal of 60, 160 and 260 Hz using experimentally derived transfer function

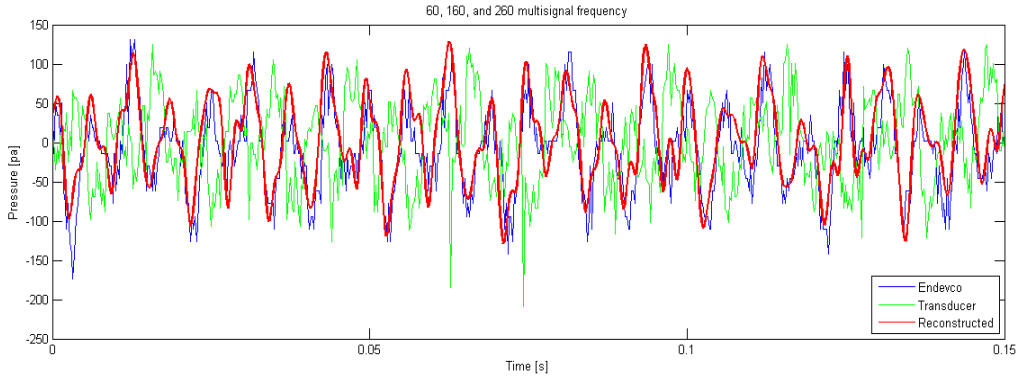

Figure 5.20. Pressure reconstruction of a multi-frequency signal of 60, 160 and 260 Hz using Tijdeman and Bergh transfer function

At high speaker frequencies (shown 250 Hz), the reconstruction magnitude begins to noticeably deviate from the reference Endevco pressure. By examining the measured transducer pressure and the reference Endevco pressure, low-frequency oscillations are apparent. The sinusoidal oscillation is no longer representative of a mono-frequency wave. Figures 5.18–5.23 further show the effects of the reconstruction algorithm on a multi-frequency signal.

The analysis of Figures 5.18–5.23 is presented here for two purposes: (1) to validate the spectral reconstruction methods of a multi-signal frequency and (2) to verify the utility of implementing the derived experimental transfer function over the analytic function. The multi-frequency signals are composed of the summation of three sine waves of equal magnitude but of varying frequencies. Figures 5.18–5.19 are of frequencies of 10, 110, and 210 Hz, Figures 5.19–5.20 are of 35, 135, and 235 Hz and Figures 5.22–5.23 are of 60, 160, and 260 Hz. Furthermore, Figures 5.18, 5.20, and 5.22 are reconstructed using the experimentally derived transfer function whereas the remaining figures used the Tijdeman and Berg analytic transfer function.

The basic trends from these plots are observed. Generally, the analytic transfer function reconstructs high-frequency elements; however, over and under estimates of peak values are observed as compared to the experimental results. For the multi-frequency analysis, individual signal frequencies were maintained between the rated speaker range of ≤ 260 Hz. However, higher frequencies in the oscillating pressure are apparent caused by coherence of the individual sinusoidal frequencies in the multi-

frequency signal. The reconstruction of these higher frequencies, as seen when the analytic function is applied, is caused by speaker frequency limitations during the experimental process. The result of this physical limitation is that the pneumatic tubing response is experimentally unknown for values above 260 Hz. This creates a low-pass filter when applying the experimental transfer function, and thus higher frequencies are not represented in the reconstruction. This filtering effect has an overall favorable response, because errors with respect to magnitude excursion are reduced compared to the analytic transfer function. The results stated from the comparative analysis validate the use of the experimental transfer function in the pressure reconstruction algorithm.

Although the reconstructed signals using the experimental transfer function more closely represented the actual reference pressure, slight variations in magnitude still were apparent at intermittent oscillation peaks. As a final method of validation, reconstruction was examined with respect to the applied unsteady upstream disturbance in the main experiment. The fast-response sensor was embedded and flush aligned in the model airfoil at the same chord location as the first pressure port on the leading edge. The upstream disturbance was actuated, and the corresponding time history was recorded using the reference Endevco transducer and using the pneumatic tubing system. The reconstruction algorithm was then applied and results from this test are presented in Figures 5.24–5.26.

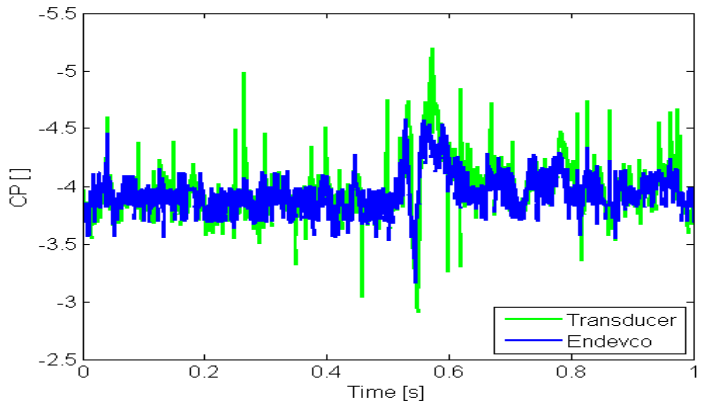

Figure 5.21. Honeywell and Endevco measurements of pressure excursion generated by the upstream disturbance measured at the most leading edge port on the NACA 63_3-418 airfoil.

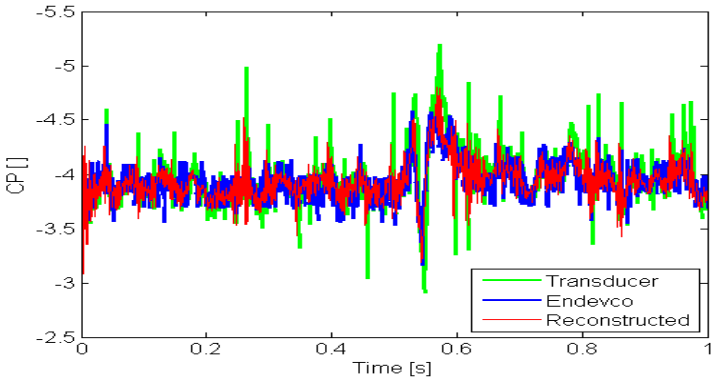

Figure 5.22. Pressure reconstruction of the Honeywell transducer measurement of the most leading edge port on the NACA 63_3-418 airfoil using experimentally derived transfer function.

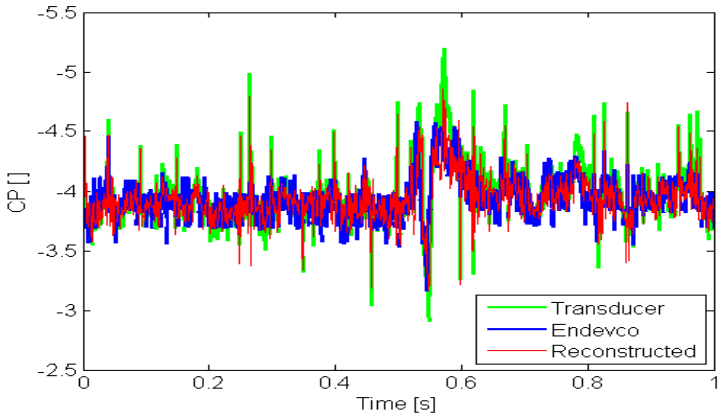

Figure 5.23. Pressure reconstruction of the Honeywell transducer measurement of the most leading edge port on the NACA 63_3-418 airfoil using Tijdeman and Bergh transfer function.

CHAPTER VI

PASSIVE FLOW CONTROL TESTS

This section documents the results of the passive flow control experiments. The research presented was conducted between December 2011 and August 2012. During this time, two test series of five different airfoil configurations were completed (Table 6.1). The first test series compared the coefficients of lift and pressure of the leading-edge slot and the baseline slot-flap to that of a clean airfoil. Maintaining slot characteristics (slot width, location, etc.), the second test series was conducted to examine the influence of the slot-flap characteristics. Two additional slot-flaps were constructed that varied a parameter of the baseline slot-flap design: (1) fiberglass but of a different length, and (2) the same length but of a different material (Mylar plastic). Table 6.2 lists the physical specifications for the three slot-flaps.

Table 6.1. List of the three comparative studies of various PFC configurations.

TEST SERIES 1 **Comparison of PFC Elements**	**TEST SERIES 2** **Comparison of Slot-Flap Variations**
Clean Airfoil	Baseline Slot-Flap
Leading-Edge Slot	Mylar Slot-Flap
Baseline Slot-Flap	¾-in Slot-Flap

Table 6.2. Summary of variations slot-flap manufacturing.

Slot-Flap Configuration	x_{te}/c	Material	Thickness (in)	Length (in)
Baseline	0.76	Fiberglass	0.012 ± 0.001	1.55 ± 0.05
Mylar	0.76	Mylar	0.035 ± 0.001	1.55 ± 0.05
¾-in	0.84	Fiberglass	0.012 ± 0.001	0.75 ± 0.05

Clean Airfoil Static Tests

The reference test configuration was a clean NACA 63_3-418 airfoil tested at a chord-Reynolds number of 0.3×10^6. For accurate comparisons and to eliminate uncertainties caused by minor variations in geometry, the clean airfoil was synthesized by sealing the slot in the airfoil slot configuration (Figure 3.1). Polystyrene foam was used to fill the slot void while maintaining the slot width. Additionally, a temporary smooth seal was placed along the surface at the slot inlet and outlet to prevent mass flow through the channel.

The static results from the clean airfoil tests were compared to experimental results published in Abbott and von Doenhoff [59]. Although this comparison was made, it should be noted that there was an order of magnitude difference between the Reynolds number of the referenced data and the current experimental effort. To further validate pressure and lift data, results were also compared to XFOIL [62] numerical analysis at representative test conditions. XFOIL is an industry-accepted program for the analysis of isolated airfoils that uses an inviscid panel method coupled with an integral boundary layer scheme to determine viscous pressure distributions. XFOIL is commonly

implemented and referenced in airfoil design, because it closely compares to experimental data at low angles of attack [60, 61]. It has also been shown to over predict $C_{L,max}$ and under predict $C_{D,min}$ with error in the chord-wise pressure distributions at high angles of attack when separation occurs [36]. For static, clean airfoil comparisons, XFOIL simulations were performed at a Reynolds number of 0.3×10^6 and an *Ncrit* transition of 9, which is representative of an average wind tunnel turbulence [62]. Figure 6.1 illustrates these comparisons of the chordwise pressure distribution and Figure 6.2 compares coefficients of lift and moment versus angle of attack.

Error bars shown in the figures are representative of systematic errors of the transducers. Random error is negligible, because each pressure measurement for the static case was tested for 3 s at a sampling rate of 1 kHz and averaged. The trailing-edge pressure shown in the C_P plots of Figure 6.1 was not measured. The point shown in the pressure distribution is the average of the rearmost data points from the upper and lower surfaces, and an error of ±0.5 was assumed. This assumption is based upon the trailing-edge Kutta condition of an airfoil.

The experimental results as compared to Abbott and von Doenhoff and XFOIL, (Figure 6.2(a)) show a decrease in C_L slope and maximum C_L. The dissimilarity in the lift curve slope and $C_{L,max}$ are attributed to effects relating to lower Reynolds number. Deviation from the linear region is also noted for negative angles of attack. This result is primarily a consequence of a lack of pressure ports along the lower surface leading edge because of the presence of the slot inlet. At negative angles of attack, a suction peak develops at the lower surface of the leading edge. The high curvature of this peak is not

captured because of the lack of pressure ports at this location, resulting in a decreased negative C_L. However, for the scope of this project, this slight variation is negligible.

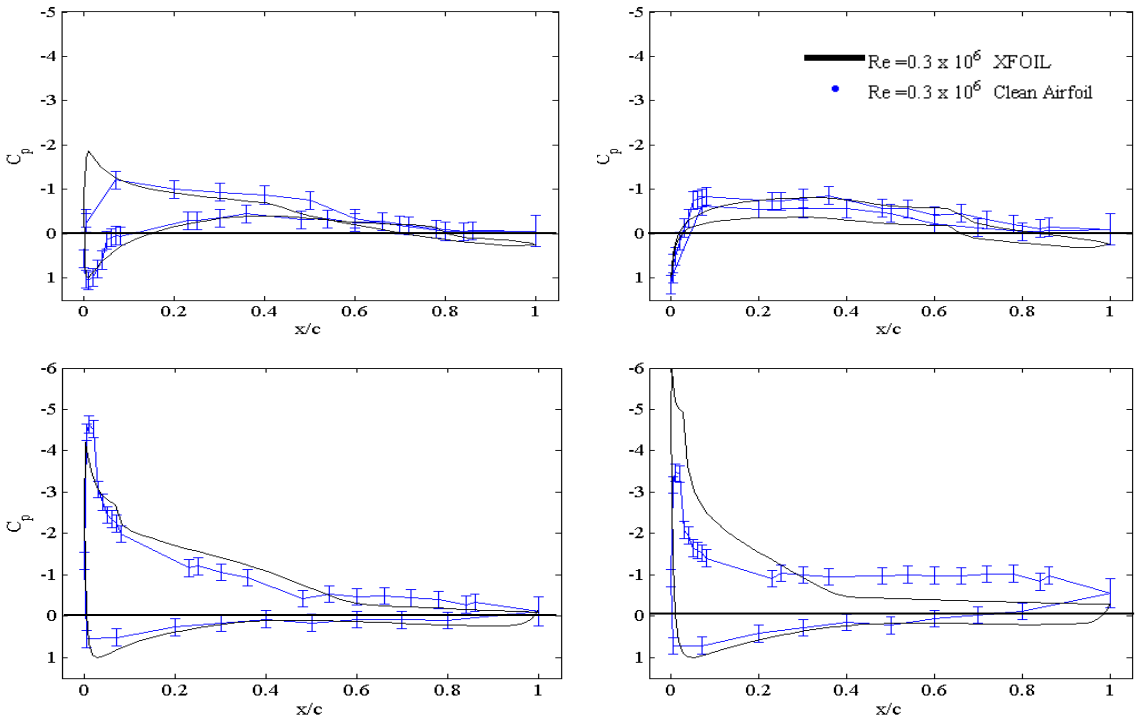

Figure 6.1(a-d) Experimental pressure coefficient profiles compared to XFOIL numerical results at Re = 3.0×10^5 for α = -6˚, 0˚, 11˚, and 17 ˚.

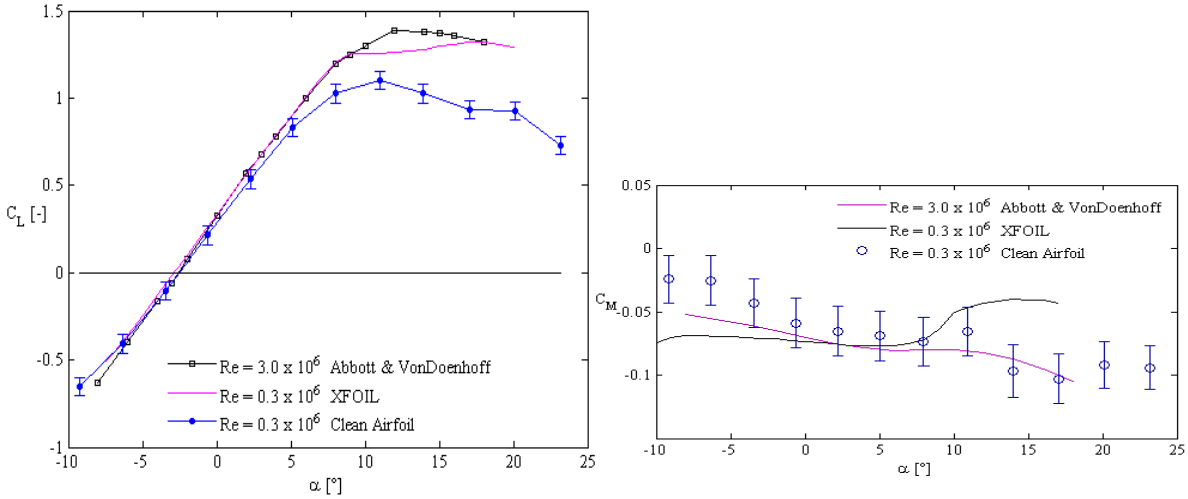

Figure 6.2(a-b) C_L (left) and C_M (right) plots of the clean NACA 63_3-418 airfoil for Re = 3.0×10^5 as compared to Abbott and Von Doenhoff and and XFOIL.

Test Series 1: Comparison of PFC Mechanisms

By examining the two passive flow control methods of the leading edge slot and the oscillating slot-flap individually, the following general observations are made. The observations presented reference Figures 6.3–6.6, which show variations in lift produced by the upstream disturbance for pitch rates of 0.032, 0.028, and 0.037, and maximum deflection angles 3º, 15º, and 27º, respectively. As shown in Chapter 4, the disturbance generates an increase, followed by an immediate decrease in lift. The variation in inflow conditions changes the effective angle of attack of the main airfoil, resulting in shifts of the C_L curve. Maximum and minimum shifts as well as the steady C_L curve are shown on the left side of Figures 6.3–6.6. The right side shows the time history of the percent change of the maximum C_L (see Equation 4.2). For the clean airfoil and leading-edge slot, this occurs at $\alpha = 11^\circ$, whereas $C_{L,max}$ of the slot-flap was $\alpha = 14^\circ$. Table 6.3

summarizes the numerical values of the maximum and minimum excursion for each case.

The leading-edge slot exhibited favorable responses in unsteady flow conditions. When comparing the percent change of lift produced by the upstream disturbance, the leading-edge slot reduced the normalized deviation. For example for the smallest deflection, $A = 0.032$ and $\alpha_D = 3^\circ$, the clean airfoil exhibits lift excursions of +15% and –12% change as compared to the static case. However, for the same actuation period, the leading-edge slot response is +9% and –7% for maximum and minimum lift deviations. Overall, the leading-edge slot exhibited reduced unsteady flow variations for all three actuation periods as compared to the clean airfoil. Similarly, the baseline slot-flap also showed reduced load excursions. However, this reduction was within the same percentage range of the leading-edge slot for most cases.

Examination of the time history of $C_{L,max}$ provided additional information of the transient-load response. For the smaller upstream deflection rates (Figures 6.3–6.4) the slot and the slot-flap configurations not only reduced the maximum ΔC_L but also reduced the subsequent loading peaks. Although reductions of subsequent peaks are also observed for the largest upstream deflection (Figure 6.5), the magnitude of ΔC_L remains generally large (above 15%). This indicates that the slot and slot-flap, although capable of reducing loads from smaller disturbances, becomes less effective with larger disturbances involving multiple vortex interactions.

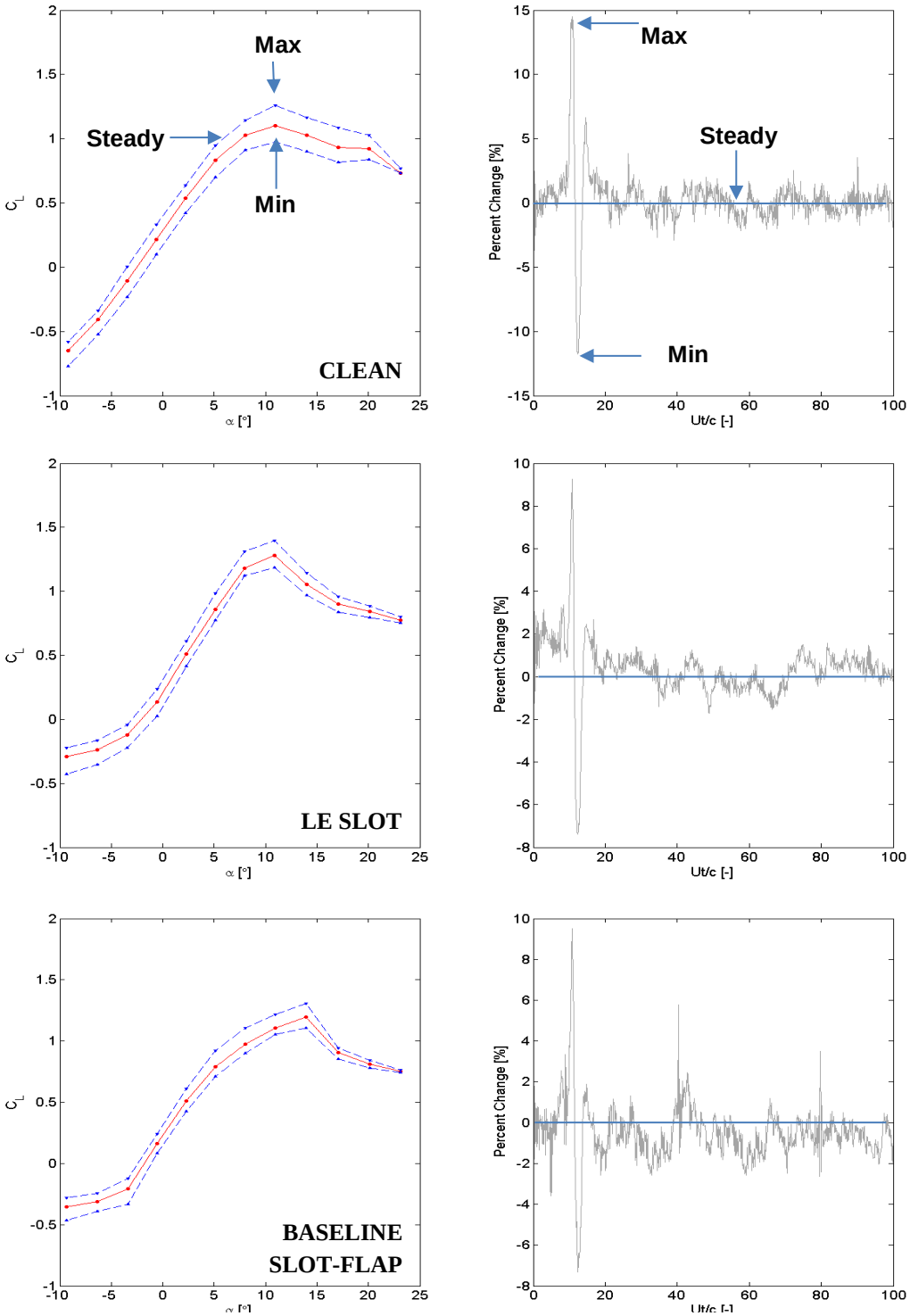

Figure 6.3(a-f). C_L vs. angle of attack (right) and percent change of $C_{L,max}$ vs. reduced time (left) for A = 0.032 and α_D = 3° for Test Series 1.

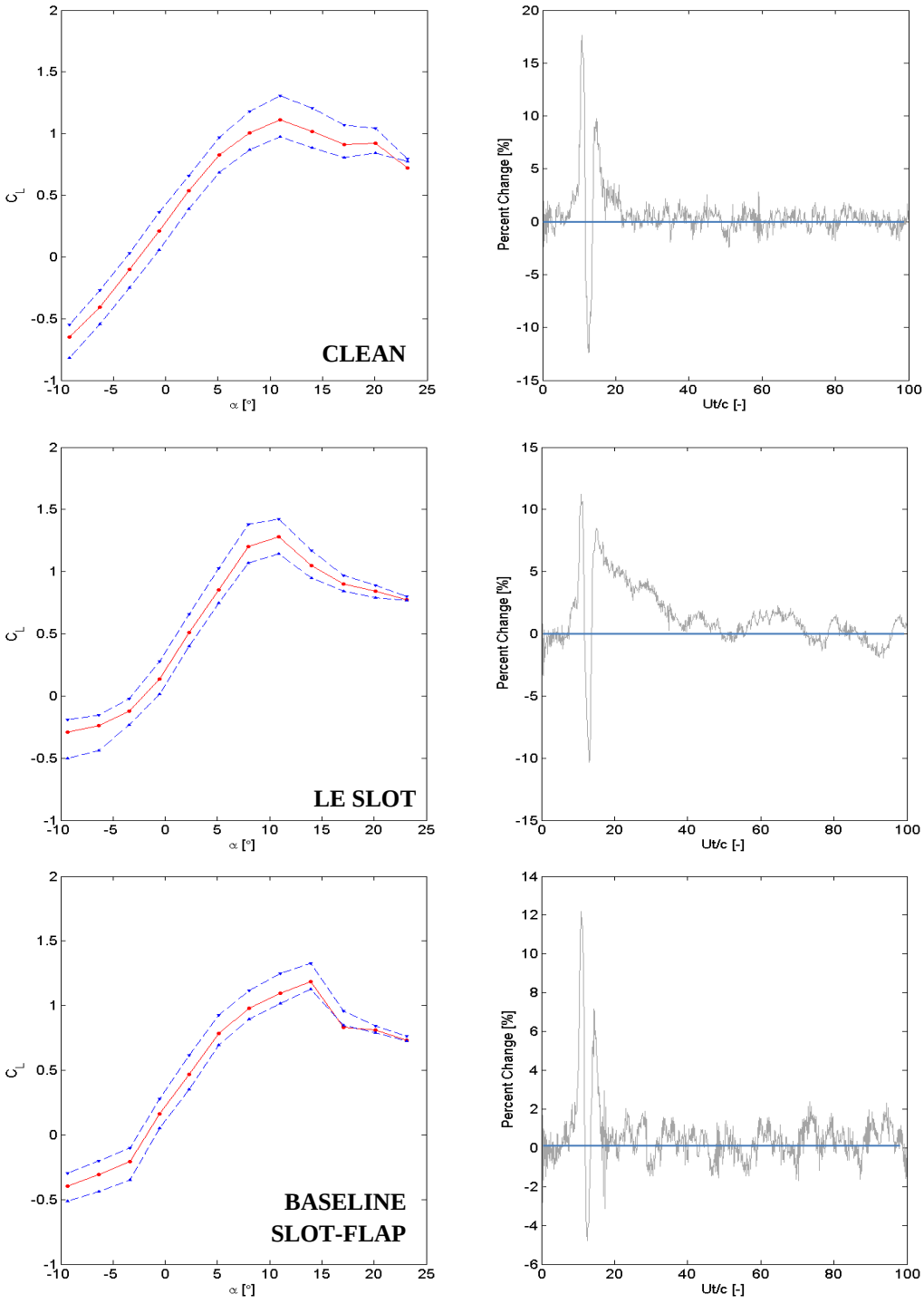

Figure 6.4(a-f). C_L vs. angle of attack (right) and percent change of $C_{L,max}$ vs. reduced time (left) for A = 0.028 and α_D = 15º for Test Series 1.

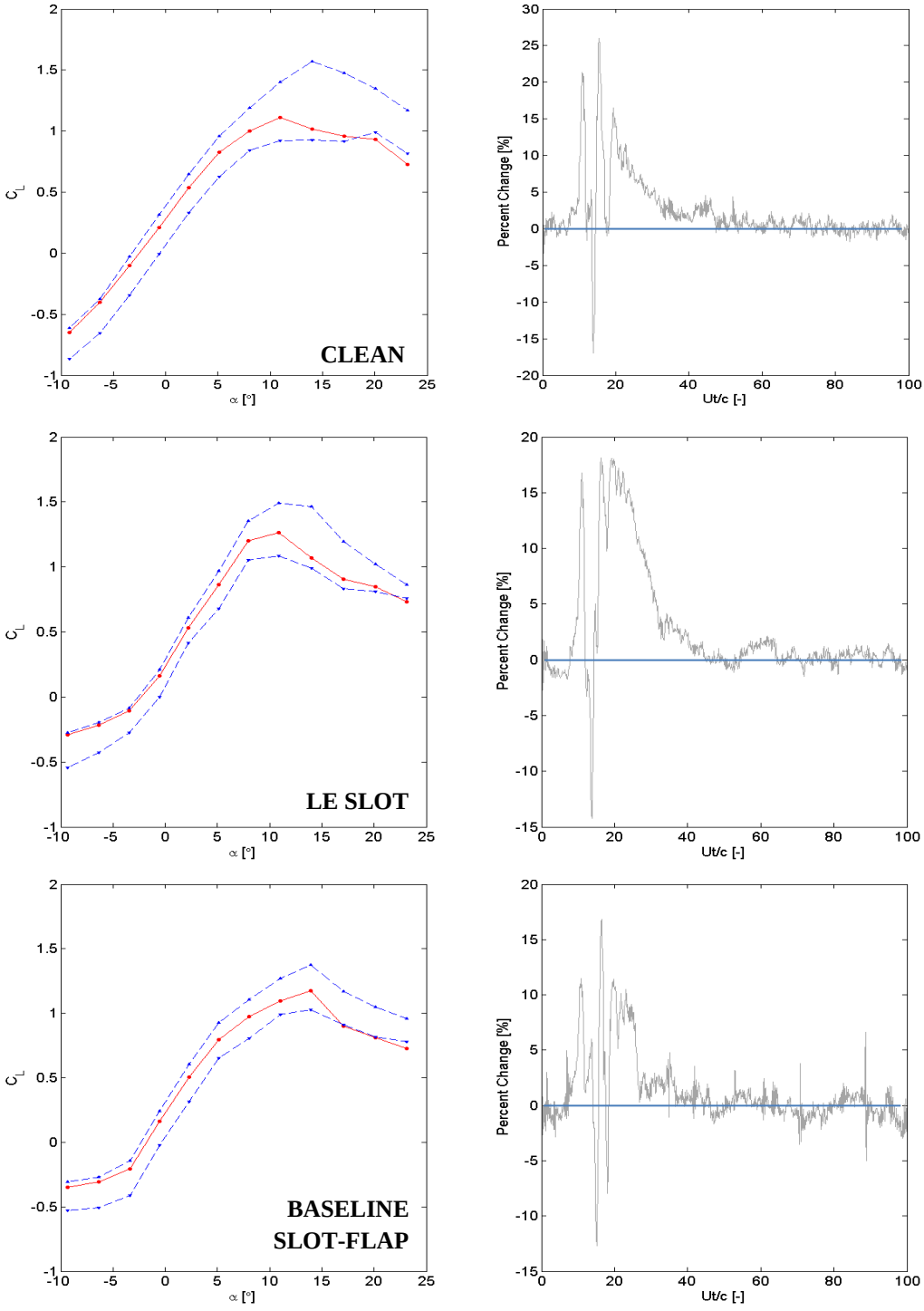

Figure 6.5(a-f). C_L vs. angle of attack (right) and percent change of $C_{L,max}$ vs. reduced time (left) for A = 0.037 and α_D = 25° for Test Series 1.

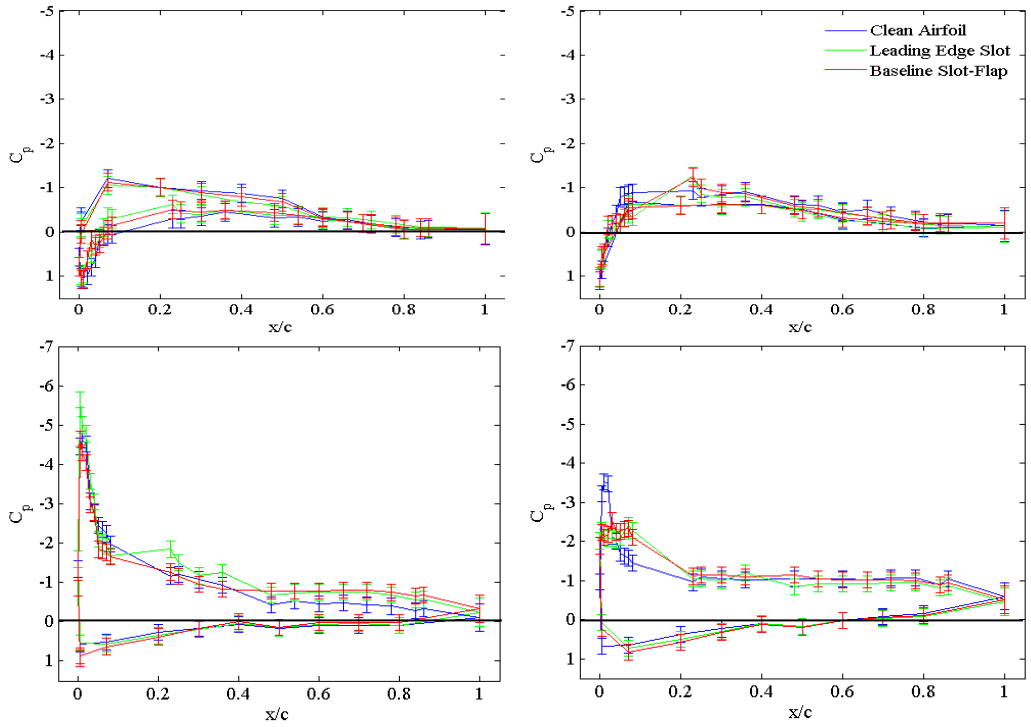

Figures 6.6(a-d). Static C_P profiles of the clean airfoil configuration as compared to the leading edge slot and the baseline slot-flap for α = –6º, 0º, 11º and 17º.

Additionally, the time history of $C_{L,max}$ illustrates the time lapse from the initial applied transient load to the return to steady state. For the larger upstream deflections (α_D = 15º A = 0.028 and α_D = 25º A = 0.037) the clean airfoil shows a delay in returning to steady state. This delay is decreased for the slot-flap configuration, but is dramatically increased for the leading-edge slot. Because only the surface pressure was measured, a further explanation on this response cannot be addressed at this time. Supplementary studies involving flow visualization, such as PIV, could provide insight on this response by further examining vortex shedding and separation occurrences with respect to the applied transient loads.

Comparisons of the three airfoil configurations are further derived from reviewing the chordwise pressure distributions (Figure 6.6). At negative angles of attack (shown $\alpha = -6^{\circ}$), both the slot and the slot-flap PFC configurations show a decrease in the C_P profile area. An interesting variation in the PFC profiles are observed at $\alpha = 0^{\circ}$, because both the slot and the slot-flap show a peak in the pressure at the ports located near the slot location on the upper surface. This peak is attributed to the additional momentum generated by the accelerated flow from the pressure differential at the slot. For $\alpha = 11^{\circ}$, the area of the slot and the slot-flap profiles increases for the trailing-edge ports. Finally, at high angles of attack (shown $\alpha = 17^{\circ}$), all three configurations are stalled.

Although both PFC methods reduce of transient load excursions as compared to the clean airfoil, the configuration notably produced significant changes in the lift curve plots. Under static conditions, the leading-edge slot maintains a constant slope of the linear-region lift curve. In contrast, at low angles of attack, the lift prematurely deviates from the linear region and results in lower negative coefficients of lift at negative angles of attack. Stall characteristics are also modified, producing an increase in lift beyond that of static stall of a clean airfoil. This observation is expected, because a leading-edge slot is a classic "high-lift" device. Nevertheless, there is a tradeoff, because the non-linear region demonstrates a significant peak and is no longer representative of "gentle-stall conditions." The static C_L curve of the slot-flap configuration also considerably varied compared to the clean airfoil. The linear region of the lift curve slope was significantly transformed for the baseline slot-flap configuration, resulting in a non-linear lift curve plot. A delay of stall was also observed. Comparatively, both the clean

airfoil and leading-edge slot show $C_{L,max}$ at angles of around 11º, where as the combined passive flow control method reached a maximum lift value at 14º.

Test Series 2: Comparison of Slot-Flap Variations

Test Series 2 varied material properties of the baseline slot-flap and the analysis was repeated. As with Test Series 1, the C_L lift curve and maximum C_L time histories were examined. By examining the C_L curve, both variations (Mylar and ¾-in slot-flaps) showed a significantly reduced the transient load excursion for the smaller upstream disturbances (Figures 6.7 and 6.8). For these cases, the excursion was reduced to a magnitude on the order of the noise of the system. As shown in Test Series 1, the slot-flap configurations are less effective in mitigating larger disturbances involving multiple vortices (Figure 6.9). For these tests, a reduction is observed as compared to the baseline, but still a significant transient load response is prevalent.

Figure 6.6 compares of the chordwise pressure distributions of the three airfoil configurations. The three slot-flap configurations show similar profile shapes for –6º, 0º, and 11º. A deviation is observed at 17º. At this angle of attack, the Mylar C_P profile shows a dominant leading edge suction peak whereas the baseline and the ¾-in slot-flaps are stalled. The trends of the static C_L vs. angle of attack of the ¾-in slot-flap are also comparable to the baseline, with a $C_{L,max}$ at 14º for both cases. The Mylar slot-flap exhibits a decrease in the lift curve slope, but shows $C_{L,max}$ at 17º.

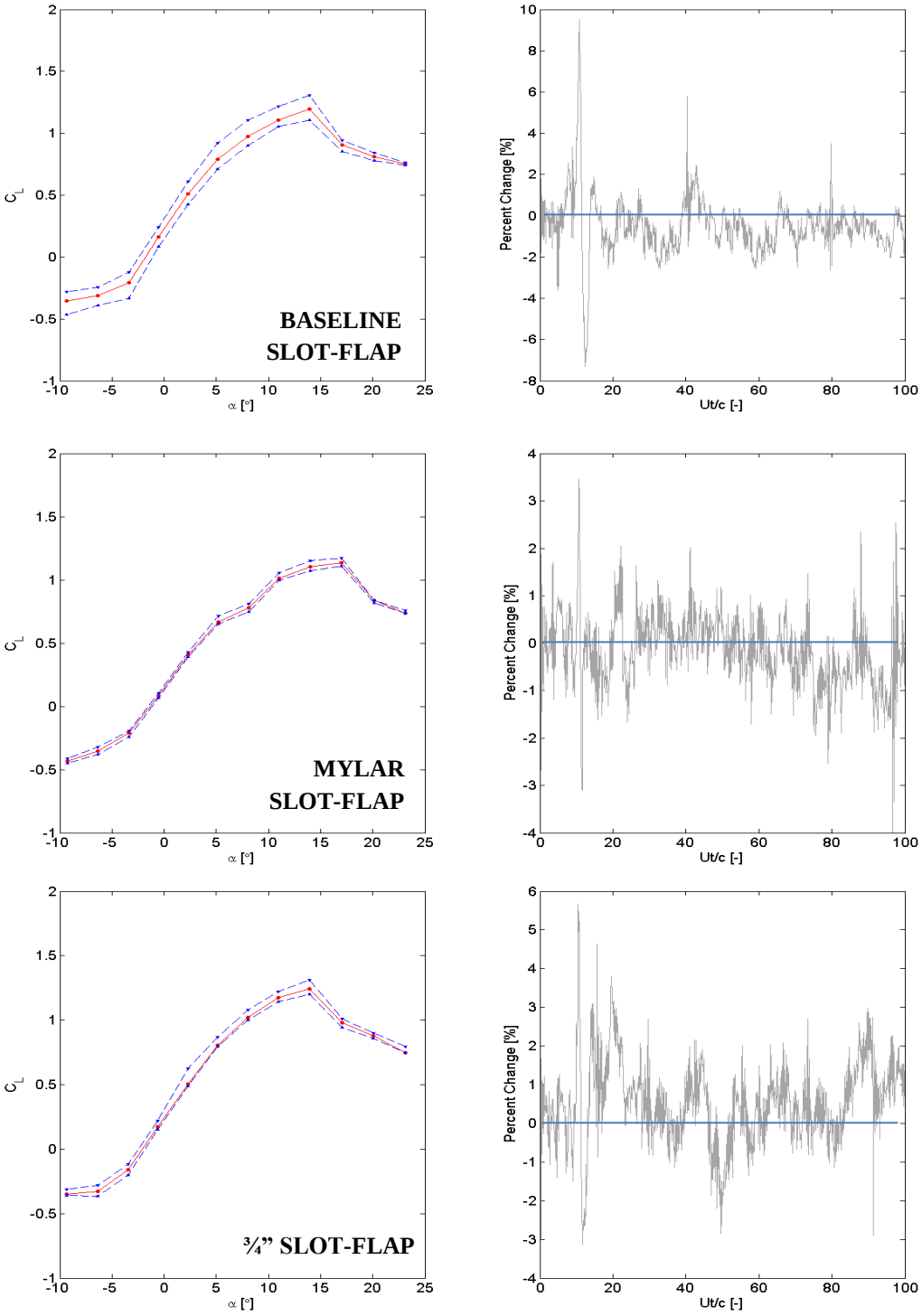

Figure 6.7(a-f). C_L vs. angle of attack (right) and percent change of $C_{L,max}$ vs. reduced time (left) for A = 0.032 and α_D = 3° for Test Series 2.

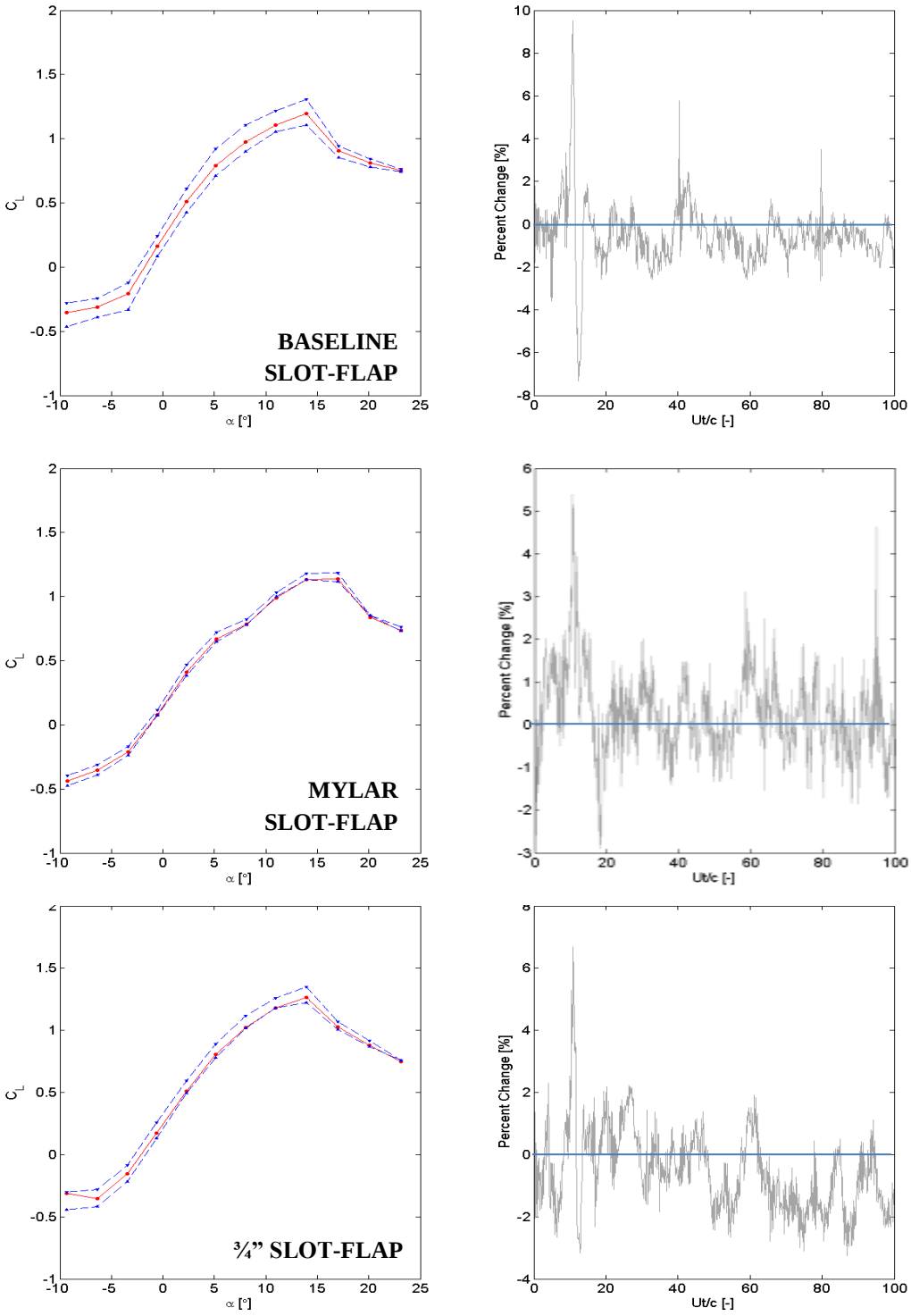

Figure 6.8(a-f). C_L vs. angle of attack (right) and percent change of $C_{L,max}$ vs. reduced time (left) for A = 0.028 and α_D = 15º for Test Series 2.

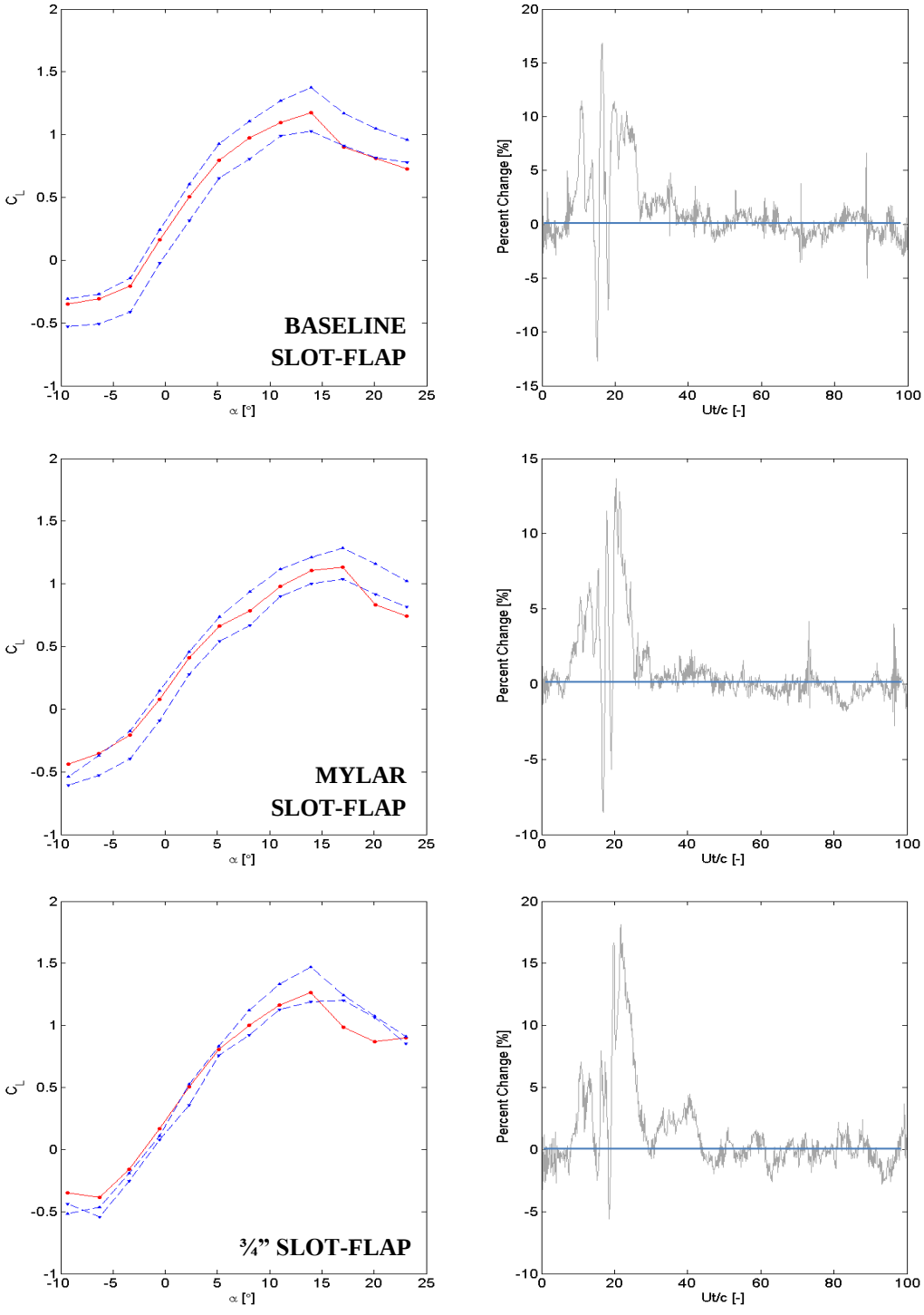

Figure 6.9(a-f). C_L vs. angle of attack (right) and percent change of $C_{L,max}$ vs. reduced time (left) for A = 0.037 and α_D = 25º for Test Series 2.

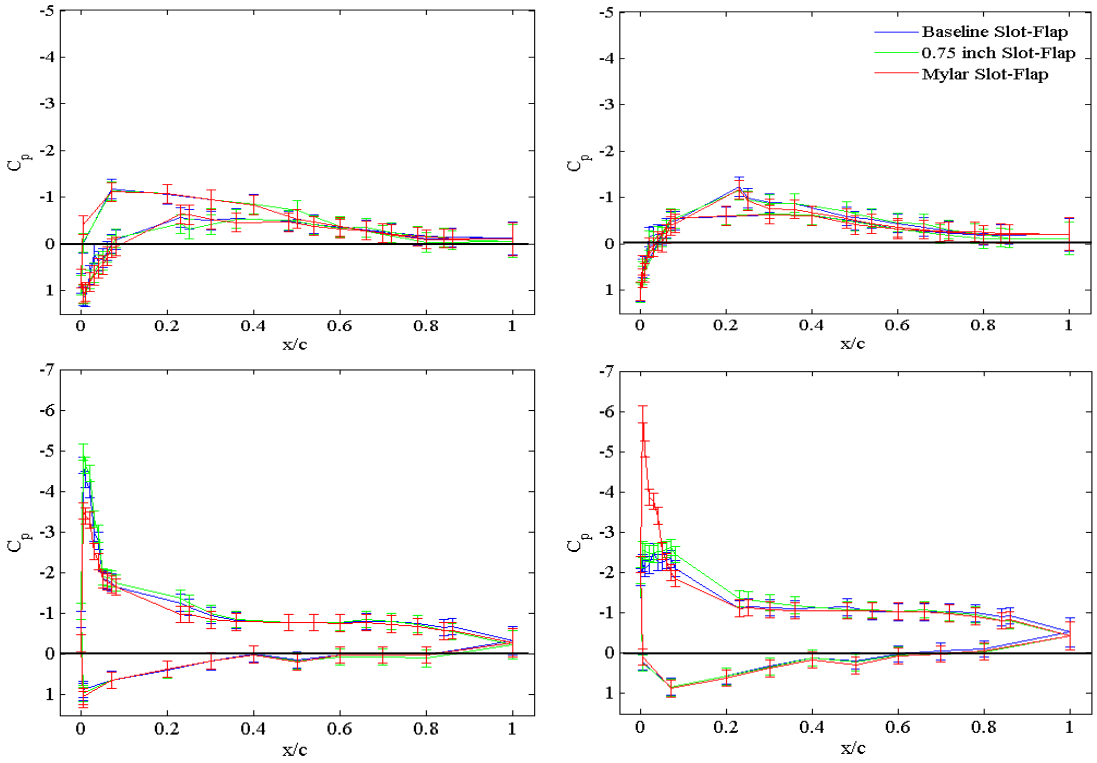

Figure 6.10(a-d). Static C_P profiles of the baseline slot-flap configuration as compared to the Mylar and the 0.75 inch slot-flaps for α = -6º, 0º, 11º and 17º.

Passive Flow Control Parameters

Results from the two test series are summarized in Table 6.3, which delineates $\Delta C_{L,max}$ values and percent change of $\Delta C_{L,max}$ from Figures 6.3–6.5 and 6.7–6.9. Figure 6.11 illustrates the variation in static C_L vs. angle of attack for each configuration. Observations of these variations have been stated in the previous sections. The results from Table 6.3 are further visualized in Figure 6.12, which plots the static $C_{L,max}$ for each case, where the error bars for this plot represent the maximum and minimum ΔC_L. Viewing the data in this manner allows for the range of load excursions

Table 6.3. Summary of transient load excursion data from PFC tests

Test Series Configuration	Pitch Rate $A = \alpha\, c_{DG}/U_\infty$	Steady $C_{L.max}$	Max ΔC_L	Min ΔC_L
Clean Airfoil	0.032	1.10 at 11˚	1.26 (15%)	0.97 (12%)
Leading Edge Slot	0.032	1.28 at 11˚	1.40 (9%)	1.19 (7%)
Baseline Slot-Flap	0.032	1.19 at 14˚	1.29 (10%)	1.08 (7%)
¾" Slot-Flap	0.032	1.24 at 14˚	1.31 (6%)	1.20 (3%)
Mylar Slot-Flap	0.032	1.14 at 17º	1.17 (3%)	1.11 (3%)
Clean Airfoil	0.028	1.11 at 11˚	1.31 (18%)	0.97 (12%)
Leading Edge Slot	0.028	1.28 at 11˚	1.42 (11%)	1.15 (10%)
Baseline Slot-Flap	0.028	1.18 at 14˚	1.33 (12%)	1.13 (5%)
¾" Slot-Flap	0.028	1.26 at 14˚	1.35 (7%)	1.22 (3%)
Mylar Slot-Flap	0.028	1.14 at 17˚	1.19 (5%)	1.12 (3%)
Clean Airfoil	0.037	1.11 at 11˚	1.40 (26%)	0.92 (17%)
Leading Edge Slot	0.037	1.26 at 11˚	1.50 (18%)	1.08 (14%)
Baseline Slot-Flap	0.037	1.18 at 14˚	1.37 (17%)	1.03 (13%)
¾" Slot-Flap	0.037	1.26 at 14˚	1.49 (18%)	1.19 (6%)
Mylar Slot-Flap	0.037	1.13 at 17˚	1.29 (14%)	1.04 (9%)

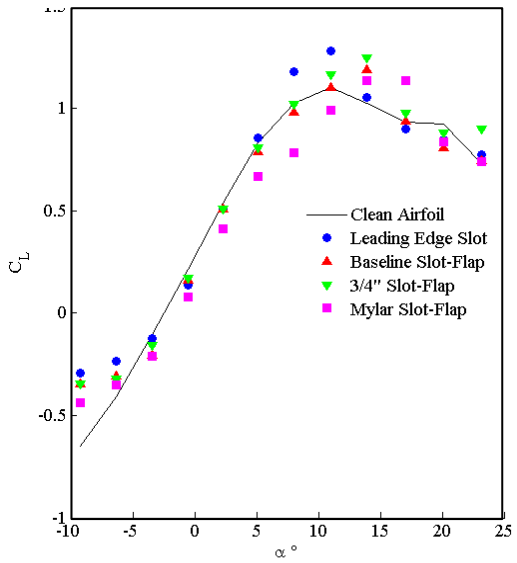

Figure 6.11. Static C_L vs. angle of attack for each test configuration.

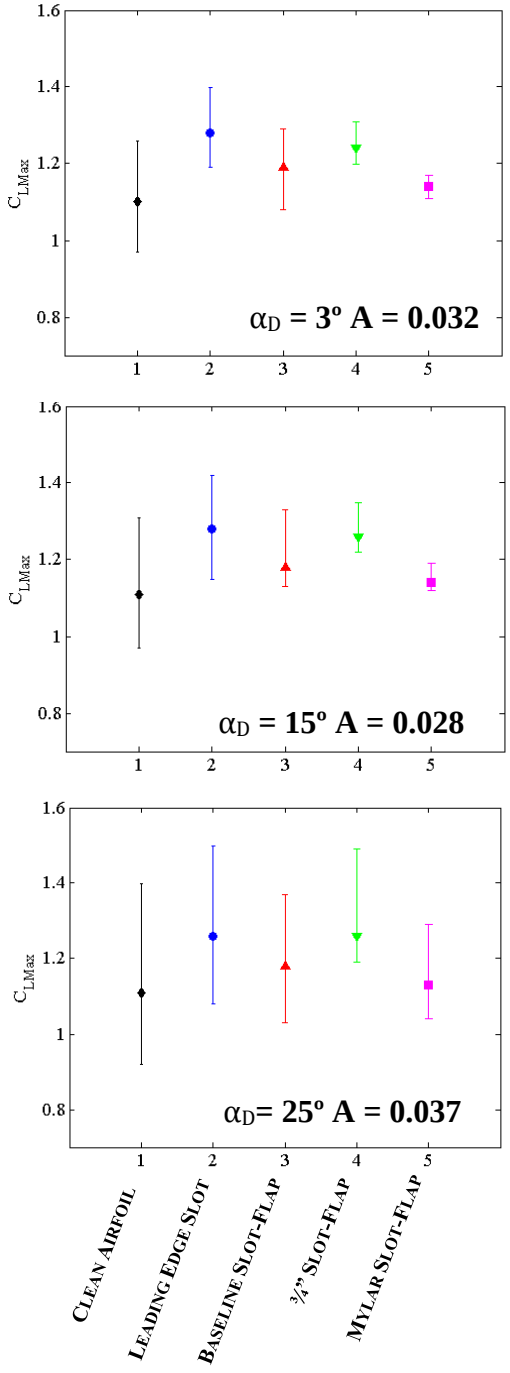

Figure 6.12(a-c). $C_{L,max}$ for each test configuration, showing average static $C_{L,max}$ (data point) and ±ΔCL (error bars).

to be visualized. From the plot, it is noted that the Mylar slot-flap has the smallest excursion range, followed by the ¾-in slot-flap. The ranges of the baseline slot-flap and the leading-edge slot are comparable in magnitude, whereas the clean airfoil exhibits the greatest excursion range.

The results from Test Series 2 indicate that both slot-flap variations exhibit improved mitigation of transient-load excursions than the baseline slot-flap. To examine this effect, the coefficient of momentum (c_μ) and reduced excitation frequency (F^+) of the slot-flat configurations were quantified. The coefficient of momentum was calculated based upon slot velocity measurements under steady flow conditions using hot-wire anemometry. With respect to angle of attack, Figure 6.13 shows the coefficient of momentum variations for the leading edge slot and slot-flap configurations. Data points represent the mean velocity with error bars representing the sampling uncertainty of six different test runs. For negative angles of attack, coefficients of momentum of the slot-flap were excluded because the slot-flap was in the "closed" position, preventing mass flow through the slot. Data from the leading-edge slot confirms this, because c_μ is approximately zero, indicating zero mass flow from the slot.

Notably, the coefficient of momentum is an order of magnitude higher than for most periodic flow control methods (0.1%); however, it is on the order of steady blowing (1%). A few comments are made with respect to this dissimilarity. The literature states that most periodic flow control methods are AFC, which actively controls the quantity and periodicity of the injected air via stored compressed air, SJAs or ZMFB. The PFC methods utilized in this research were of a different approach. The amount of injected

high-momentum fluid from the slot is determined by the pressure differential at the slot inlet and outlet, and the slot width. Thus the only controllable parameter was the slot width. For this research, the slot width was maintained at a length of 0.02*c* (1.8 in) to determined the order of magnitude of the momentum coefficient. Future tests are suggested which examine the effect of variations in slot width and the corresponding momentum coefficient on the effectiveness of transient load mitigation.

At angles of attack corresponding to the linear region of the lift curve slope, the average c_μ of the three slot-flap configurations are highly similar and are all within the uncertainty range of each other. At higher angles of attack, where stall occurs, the c_μ data points begin to separate from one another. The data points of the three slot-flap configurations fall within the uncertainty bounds; however the leading-edge slot highly deviates from the trend. Surface pressure data was once again examined in an attempt to

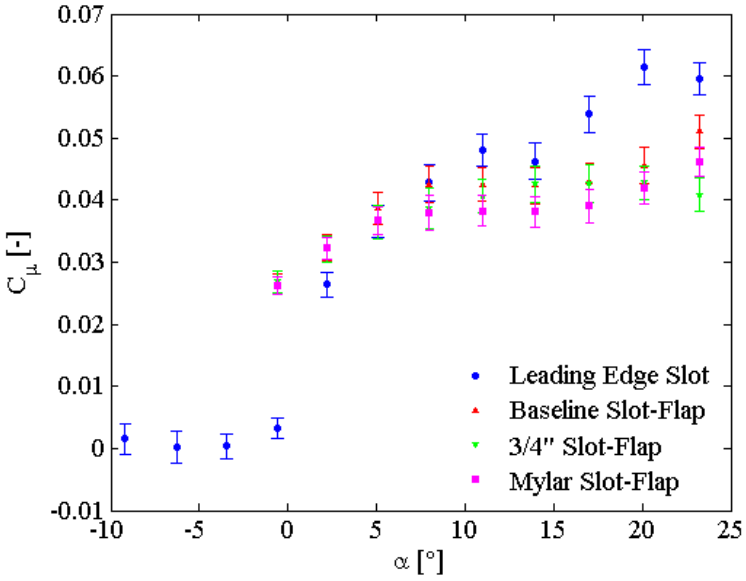

Figure 6.13. c_μ vs. angle of attack of each PFC configuration from hot wire measurements at slot expulsion point

explain this deviation. If the pressure profile of the leading-edge slot indicated higher suction on the upper surface at the slot expulsion location, then the increase in momentum might be confirmed. However, examination of the leading-edge slot and baseline slot-flap C_P data at $\alpha = 17^\circ$ showed no significant deviation, which might verify an increase in coefficient of momentum produced by an increase in suction. The theory of the slot-flap design involves enhanced mixing of high-momentum fluid from the slot with local low-momentum fluid. It is surmised that the difference in c_μ values of the could be an effect of the mixing of high- and low-momentum flows, which creates a momentum deficit as compared to c_μ of the leading-edge slot. An extensive study utilizing flow visualization techniques is required before exact conclusions may be inferred relating mixing quality to momentum defect. The primary observation from this data is that c_μ of the slot-flaps are within the uncertainty of the other slot-flap variations. Based on this test series, the improved mitigation of transient loads is not attributed to variants in $c_{\mu,}$ because all three slot-flap configurations have comparable average values within the uncertainty bounds.

Finally, for an angle of attack of 11° F^+ was quantified for the three slot-flap configurations. The corresponding frequency range was verified using a high-speed digital camera at a 1000 fps resolution. The algorithm used to process the digital video was outlined in Chapter 4. To quantify the noise associated with this process, the algorithm was applied to a random location in the image. Figure 6.14 shows a sample power spectral analysis indicating system noise. The results from the individual pixel analysis from the image window are presented in a histogram. Histogram bins were

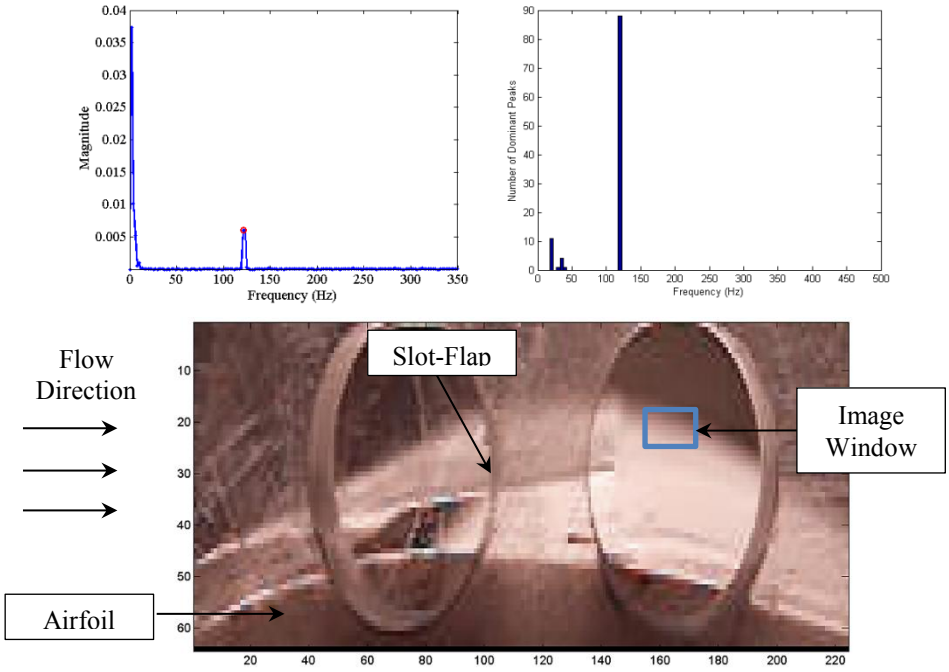

Figure 6.14. Sample signal noise frequency spectrum (left) from pixel data and corresponding histogram (right) from 14x6 image window located outside the slot-flap domain.

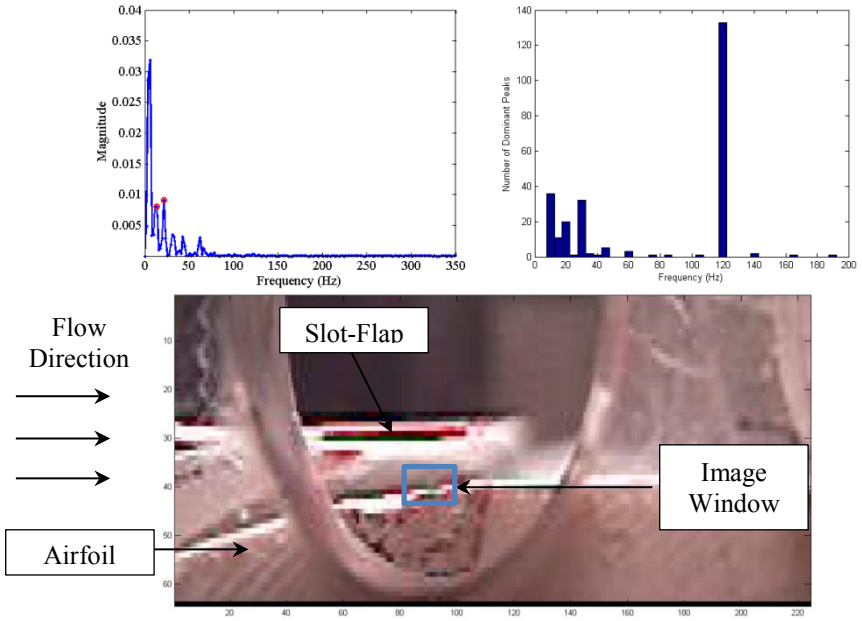

Figure 6.15. Sample ringing artifacts frequency spectrum (left) from pixel data and corresponding histogram (right) from 14x6 image window located outside the slot-flap domain.

centered at multiples of 5 and included a range of ±2.5 (e.g., 120 ± 2.5 Hz). From this analysis, it was observed that the lighting generated noise of 120 Hz.

Digital image processing may be subject to ringing artifacts. Briefly, *ringing* is a Gibbs phenomenon in which a monotonic signal yields an oscillatory output. With respect to digital image processing, ringing artifacts are apparent near sharp transitions and are viewed as bands of alternating light and dark. To examine potential effects on frequency content, the spectral decomposition algorithm was applied to an image window located outside the slot-flap domain, but in an area of sharp transition from light to dark. Figure 6.15 shows this spectral decomposition. Lighting effects at 120 Hz is once again apparent in the corresponding histogram. In addition, low-frequency content is also observed from a range from 10–45 Hz, which is attributed to ringing effects of the digital image.

A high-frequency oscillation for the baseline slot-flap could be quantified on a macro scale from the digital video. These oscillation periods were not constant, varying between a range of 7 –11 frames between oscillation peaks corresponding from 90 to 143 Hz. An image processing algorithm using pixel analysis was used to narrow this frequency range. Figure 6.16 shows the corresponding data from the power spectral density survey for the baseline slot-flap configuration. The low-frequency first peak of the spectral analysis was omitted in the survey because it is assumed to be associated with the steady-state value. The dominant frequency range was from 110 to 125 Hz, corresponding to an F^{+} range of 0.96 to 1.09. Notably, this frequency range includes the 120 Hz noise; however, the power spectral density response is significantly different

compared to the lighting effect. The noise frequency did not shift in phase, so that the magnitude of the bins of 110-, 115- and 125-Hz would not be affected by lighting effects.

Compared to the baseline configuration, the oscillations of the Mylar slot flap were of smaller amplitude and approximately the same range, qualitatively. Figure 6.17 shows the power spectral density survey for the Mylar slot-flap configuration. The dominant frequency range was from 115 to 125 Hz, corresponding to an F^+ range of 1.00 to 1.09. Additionally, a second frequency range is recognized for the Mylar configuration of 25 to 35 Hz. This frequency range is attributed to ripple effects (Figure 6.15).

The oscillation frequency of the ¾-in slot-flap configuration could not be viewed on a macro scale. The spectral density analysis was repeated for this configuration to determine if small amplitude vibrational effects were present and quantifiable on the pixel level. Figure 6.18 shows the power spectral density survey for the ¾-in slot-flap configuration. As shown, ripple artifacts dominate the frequency content of the image window. A frequency of 125.0 ± 2.5 Hz is detected, which is outside both the noise and the ripple effect and corresponds to F^+ of 1.23. The magnitude of the 125-Hz bin is significantly smaller than those of the Mylar and baseline configurations. This is attributed to amplitude of the oscillations for the ¾-inch slot-flap. Smaller amplitudes would affect few pixels, resulting in a smaller bin magnitude.

From the lift excursion plots, the Mylar and the ¾-in slot-flaps also showed improved mitigation in lift excursion compared to the baseline slot-flap; however, the flow control parameters c_μ and F^+ of the ¾ inch and baseline slot-flap showed no

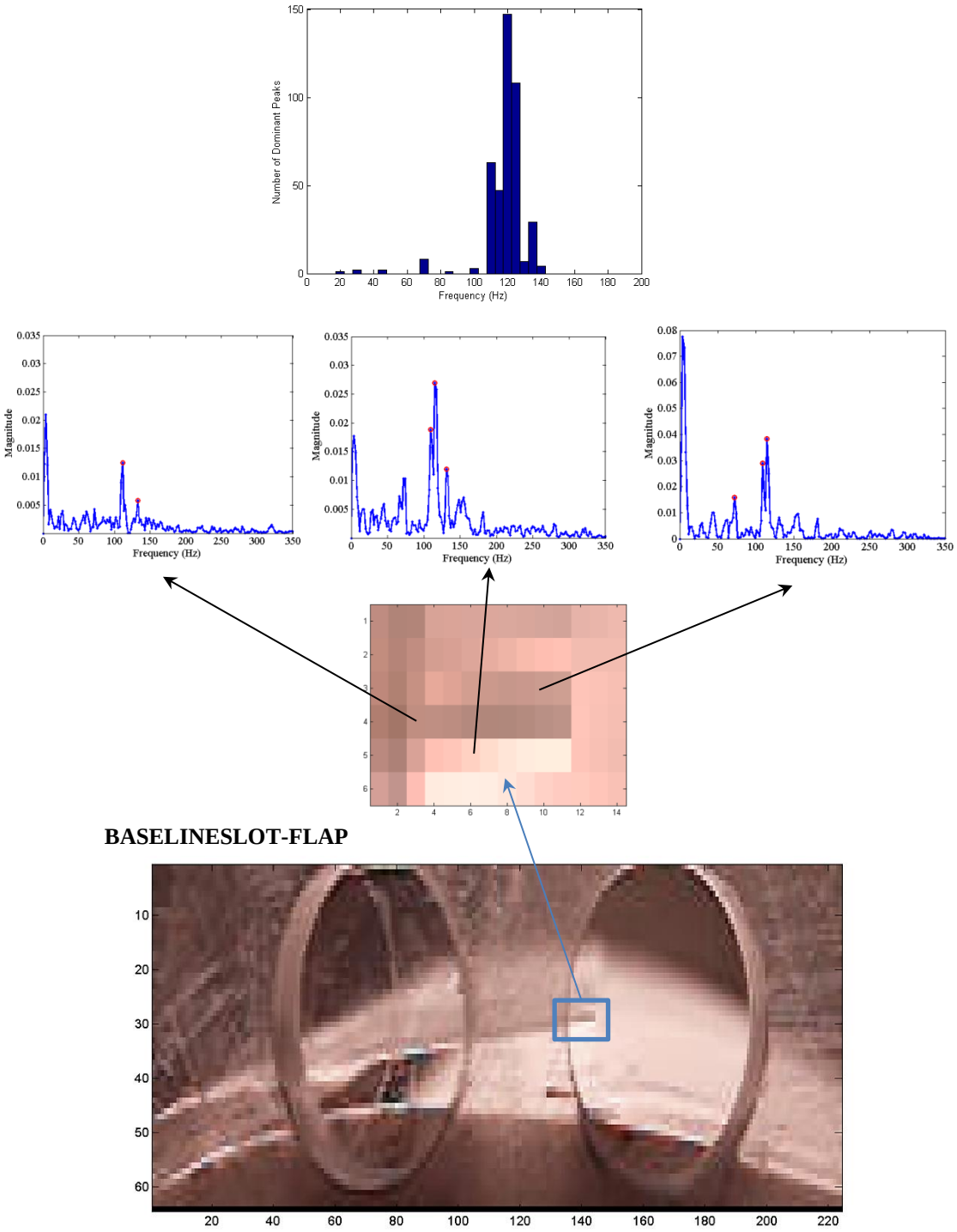

Figure 6.16. Image from the baseline slot-flap video indicating image window location and sample power spectral density for select pixels. The dominant frequencies from the image window are presented in a histogram (top).

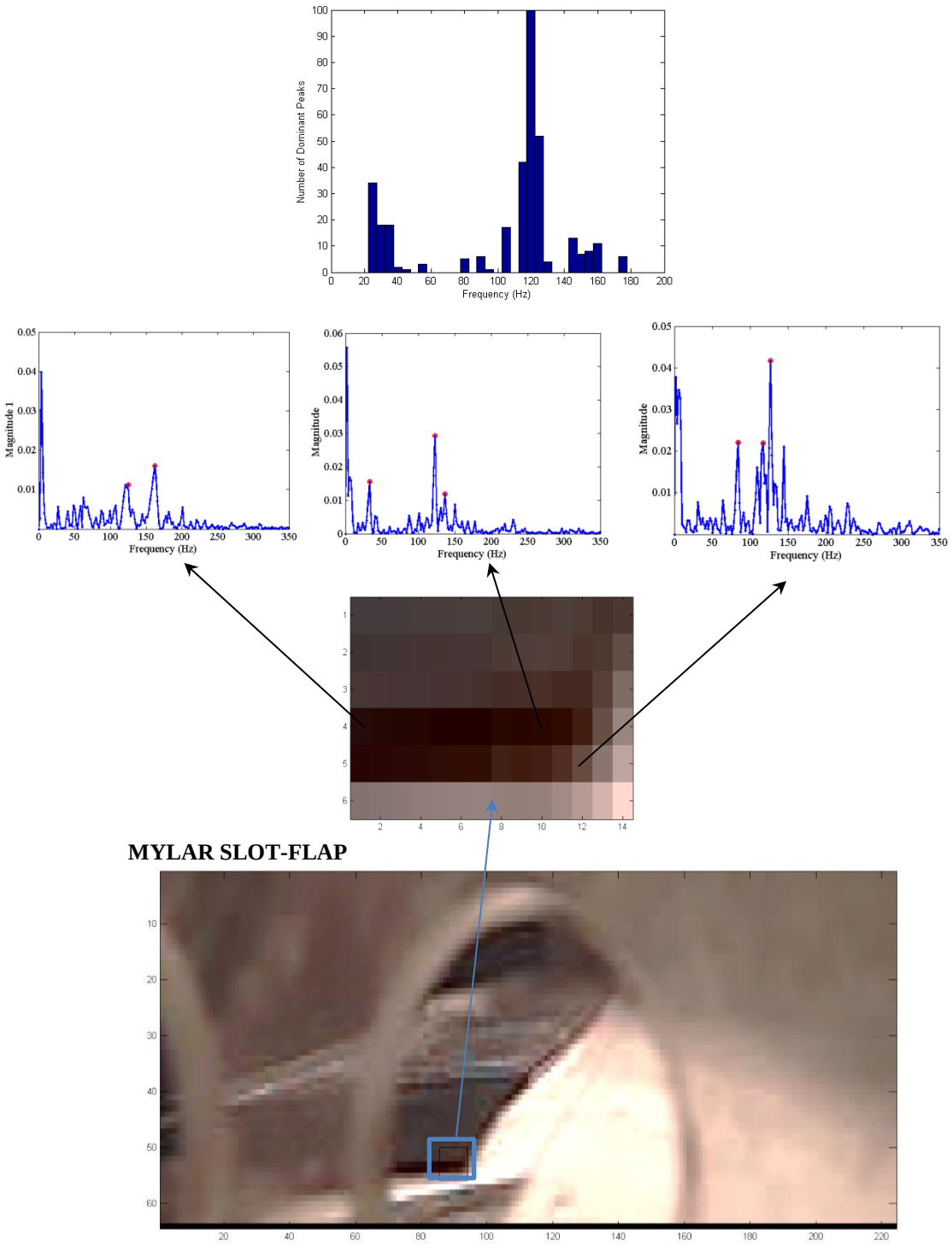

Figure 6.17. Image from the Mylar slot-flap video indicating image window location and sample power spectral density for select pixels. The dominant frequencies from the image window are presented in a histogram (top).

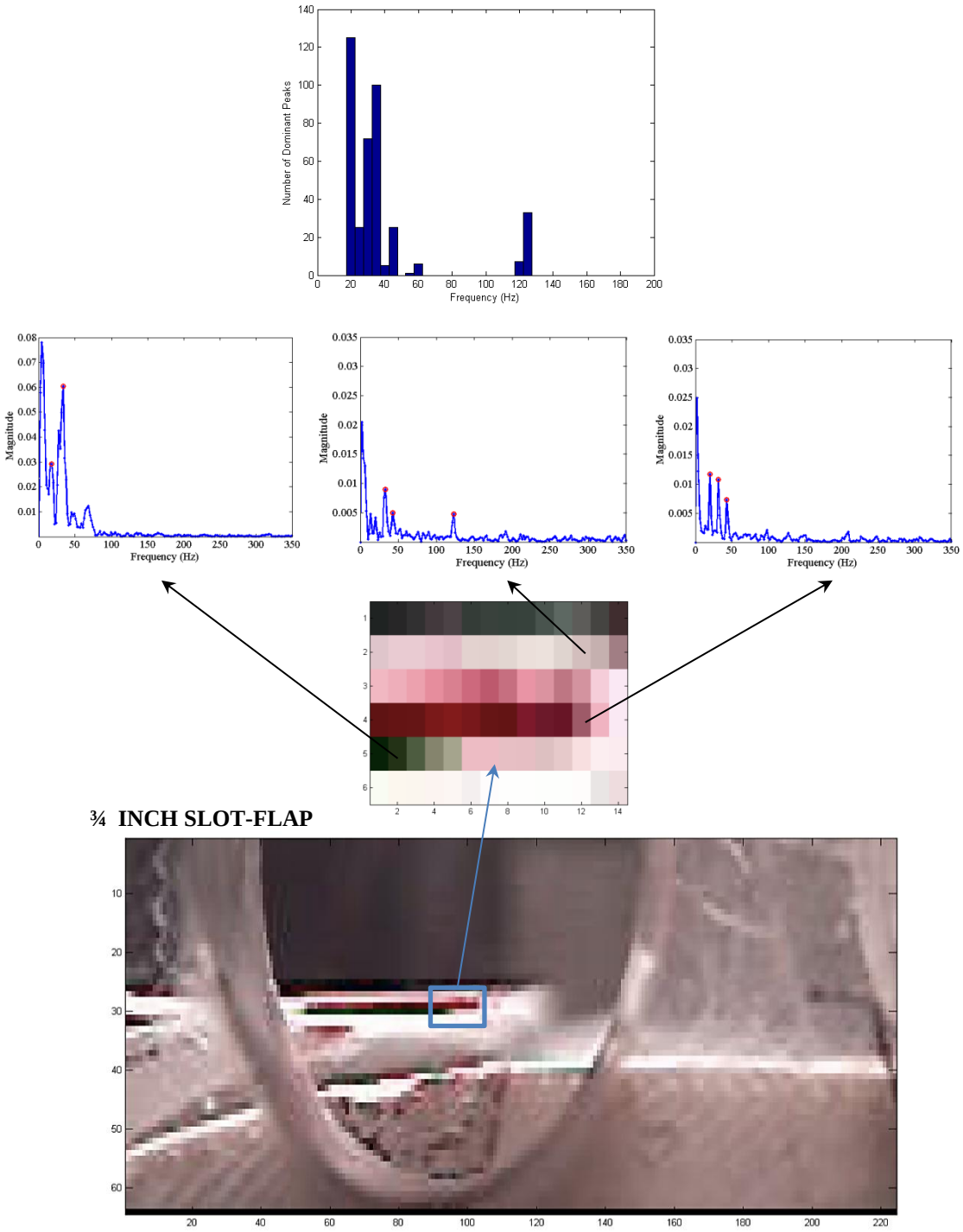

Figure 6.18. Image from the ¾ inch slot-flap video indicating image window location and sample power spectral density for select pixels. The dominant frequencies from the image window are presented in a histogram (top).

significant disparity. The reduced excitation frequency response of the three slot-flap configurations agreed with theory, such that the optimum F^+ value occurs at approximately unity. The method of pixel spectral analysis only provided a probabilistic view of the frequency content. High-precision conclusions based on the frequency content in relation to mitigation performance cannot currently be made from the present analysis.

Other factors contributing to the disparity in mitigation effects are discussed. Flow-control literature states that the chordwise location [21, 36] of the applied flow control technique and the excitation amplitude [63, 64] are highly influential on the aerodynamic response. The ¾-in and baseline slot-flap comparison indicates that the slot-flap configuration is most effective at locations closer to the leading edge of the airfoil. Oscillation amplitudes were not quantified in this study; however, from a qualitative perspective, improved mitigation was observed for the two slot-flaps (Mylar and ¾-in) with smaller oscillation amplitudes. This observation is reflected in the bin magnitude of the histogram. The bin magnitude is greatest for the baseline slot-flap and least with the ¾-in slot-flap. The bin magnitude is proportional to the number of pixels affected by the oscillations, so that reduced amplitude reduces the number of pixels capturing oscillatory effects producing a lower bin count.

CHAPTER VII

CONCLUSIONS

This thesis examined the potential of utilizing PFC methods to mitigate transient loads on a horizontal axis wind turbine blade. The PFC methods examined were that of a leading-edge slot and a combined PFC system involving a leading-edge slot and an oscillating surface (slot-flap). Before mitigation methods could be examined, the development of a repeatable unsteady upstream disturbance was required. This disturbance was generated utilizing vortex shedding of a rapidly pitching upstream airfoil and resulted in the main airfoil experiencing transient load responses with a reduced frequency of $k = 0.71$. Unsteady lift of the main airfoil was calculated using surface-pressure integration and an experimentally derived transfer function was used to correct for pneumatic tubing effects.

Tests were conducted of four PFC configurations, that of a leading-edge slot and three variations in slot-flap configurations. The test involved a NACA 63_3-418 airfoil with a 9-in (0.23-m) chord at Re = 0.3×10^6. Results from the test series demonstrated reduced maximum load excursions ($\Delta C_{L,max}$) for all four PFC methods as compared to clean airfoil tests. Performance of the PFC methods decreased for loadings with multiple vortex interactions. The leading-edge slot and the baseline slot-flap configuration showed the least reduction, whereas the two variations in slot-flap design (Mylar and ¾-in) showed the greatest mitigation. Coefficient of momentum (c_μ) of the jet at the slot expulsion location was quantified for the angle of attack range. Measured

c_μ were on the order of 1% and varied with respect to angle of attack. Additionally, using power spectral analysis of pixel data from a high-speed video, the reduced excitation frequency (F^+) was calculated for the slot-flap configurations. The reduced excitation frequency response of the three slot-flap configurations agreed with theory, so that the optimum F^+ value occurs at approximately unity. The flow control parameters c_μ and F^+ of the baseline, Mylar, and the ¾-in slot-flaps were comparable and within sampling uncertainty. The dominant variations in the configurations were the length and oscillation amplitude, which are additional parameters in flow control effectiveness. Compared to the baseline slot-flap, the ¾ inch indicated that the slot-flap was most effective at locations closer to the leading edge of the airfoil (in this case, distance from the mounting point on the slot). Oscillation amplitude was shown to be greatest for the baseline configuration. This was reflected in the magnitude of the bins in the histogram, such that reduced amplitude reduces the number of pixels capturing oscillatory effects producing a lower bin count. Based upon this study, the location and oscillation amplitude were shown to be significant parameters in the resulting mitigation effects.

The experimental results from the PFC tests indicate that the leading-edge slot and the oscillating slot-flap mitigate unsteady loading effects of excursion frequencies representative of large unsteady wind gusts on an HAWT blade. Shortcomings of the experiment are addressed. First, potential blockage effects are acknowledged. The size of the model in relation to the test section size required blockage corrections to be applied to lift measurements. The effects of blockage on the slot momentum and slot-flap oscillation frequency were not corrected for this stage of testing; because such

interactions are presently unknown. Second, the effects of slot-flap mounting were not quantified for this series of tests. The slot-flap was mounted externally and adhered to the surface of the leading-edge slat. Although significant efforts were made to flush-mount these structures, the sudden transition in material might contribute to disparities in aerodynamic responses. Additionally, variations in the upstream disturbance location were not explored. The upstream disturbance airfoil was positioned above the main airfoil, so that shed vortices from the upstream disturbance propagate over the upper surface of the airfoil. Vortex interactions in plane with or below the main airfoil might exhibit different transient loadings for which the PFC response must be quantified. Finally, Reynolds number effects are also recognized. A 2-MW HAWT potentially experiences high tip speeds corresponding to Reynolds numbers of 3.0×10^6, which is an order of magnitude higher than the experimental test range. In addition, the test Reynolds number of 0.3×10^6 is in the transitional range from laminar to turbulent flow, which also adds uncertainty with respect to transition effects. However, because the design was an optimization problem and the performance of the slot-flap was unknown, it was economically beneficial to test in a smaller wind tunnel at lower Reynolds numbers for this phase of testing.

Having verified mitigation of transient loads based on wind tunnel tests conducted in an 18-in square test section, future research involving larger scaled models at higher Reynolds numbers is recommended. Furthermore, to fully represent the unsteady effects as seen by a HAWT in field conditions, incorporating sinusoidal pitching of the main airfoil is recommend. This pitching effect is of lower frequencies and is representative

of periodic HAWT unsteady loads as opposed to aperiodic contributors, which was modeled in this research. This research also primarily used surface pressure measurements to quantify aerodynamic forces. Flow visualization methods such as PIV are proposed for future research. The incorporation of flow-visualization techniques would provide greater insight in some of the more complicated fluid-structure interactions, such as the momentum exchange generated by the slot-flap oscillation and separation effects. Further analysis of the PFC control elements is also recommended. This analysis would involve structural quantification of the slot-flap and a more in-depth investigation of the induced characteristic structural vibrations. Additional variations in the slot-flap design should also be explored. These variations would involve examining mitigation effects based on slot width and location as well as the effectiveness on different airfoil profiles (thicker vs. thinner profiles and leading-edge vs. trailing-edge stall characteristics).

Finally, additional studies relating to direct implementation of the slot-flap in wind turbine structures should be employed. These studies would explore sound generation and drag effects induced by the addition of the slot-flap on an HAWT blade. One opposition to incorporating wind energy into the nation's energy portfolio is related to the sound produced by a HAWT rotor. Increasing the sound generation would potentially be detrimental in relation to the societal impacts of wind energy implementation; thus, the sound produced by the addition of the slot-flap must be quantified for the scale of an average commercial wind turbine blade. Furthermore, drag effects were not quantified for this phase of testing, but generally the addition of a

leading-edge slot contributes to increased airfoil drag. A performance cost/benefit analysis is recommended, which would relate mitigation effects to drag increase and decreased efficiency.

REFERENCES

1. "20% Wind Energy by 2030: Increasing Wind Energy's Contribution to U.S. Electricity Supply," U. S. Department of Energy DOE/GO-102008-2567, 2008.
2. "Annual Energy Outlook 2011," Energy Information Administration, Feb 2011.
3. Huyer, S., Simms, D., Robinson, M., "Unsteady Aerodynamics Associated with a Horizontal Axis Wind Turbine," *AIAA Journal*, Vol. 34 No. 7, 1996, pp. 1410–1419.
4. Leishman, G. J., "Challenges in Modeling the Unsteady Aerodynamics of Wind Turbines," *Wind Energy*, Vol. 5, 2002, pp. 141–167. doi: 10.1002/we.62
5. Robinson, M., Galbraith, R., Shipley, D., Miller, M., "Unsteady Aerodynamics of Wind Turbines," *AIAA Journal 95- 0526*, 1995.
6. Kelley, N., Jonkman, B., and Scott, G., 2005, "The Impact of Coherent Turbulence on Wind Turbine Aeroelastic Response and Its Simulation," *Windpower 2005 Conference*. Denver, CO.
7. McCroskey, W., "Unsteady Airfoils," *Annual Review of Fluid Mechanics*, Vol. 14 No. 1, 1982, pp. 285–311.
8. Snel, H., Schepers, J., "Investigation and Modeling of Dynamic Inflow Effects," *ECWEC'93 Conference,* Travemunde, Germany, 1993.
9. Vilar, C., Amarís, H., and Usaola, J., "Assessment of Flicker Limits Compliance for Wind Energy Conversion System in the Frequency Domain," *Renewable Energy*, Vol. 31 No. 8, 2006, pp. 1089–1106.

10. Vilar, C., Usaola, J., and Amarís, H., "A Frequency Domain Approach to Wind Turbines for Flicker Analysis," *IEEE Transactions on Energy Conversions*, Vol. 18 No. 2, 2003, pp. 335–341.
11. Mouzakis, F., Morfiadakis, E., and Dellaportas, P., "Fatigue loading parameter identification of a wind turbine operating in complex terrain," *Journal of Wind Engineering and Industrial Aerodynamics*, Vol. 82 No.1–3, 1999, 69–88.
12. Fragoulis A., "The complex terrain wind environment and its effects on the power output and loading of wind turbines", *AIAA, 35th Aerospace Sciences Meeting & Exhibit*, Reno, NV, 1997, pp. 33–40.
13. Nelson, L. D., Manuel, L., Sutherland, H. J., Veers, P. S., "Statistical Analysis of Wind Turbine Inflow and Structural Response Data from the LIST Program," *Journal of Solar Energy Engineering*, Vol. 125 No. 4, 2003, pp. 541.
14. Kelley, N., Osgood, R., Bialasiewicz, J., and Jakubowski, A., "Using wavelet analysis to assess turbulence/rotor interactions," *Wind Energy*, Vol. 3, Jan 2000, pp. 121–134.
15. Eggers, J., Digumarthi, R., Chaney, K., "Wind Shear and Turbulence Effects on Rotor Fatigue and Loads Control," *Journal of Solar Energy Engineering*, Vol. 125 No. 4, 2003, pp. 402.
16. Hand, M., Robinson, M., Balas, M., "Wind turbine response to parameter variation of analytic inflow vortices". *Wind Energy.* Vol 9, 2006, pp. 267–280.
17. Hansen A., Butterfield C., "Aerodynamics of Horizontal Axis Wind Turbines," *Annual Review of Fluid Mechanics,* Vol. 25, 1993, pp. 115–149.

18. Weaver D., McAlister K., Tso T., "Control of VR-7 Dynamic Stall by Strong Steady Blowing," *AIAA Journal of Aircraft.* Vol. 41 No. 6, Nov 2004, pp. 1404–1413.

19. Alrefai, M., Acharya, M., "Controlling Leading-Edge Suction for the Management of Unsteady Separation Over Pitching Airfoils," *AIAA Journal of Aircraft.* Vol. 34 No. 11, 1996, pp. 2327–2336.

20. Stuart, J., Wright, A., Butterfield, C., "Considerations for an Integrated Wind Turbine Controls Capability at the National Wind Technology Center: An Aileron Control Case Study for Power Regulation and Load Mitigation," *Prepared for AWEA Windpower '96*, 1996, NREL/TP-440-21335

21. Greenblatt, D., "Active Flow Control on Leading Edge," *International Journal of Flow Control.* Vol. 2 No. 1, 2010, pp. 21–38.

22. Stalnov, O., Kribus, A., Seifert, A., "Evaluation of Active Flow Control Applied to Wind Turbine Blade Section," *Journal of Renewable and Sustainable Energy.* Vol. 2 No. 6, 2010, pp. 1–24.

23. Seifert, A., Darabi, A., Wygnanski, I., "Delay of Airfoil Stall by Periodic Excitation," *AIAA Journal of Aircraft.* Vol. 33 No. 4, 1996, pp. 691–698.

24. Seifert, A., Eliahua, S., Greenblatt, D., Wygnasnski, I., "Use of Piezoelectric Actuators for Airfoil Separation Control," *AIAA Journal of Aircraft.* Vol. 36 No. 8, 1998, pp. 1535–1537.

25. Gilarranz, J., Traub, L., Rediniotis, O., "A New Class of Synthetic Jet Actuators: Part II: Application to Flow Separation Control," *ASME Journal of Fluids Engineering*. Vol. 127 No. 2, 2005, pp. 377–387.

26. Traub, L., Miller, A., Rediniotis, O., "Effects of Active and Passive Flow Control on Dynamic-Stall Vortex Formation," *AIAA Journal of Aircraft*. Vol. 41 No. 2, 2004, pp. 405–408.

27. Traub, L., Miller, A., Rediniotis, O., Kim, K., Jung, G. and Jayasuriya, S., "Effects of Synthetic Jets on Large Amplitude Sinusoid Pitch Motions," *AIAA Journal of Aircraft.* Vol. 42 No. 1, 2005, pp. 282–285.

28. McCormick, M., "Boundary Layer Separation Control with Directed Synthetic Jets," *AIAA 38th Aerospace Sciences Meeting and Exhibit*. Reno, NV. Jan 2000.

29. Baker, J., Standish, K., and van Dam, C., "Two-Dimensional Wind Tunnel and Computational Investigation of a Microtab Modified S809 Airfoil," *43rd AIAA Aerospace Sciences Meeting and Exhibit*, Reno, NV, 2005.

30. Butterfield, C., Musial, W., Simms, D., "Combined Experiment Phase 1 Final Report," *National Renewable Energy Laboratory*. 1992, NREL/TP-257-4655

31. Lewis, R., Potts, I., Arain, A., "Aerodynamic Properties of NASA LS (1)-0417 MOD with Leading Edge Microspoilers for Lift/Drag Control," *Wind Engineering.* Vol. 15 No. 1, 1991, pp. 40–67.

32. Carr, L., "The Effect of a Leading-Edge Slat on the Dynamic Stall of an Oscillating Airfoil," *AIAA/AHS Aircraft Design System and Operations Meeting,* Fort Worth, TX, 1983, AIAA 83–2533.

33. Chandrasekharam M., Tungm C., and Martinm P., "Aerodynamic Flow Control using a Variable Droop Leading Edge Airfoil*," RTO AVT Specialists' Meeting on Enhancement of NATO Military Flight Vehicle Performance by Management of*

Interacting Boundary Layer Transition and Separation, Prague, Czech Republic. 2004.

34. Changm R., Hsiaom F., Shyum R., "Forcing Level Effects of Internal Acoustic Excitation on the Improvement of Airfoil Performance," *AIAA Journal of Aircraft*. Vol. 29 No. 5, 1992, pp. 823–829.
35. Gad-el-Hak, M., "Flow Control: Passive, Active, and Reactive Flow Management," Cambridge University Press, New York, 2000, pp. 150–188.
36. Wygnanski, I., "The Variables Affecting the Control of Separation by Periodic Excitation," *2nd AIAA Flow Control Conference,* 2004. AIAA 2004–2505.
37. Babbitt, A., Strike, J., Mertes, C. E., Hind, M. D., Singh, M. J., Naughton, J. W., "Dynamic Characterization of a Wind Turbine Blade Section," *49th AIAA Aerospace Sciences Meeting*, Orlando, FL, Jan 2011. AIAA 2011-350.
38. Seifert, A., Daraby, A., Nishri, B., Wygnanski I., "The Effects of Forced Oscillations on the Performance of Airfoils,"AIAA Shear Flow Conference, Orlando, Fl., July 6-9, 1993. AIAA Paper 93-3264
39. Weaver, D., McAlister, K.W., and Tso, J., "Suppression of Dynamic Stall by Steady and Pulsed Upper-Surface Blowing," NASA Tech. Paper 3600, 1996. ATCOM Tech Report 95-A-005
40. Johnson, S., van Dam, C., Berg, D. "Active Load Control Techniques for Wind Turbines," *Sandia National Laboratories.* 2008, pp. 1–132. SAND2008-4809.

41. Weaver, D., McAlister, K., Tso, J., "Suppression of Dynamic Stall by Steady and Pulsed Upper-Surface Blowing," NASA Tech. Paper 3600, ATCOM Tech Report 95-A-005, 1996.

42. Nishri, B., Wygnanski, I., "Effects of Periodic Excitation on Turbulent Separation from a Flap," *AIAA Journal*, Vol. 36, No. 4, 1998, pp.547–556.

43. Leishman, J., Principles of Helicopter Aerodynamics, Cambridge University Press, Cambridge, United Kingdom, 2000.

44. Dam van, C., Chow, R., Zayas, J., Berg, D., "Computational Investigations of Small Deploying Tabs and Flaps for Aerodynamic Load Control," *Journal of Physics*. Vol. 75, 2007.

45. Dam van, C., Standish K., and Baker, J., "Computational and Experimental Investigation into the Effectiveness of a Microtab Aerodynamic Load Control System," Sandia Report AO273, Aug. 2004.

46. Andersen, P., Gaunaa, M., Bak, C. and Buhl, T., "Load Alleviation on Wind Turbine Blades using Variable Airfoil Geometry," *Proc. of 2006 European Wind Energy Conference and Exhibition*, Athens, Greece, 2006.

47. Bak, C., Gaunaa, M., Anderson, B., Buhl, T., Hansen, P., Clemmensen, K., Moeller, R., "Wind Tunnel Test on Wind Turbine Airfoil with Adaptive Trailing Edge Geometry", *AIAA Paper*, Jan. 2007. AIAA Paper 2007- 1016

48. Fuglsang, P., Bak, C., Gaunaa, M., Antoniou, I., "Wind Tunnel Tests of Risø-B1-18 and Risø-B1-24", Tech. Report Risø-R-1375(EN), *Risø National Laboratory*, Roskilde, Denmark, 2003.

49. Fuglsang, P., Bak, C., Gaunaa, M., Antonio, I., "Design and Verification of the Risø-B1 Airfoil Family for Wind Turbines," *Journal of Solar. Energy Engineering*, Vol. 126, 2004, pp. 1002–1010.

50. Lewis, R., Potts, I., and Arain, A., "Aerodynamic Properties of NASA LS (1)-0417 MOD with Leading Edge Microspoilers for Lift/Drag Control," *Wind Engineering*, Vol. 15, No. 1, 1991, pp. 40–67.

51. Tongchitpakdee, C., Benjanirat, S., and Sankar, L., "Numerical Studies of the Effects of Active and Passive Circulation Enhancement Concepts on Wind Turbine Performance," *Journal of Solar Energy Engineering*, Vol. 128, Nov. 2006.

52. Liu, Y., Sankar, L., Englar, R., Ahuja, K., and Gaeta, R., "Computational Evaluation of the Steady and Pulsed Jet Effects on the Performance of a Circulation Control Wing Section," *AIAA Paper* No. 2004-0056, 2004.

53. Maldonad, V., Boucher, M., Ostman, R., and Amitay, M., "Active Vibration Control of a Wind Turbine Blade Using Synthetic Jets", *International Journal of Flow Control*, Vol. 1 No. 4, 2009, pp. 227–237.

54. M. S. Selig, "UIUC Airfoil Data Site, Department of Aerospace Engineering." Urbana, Illinois, University of Illinois Department of Aerospace Engineering, Jan 2007. www.ae.illinois.edu/m- selig/ads/coord_database.html

55. Schnipper, T., Andersen, A., and Bohr, T., "Vortex wakes of a flapping foil," *Journal of Fluid Mechanics*, Vol. 633, 2009, pp. 411.

56. Barlow, J. B., Rae,W.H., Pope, A., Low-Speed Wind Tunnel Testing, Third Edition, Wiley, New York, 1999.

57. Hand, M., Balas, M., "Blade load mitigation control design for a wind turbine operating in the path of vortices". *Wind Energy.* Vol 10, 2007, pp. 339–355.

58. Bergh H., and Tijdeman H., "Theoretical and experimental results for the dynamic response of pressure measuring systems", National Aero and Astronautical Research Institute, Amsterdam, Report NLR-TRF, 1965, pp. 328

59. Abbott, I. H. A, and Doenhoff A. E. Von. Theory of Wing Sections, Including a Summary of Airfoil Data. New York: Dover Publications, 1959.

60. Maughmer, M., Coder, J., "Comparisons of Theoretical Methods for Predicting Airfoil Aerodynamic Characteristics Comparisons of Theoretical Methods for Predicting Airfoil Aerodynamic Characteristics," Tech. Report, *U.S. Army Research, Development and Engineering Command*, 2010.

61. Bak, C., Aagaard, Madsen, H., Gaunaa, M., Schmidt, Paulsen, U., Fuglsang, P., Romblad, J., Olesen, N., Enevoldsen, P., Laursen, J., Jensen, L., "DAN-AERO MW: Comparisons of airfoil characteristics for two airfoils tested in three different wind tunnels", *Torque 2010: The science of making torque from wind EWEA*, 2010, pp. 59–70.

62. Drela, M., Youngren, H., "XFOIL 6.94 User Guide," Massachusetts Institute of Technology, Cambridge, MA, 2001.

63. Amitay, M., Glezer, A., "Role of actuation frequency in controlled flow reattachment over a stalled airfoil", *AIAA Journal*, Vol 40, 2002, pp209–216.

64. Greenblatt, D., Wygnanski, I., "The Control of Flow Separation by Periodic Excitation", *Progress in Aerospace Sciences*, Vol 36, 2002, pp 487–545.